ACOUSTIC DROPLET VAPORIZATION: STRATEGIES FOR CONTROL OF BUBBLE GENERATION AND ITS APPLICATION IN MINIMALLY INVASIVE SURGERY

by

Andrea Hsio-an Lo

A dissertation submitted in partial fulfillment
of the requirements for the degree of
Doctor of Philosophy
(Biomedical Engineering)
in The University of Michigan
2007

Doctoral Committee:

Associate Professor J. Brian Fowlkes, Chair
Professor Paul L. Carson
Professor Steven L. Ceccio
Assistant Professor Joseph L. Bull
Assistant Professor Oliver D. Kripfgans

"Science can only ascertain what *is*, but not what *should be*, and outside of its domain value judgments of all kinds remain necessary."

Albert Einstein (1879-1955)

For my family,

Ben, Lisa, and Audrey Lo

and in loving memory of my grandparents,

Wei Chin and Chun Hon Tsang

ACKNOWLEDGMENTS

The pages bound between this hard cover embody and tie together the people who have shared my graduate school experience with me. It is representative of the stages of progression and growth, and of those who have encouraged and taught me. It is hard to believe that this book is now closed, although hopefully it will still be opened once and awhile.

I have been so fortunate to have been able to work with and share friendships with the people whom I've met at the University of Michigan. I am grateful to my doctoral committee, Professors Brian Fowlkes, Paul Carson, Steve Ceccio, Joe Bull, and Oliver Kripfgans, all of whom have guided my dissertation from the onset and have lent valuable scientific advice and ideas. I would like to especially thank my advisor Brian Fowlkes and mentors Oliver Kripfgans and Paul Carson, who comprise the faculty members serving on the Vascular Bubbles project. I have learned a great deal from Brian, with his attention to detail, pragmatic approach, and leadership. I am fortunate to have had an advisor who supported my work in all the ways that I needed it and who wholeheartedly shared my excitement during small and large successes. I was also a direct recipient of Oliver's generosity, both with his time and intellect. My assimilation into the lab and development was only possible with Oliver's support. As an experienced mentor and participant in the field, Paul has given me valuable insight into the development of my career and brings great warmth to work environment.

It would not have been the same experience if it were not for the Kresge family. Although I may not have directly worked with many of the faculty, Drs. Jerry

LeCarpentier, Scott Swanson, Jon Rubin, Aaron Moskalik, and Will Roberts were always willing to help and discuss any issues at any time, whether it was about my research or the weekend. I am also grateful for the scientific and invaluable moral support of the other graduate students both past and present, from the North Campus BUL lab to the Kresge group, including Jessi Parsons, Zhen Xu, Tim Hall, Michol Cooper, Christine Tse, Marwa Zohdy, Titaina Potdevin, and Stan Samuel. They have been solid pillars as colleagues and friends. I owe many of the good times in the drab Kresge basement to my labmate, Kevin Haworth. As we met weekly to discuss our individual projects, we came to know the details of each other work. I greatly appreciate the collaboration, camaraderie, and conversations we shared.

I acknowledge Maria Steele in the BME department who is amazingly attentive to meeting students' needs and for her uplifting attitude and high energy. I also thank Dr. Kim Ives, our resident Kresge veterinarian, who has dedicated much of her time to long-lasting experiments and who contributes valuable expertise.

In the five years that I've spent here, I've made friendships that will last a lifetime and are worth a lifetime. My friendships with Nadder Sahar and Kiran Pandey began during our first year as graduate students, when we spent countless hours doing homework and projects together. Despite separating into our own labs and research, their friendships continue to be essential to my being. I also thank my boyfriend, Peter Rossi, for his patience and for being my outlet for anything and everything.

Finally, I thank my family, Ben, Lisa, and Audrey Lo, without whom I could never attempt the goals I reach for. They have encouraged me throughout my academic career and through life. I am so fortunate to have their everlasting support. It is to them I owe my heartfelt gratitude.

TABLE OF CONTENTS

LIST OF FIGURES

Figure

LIST OF TABLES

Table

ABSTRACT

ACOUSTIC DROPLET VAPORIZATION: STRATEGIES FOR CONTROL OF BUBBLE GENERATION AND ITS APPLICATION IN MINIMALLY INVASIVE SURGERY

by

Andrea Hsio-an Lo

Chair: J. Brian Fowlkes

As a minimally invasive alternative to current cancer treatment, the use of encapsulated, superheated liquid perfluorocarbon droplets has been proposed to treat cancer by occlusion therapy. In response to an applied acoustic field, these droplets, which are small enough to pass through capillaries, vaporize into large gas bubbles that subsequently lodge in the vasculature. This research investigates strategies to reduce the required pressures necessary to achieve acoustic droplet vaporization (ADV), what implications they may have on efficiency, and how the resulting location of bubbles may alter the acoustic field.

Two methods to lower the ADV threshold were explored. The first method investigated the role of pulse duration on ADV. The second investigated the role of inertial cavitation (IC) external to a droplet by adding ultrasound contrast agent (CA), which has a low IC threshold. At 1.44 MHz, the threshold was found to

be 5.5-5.9 MPa peak rarefactional pressure (P_r) for short microsecond pulses and decreased for millisecond pulses to 3.8-4.6 MPa P_r. When CAs were added and long millisecond pulses were used, the ADV threshold decreased to values as low as 0.41 MPa P_r.

With the help of CA, the same amount of power was necessary to achieve ADV through an attenuating tissue mimicking (TM) phantom as it was without attenuation and with only droplets. When comparing ADV pressure thresholds, where *in situ* pressures were used when a TM phantom was present, rarefactional pressure appeared to be the salient determinant. However, careful consideration must be taken when choosing pulse repetition frequencies and amplitude as inertial collapse of both ADV and IC bubbles appears to affect efficient droplet conversion.

During *in vivo* application, treatment planning may be important as backscattering properties of microbubbles created by ADV can augment or obstruct the sound field in the affected area. With strategic targeting and subsequent conversion of droplets into microbubbles at one location, constructive interference due to these effects reduces the transmitted pressures required for ADV proximal to that location. The attenuation from these bubbles can create a protective boundary for areas distal to the treatment volume. The potential result can be a confined area for further treatment by ADV or other acoustic means at lower acoustic output than would otherwise be required.

CHAPTER I

Introduction

1.1 Minimally Invasive Surgery

Minimally invasive surgery (MIS) has long since been a movement in the practice of medicine. With minimal collateral damage, it is a natural progression as less damage to overlying tissue minimizes chances of infection, facilitates healing, and reduces scarring, all of which reduce the possible accompanying costs of the surgery itself. Currently, MIS practice is often considered laparoscopic or endoscopic surgery, where small incisions are made for insertion of a camera and long surgical instruments into the body. In a less traditional sense although in no way less established, MIS also includes extracorporeal treatments that have been developed to perform surgery without the need of any incision. Examples include shockwave lithotripsy and now, high intensity ultrasound (US), which has become a new wave of minimally invasive or perhaps even noninvasive techniques to perform surgery.

This chapter will provide an overview of the current available technologies for minimally invasive and noninvasive surgery. Of particular interest is the treatment of renal cell carcinoma (RCC), where unique challenges arise due to the location of the organ and its high perfusion. A discussion of the current techniques and their challenges as they apply to RCC is provided and is followed by the introduction of the thesis topic. This dissertation will describe research into a novel cancer therapy technique that creates gas emboli to deprive cancer cells of their blood supply. This

technique uses injectable liquid dispersions that can be vaporized with an acoustic pulse at a specific target. In comparison to the available alternatives, this method offers advantages that make it more ideal for treatment of RCC.

1.2 History and Future of Surgical Techniques

1.2.1 Laparoscopy and Endoscopy

With the important benefits reaped from MIS, many advances and innovations were achieved in a short amount of time. The first laparoscopic cholecystectomy (gall bladder removal) was performed in France in 1987 by Mouret, and in one year had spread to the United States and other countries [1]. It became the standard method of treatment [2] in two years. Around the same time, the United States Army funded the former Stanford Research Institute to produce a telesurgical workstation for remote surgery on the battlefield. The outcome from this project became the prototype for the now commercial da Vinci® Surgical System (Intuitive Surgical, Inc., Sunnyvale, CA), which was first cleared by the United States Food and Drug Administration (FDA) in 2000 for general laparoscopic surgery. It is currently approved by the FDA to perform certain minimally invasive urologic, gynecologic, and cardiac surgical procedures. Mitral valve repairs, joint replacements, prostatectomies, and other surgeries are now performed with laparoscopic or endoscopic minimally invasive techniques on a regular basis.

Extending the idea to telesurgery, then, does not seem out of reach. With the capabilities of information technnology (IT) today, the global reach of medicine is broadened in what has been dubbed "telemedicine". In the future, surgeons would be able to extend their technical skill set beyond their own operating room. Because it is already possible to perform surgery without being in direct contact with a patient with current commercial systems, these surgical techniques should also be able to be translated offsite through the use of telecommunications. Research is

being done to develop these telesurgical workstations, where surgeons perform the procedure in a remote location while being given the appropriate visual cues. Their motions and commands are transmitted to the robotic workstation where the patient is situated. Assistants present in the operating room are responsible for changing surgical tools as well as following instructions given by the offsite surgeon. With telecommunications, the potential of this system is global. Experts from all over the world can work together in a remote operating room. This not only brings together the best talent to one room, but it also saves resources in air travel and time, and can be beneficial to the patient who is perhaps too sick to travel. This is telemedicine at its highest level.

Current implementation of telemedicine allows doctors to share medical knowledge on a global level. Today, physicians in certain African nations can extend outside their borders to reach specialists for medical consultations in countries such as Canada and the United States [3]. Thus, patients traveling to their local facilities are assured that they will receive world-class care, an attractive service that encourages more consumers to seek medical attention. Existing collaborations include King Faisial Specialist Hospital and Research Center in Saudi Arabia and Massachusetts General hospital, Singapore General Hospital and Stanford University Hospital, King Hussein Medical Center in Jordan and Amman Surgical Hospital with the Mayo Clinic, and Arab Gulf States with WorldCare, a private U.S. company [3].

1.2.2 Bloodless Alternatives

Apart from the burgeoning utility that laparoscopic techniques have found in robotics and telemedicine, bloodless surgery has also been in practice for a number of years. Some of these technologies are listed and described in the following section.

Extracorporeal shock wave lithotripsy (ESWL) as a treatment of kidney stones was introduced in 1979 in Germany [4], with the first human clinical trial in 1980

by the same group [5]. Ultrasound (US) had been used prior to ESWL, but direct contact between stone and transducer was necessary. Shock waves in ESWL are generated by spark electrodes placed in one geometric focus of half an elliptical reflector and refocus to the second focus of the ellipse, where the target (kidney stone) is situated and disintegrated (Fig. 1.1a). ESWL is now a routine noninvasive outpatient procedure.

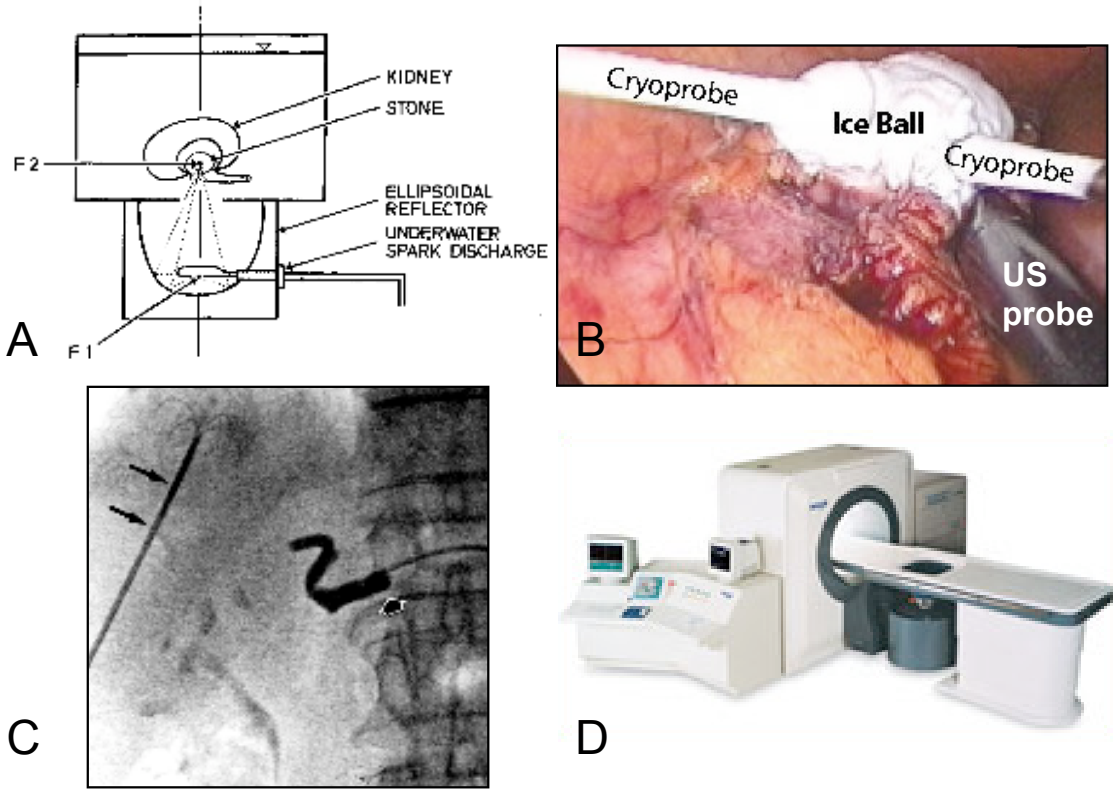

Figure 1.1: Current available minimally invasive or extracorporeal treatments. (a) A schematic of the extracorporeal shock wave lithotripter designed by [6]. (b) An example of cryoablation of an exophytic renal tumor, where two cyroprobes are labeled along with an US probe for real-time monitoring. Adapted from [7]. (c) As seen in this frontal angiogram, an RF probe with deployed hooks, as illustrated by long arrows, is inserted into the nodule of a hepatocellular carcinoma. Blood flow is occluded with a balloon catheter (short arrow) in the hepatic artery [8]. (d) shows the Model JC Haifu system (Chongqing Haifu Technology Co., Ltd., Chongqing, China) used for HIFU treatment [9]. Images were collected from the above cited references.

Among the oldest therapies, cryoablation was conceptually introduced in 1850

[10] and works by freezing (freeze cycle of the freeze/thaw protocol) the target area via a vacuum-insulated cryoprobe tip circulated with liquid nitrogen. The freeze must lower the tissue temperature to -40 to -50°C [11] to ensure complete cell death. In order to treat the entire volume, the portion of the cryoablated lesion, or "iceball" (Fig. 1.1b), at or below the required temperatures must reach the borders of the tumor. Gill et al. [12] extended the iceball to 1 cm beyond each of the 11 tumors included in the study with positive results, though all tumors were small, peripheral, and exophytic. When circulation is restored (thaw cycle), damaged blood vessels caused by the freeze result in edema, vascular occlusion, and thrombosis [7]. Further complications include cracking and bleeding of the renal parenchyma during the thaw phase, which is often mediated with various occlusion methods to achieve hemostasis. Nevertheless, cyroablation has been shown to be relatively effective and safe [7].

Radiofrequency ablation (RFA), which heats tissue to coagulative necrosis, has been in existence since the early 1990s [13], and has shown promise in treatment of hepatocellular carcinoma (HCC), prostate tumors, and breast tumors. RFA involves a percutaneous needle electrode that is inserted into the tumor (Fig. 1.1c) under the guidance of computed tomography (CT) or US. Current flow generated from the electrode deposits RF energy over the immediately surrounding tissue and creates a thermal lesion, which in time results in irreversible cell death [14]. Power ranges from 26-50 W, and frequencies range from 460-500 kHz [7]. High impedances, however, can be caused by tissue desiccation during treatment and limits the size of the lesion. Polascik et al. [15] found that they could also achieve time-dependent and predictably sized lesions in lepus kidneys using a cool-tipped system, where saline was used to couple the electrode to the tissue. Saline was continually infused during treatment, preventing tissue desiccation and consequently, preventing increases in impedance in tissues immediately surrounding the electrode. The RF energy could

then conduct further away without being depleted in high impedance zones.

Focused ultrasound was introduced for therapeutic purposes in the late 1940s [16]. On a global scale, high intensity focused ultrasound (HIFU) is now becoming a well-established clinical method of bloodless noninvasive surgery as US can penetrate through tissue and raise the temperatures in a tight focal region in excess of 56°C [17]. This degree of thermal dosage causes coagulative necrosis and cell death in an area limited by the focal size of the beam. Spatial peak pulse average intensities (I_{SPPA}) range from 1500-2500 W/cm^2 , and duty cycles are normally greater than 50% with pulse durations lasting several seconds. The delineation between healthy and dead cells are on the order of six to ten cells [18][19]. Commercialized units in current clinical use for extracorporeal therapy include the Model JC Haifu system (Fig. 1.1d) from Chongqing Haifu Technology Co., Ltd. (China), ExAblate® 2000 from Insightec, Ltd. (Israel), and the HIFUNIT-9000 from Shanghai A&S Science Technology Develoment Co., Ltd. (China). Applications are numerous and promising, including HCC, uterine fibroids, breast cancer, prostate cancer, bone tumors, and pancreatic carcinoma. Additionally, it can be used for hemostasis to seal blood vessels and prevent excess bleeding in open invasive surgeries [20].

In the United States, companies developing extracorporeal therapeutic ultrasound devices for specific indications have emerged. A few are approved for commercial use by the FDA such as the Sonotherm 600 Ultrasonic Lesion Generating System (Focus Surgery, Inc., Indianapolis, IN) and ExAblate® 2000 (Insightec, Ltd., Israel) for uterine fibroids, but many are in human clinical trials or are approved for use in Europe, Australia, and/or Asia. The first HIFU device approved by the FDA was Sonocare CST-100 Therapeutic Ultrasound System (Sonocare, Inc.) in 1980 and was designed for the treatment of glaucoma. However, the system became outdated by the dominance of laser surgery.

Histotripsy [21], a technology emerging from the University of Michigan, takes

a different route in therapeutic US. Focused US in this case uses low duty cycles and high intensities ($\geq$9000 W/cm^2 I_{SPPA}). Instead of converting ultrasonic energy into heat energy, the chief mechanism takes advantage of the mechanical forces produced by inertial cavitation. The human body is almost devoid of cavitation nuclei, necessitating the use of high intensities; however, histotripsy does not cause thermal leasions, but rather, tissue fractionation. It was found that the temperature rise in *ex vivo* porcine kidneys only increased 6-10°C at the focus [22]. The lesions are repeatable, controllable, and well-defined, where the border of the destruction zones can be on the order of a single cell [23] to delineate live cells from tissue homogenate.

1.3 Renal Cell Carcinoma

The technologies mentioned in the previous sections have been well documented for implementation in the breast, prostate, liver, heart, bone, uterus, and pancreas. However, the kidney is unlike other target applications in its location within the body and its high vascularity (Table 1.1). This section will provide an overview of current methods of treatment for renal cell carcinoma (RCC) along with their implications and then introduce a novel method that can circumvent the challenges confronting other therapies.

Table 1.1: Distribution of systemic blood flow in the human body at rest.

Tissue	**Percentage**
Brain	13
Heart	4
Skeletal Muscle	20
Skin	9
Kidney	20
Abdominal organs	24
Other	10

Table is reproduced from [24].

1.3.1 Current Treatments

The National Cancer Institute estimated that about 51,190 new cases of kidney cancer would arise in 2007 in the United States with an estimated 12,890 total deaths [25]. This incidence of kidney cancer is an increase of 30% from the estimate given for 2006, although the total number of estimated deaths has remained relatively unchanged [26]. RCC accounts for 80-85% of the cases of kidney cancer and has a five-year survival rate of 65% after diagnosis; however, when caught before metastasis, the prognosis improves to a 90% five-year survival [26]. The standard treatment for RCC was initially open radical nephrectomy for containment of the cancer, but it was later shown that there was no significant change in cancer survival for patients who underwent radical nephrectomy versus partial nephrectomy [27]. With no notable disadvantage in terms of cancer treatment, nephron sparing surgery became very desirable because it also considerably reduced the number of cases of renal insufficiency.

Thus, present day treatment for RCC attempts to preserve kidney function if possible and can use minimally invasive techniques such as cryoablation, RFA, microwave and laser thermotherapy, and laparoscopic partial nephrectomies, which are likely to eventually replace conventional open surgery [28]. Two-thirds of new RCC occurrences that are detected while asymptomatic as a result of the improved imaging, half of which are <3 cm [29], have enabled early treatment and improved diagnosis. Because the detectable masses are small, the growth rate of RCCs are slow (0.35 cm/year) [30], and diagnosis is frequently among older patients [29], MIS has been investigated as the preferred mode of treatment. Despite the advantages garnered by MIS, laparoscopic partial nephrectomies are still associated with high morbidity, and other techniques in current clinical use require percutaneous access to the organ and are confined to RCCs no larger than 3 to 4 cm in diameter [31].

These small RCC masses treatable by minimally invasive means would be

appropriate for the size of tumors that are detected in their early stage, but treatment still appears unreliable. In a 3.5 year study of RFA treatment of kidney tumors [13], 36 of the 42 ablated tumors were treated to technical success, which was defined as the absence of tumor enhancement in postoperative magnetic resonance or computed tomography images taken one month after the ablation study. The most successful cases in the study by Gervais et al., though, involved RF ablation of exophytic or parenchymal tumors. Those extending into renal sinus fat had a much lower success rate of 45% of the 11 cases versus 100% of the 31 exophytic or parenchymal cases. Many blood vessels flow near the renal sinus and serve as a heat sink, which limits the maximum achievable temperature and/or the target volume [32]. The resulting lesions are unpredictable in shape and volume, depending on the vascular structure surrounding the tumor.

Cryoablation likewise is confined to small tumors, where larger tumors (>2.5 cm in diameter) may require multiple probes. Despite the success in peripheral and exophytic tumors, tumors deep within the kidney require intrarenal probe placement [33]. It was hypothesized that the cold temperature was dissipated by blood flow [12], but occlusion of the renal artery during cryoablation did not appear to produce any significantly different results [33].

Extracorporeal treatment of the kidney has also proven to be a challenge. HIFU, which has shown success for other indications such as breast or prostate cancer, faces different obstacles for the kidney, which is situated near the ribs, bowel, and lungs, moves with respiration, and is highly perfused [34][35]. With optimization, HIFU in the kidney may prove efficacious, as certain studies have been successful; however, the impact of ablation on the promotion of metastasis due to cell mobilization remains controversial [34]. Minor complications can include skin burns and hematuria, but treatment time and total treatment coverage may still be the larger challenges.

Finally, histotripsy would avoid the problems associated with the “heat sink.”

Since the therapy is not related to heat but instead mechanical disruption, it could prove to be a viable treatment method. While some initial results show that histotripsy does not damage larger vessels, the treatment does disrupt capillaries, which causes minor hemorrhaging thought to be clinically insignificant. Histotripsy research is ongoing, and studies are now being conducted with promising results to evaluate the efficacy of histotripsy in the kidney.

1.3.2 Embolotherapy

Embolotherapy, which is the process of occluding blood flow for therapeutic purposes, can also be used to treat tumors by obstructing the feeder arteries that supply the tumor, thereby inducing ischemia and eventually necrosis [36][37][38]. Vascular embolization was first proposed in 1904 by Dawbain [37] and was executed later in 1960 [39] when embolization of the common carotid artery was performed with positive outcome for a patient with an arteriovenous malformation in the brain. Due to reduced peripheral resistance of the arterial feeders, blood flowed favorably to the malformation [40]; normal blood flow was restored following occlusion of these feeder arteries. Interest in embolotherapy then escalated in 1963 when hemorrhage rates of 0.5 mL/min became detectable [41] with improved imaging, enabling early treatment by means of transcatheter embolization [42]. Advancements in catheter technology and imaging coincided with advancements in occlusion agents in the 1970s, spurring a movement for embolotherapy in interventional radiology [37].

Current Agents and Applications

The current method for embolization involves catherization and placement of occlusion agents in the area of interest. Occlusion agents include metallic microcoils (stainless steel, tungsten, or platinum), acrylic microspheres (embospheres), polyvinyl alcohol particles (PVA), absolute ethanol, and Gelfoam (Pharmacia & Upjohn, Kalamazoo, MI) [43]. Embospheres, which are becoming the preferred

agent, are made from a trisacryl polymer matrix combined with porcine gelatin and are uniform in size to prevent clogging in the catheter. PVA, which have been used since the 1970s are 300-700 μm foam particles, where size varies for different indications. Gelfoam is also made of foam, though they are absorbable and only a temporary occlusion agent. Microcoils [44] and ethanol [45] promote clot formation.

Schwartz et al. [43] gathered data over a 12-year span beginning in 1993 and conducted a retrospective study on renal patients who underwent embolotherapy. From the 121 cases examined, 54.5% had renal artery embolization preceding nephrectomy of their renal masses. These data were collected only within the Weill Medical College of Cornell University (New York, New York) and the popularity of the procedure may be confined to this institution [46]. Nevertheless, it was found that embolized patients experienced less blood loss during resection as well as a reduction in preoperative size and level of tumor thrombus. Controversy pertaining to the necessity of post-embolization nephrectomy remains as the study by Schwartz et al. [43] cites work done by other groups [47] [48], who found no survival benefit when renal artery embolization for metastatic RCC was or was not followed by partial nephrectomy.

Embolotherapy for palliation [37] and to maintain hemostasis due to associated metastases with RCC, however, is common [46][43][49][50]. Emergent traumatic gastrointestinal hemorrhage [51][52][53] as well as obstetric and vascular conditions [54] are among other indications treatable by transcatheter embolization. However, the efficacy of preoperative embolization remains debatable for vascular tumors, as opposing data is found in the literature [54][37]. It is maintained that treatment plans must be patient-based.

Postembolization Syndrome

A common complication resulting from occlusion therapy is postembolization syndrome (PES), which is marked by fever, nausea, vomiting, and flank pain. From

a compiled list generated from the literature comprising 55 patients who were treated for angiomyolipomas, or benign hamartomatous tumors, PES was found to occur in 89% [55] of them. It is thought that PES occurs because of the body's inflammatory response to the necrotic tissue caused by embolization. Symptoms resolve in 1-10 days [55][37] and has in the past been treated with analgesics, but PES can be severe for some patients. Hormone treatment appears to alleviate the effects of PES [55].

1.3.3 Embolotherapy by Acoustic Droplet Vaporization

A novel method to perform embolotherapy was introduced by [56], which provides the groundwork for this dissertation. The work in [56] developed upon a patented concept [57], where a liquid perfluorocarbon (PFC) droplet becomes superheated when placed in an environment above the bulk boiling point of the PFC. This droplet contains a PFC liquid core and is encased in an albumin shell. The shell serves as a stabilizer and prevents evaporation, allowing the droplet to remain stable until perturbed by the environment, when it is subject to vaporization; thus, these droplets are described in [57] as "activatable infusable dispersions." Its activation into a gas bubble in response to an acoustic field is termed acoustic droplet vaporization, or ADV. These droplets expand into gas bubbles that are 5-6 times larger in diameter than the initial droplet [58], and if this were to occur in a capillary, these bubbles would lodge, effectively occluding the blood vessel [59].

In its proposed application for embolotherapy, the process would be entirely extracorporeal. The feeder arteries to the tumor would first be identified and targeted for insonation by a therapeutic transducer. B-mode US by a separate imaging transducer would be aligned with the focus of the therapeutic transducer to provide feedback for correct alignment and successful ADV. For the intended treatment of RCC, current studies have targeted the renal artery [60], but with adequate imaging and careful positioning, segmental arteries isolating different poles of the kidney

should be achievable. Droplets would then be injected intravenously and then insonified once they reached the targeted vessel, where they would subsequently vaporize. This process would continue until occlusion was accomplished. Further therapy could also be achieved when droplets are loaded with potent drugs that would then be locally delivered to the occluded site.

Embolotherapy by ADV can be both extracorporeal and minimally invasive, making it an improvement over current treatments including cryoablation, RF ablation, and transcatheter embolization. Additionally, the treatment is not subject to the problem of the "heat sink," but instead, uses blood flow to its advantage. In fact, ADV can be used as an adjunct to current therapies such as cryoablation, RF ablation, and HIFU by temporarily introducing an embolus to reduce heat dissipation caused by perfusion. In a study combining RFA and balloon catheter embolization (pictured in Fig. 1.1c) [8], lesions ranging from 3.5-5.5 cm in diameter were attained. The maximum lesion diameter was 2.5 cm without embolization in a previous study using the same electrode and technique [61]. Another challenge posed by the kidney, as mentioned previously, is its vulnerability to movement due to respiration. The required amplitude and time-averaged power (30-1200 W/cm^2 I_{SPPA}, 0.3-1.2 W/cm^2 spatial peak temporal average intensity, I_{SPTA}) necessary to achieve ADV are much lower than those required for HIFU or histotripsy, which allows for movement during treatment without the risk of damaging other tissues.

1.4 Overview of Dissertation

The following chapters will take an in-depth look at the strategies that can be used to reduce the input energy required to accomplish *in vivo* and transcutaneous ADV and how the resulting bubbles might by utilized to achieve therapeutic results. Each of the chapters in this dissertation contains appropriate background material for the addressed subject and can therefore be read independently of each other. An

overview of the chapters is outlined below.

Since the intended treatment via ADV is extracorporeal, it is important to counteract the effects of attenuation. It was found that pressure threshold required to induce ADV is inversely related to frequency [62]; however, to be able to penetrate through several centimeters of tissue, a low frequency is optimal. All studies presented in this thesis therefore work in this low frequency regime (750 kHz to 1.5 MHz).

Chapter II focuses on strategies to reduce the ADV threshold. Previous studies [60] have concentrated on high frequencies (3.5 MHz) for proof of principle in small animal models. Full comprehension of the mechanisms involved in ADV has not yet been understood, but the findings in Chapter II elucidate in part the contributors in the process. Appropriate citations for the material in this chapter are:

- A.H. Lo, O.D. Kripfgans, P.L. Carson, and J.B. Fowlkes. "The Effect of Pulse Length on Acoustic Droplet Vaporization." *Proceedings IEEE Ultrasonics Symposium*, pp. 285-286, 2006.

- A.H. Lo, O.D. Kripfgans, P.L. Carson, and J.B. Fowlkes. "Acoustic Droplet Vaporization Threshold: Effects of Ultrasound Contrast Agent and Attenuation." *Proceedings of the 7th International Symposium on Therapeutic Ultrasound*, 2007.

- A.H. Lo, O.D. Kripfgans, P.L. Carson, E.D. Rothman, and J.B. Fowlkes. "Acoustic Droplet Vaporization Threshold: Effects of Pulse Duration and Contrast Agent." *IEEE Transactions on Ultrasonics, Ferroelectrics, and Frequency Control*, 54(5): 933-946, 2007.

These strategies were then translated to an experimental setup that simulated *in vivo* conditions, where an overlying tissue-mimicking phantom attenuated the applied US field. Chapter III discusses efficiency issues in the application of ADV

to *in vivo* conditions. A portion of the material in this chapter is published in the following proceedings article:

- A.H. Lo, O.D. Kripfgans, P.L. Carson, and J.B. Fowlkes. "Acoustic Droplet Vaporization Threshold: Effects of Ultrasound Contrast Agent and Attenuation." *Proceedings of the 7th International Symposium on Therapeutic Ultrasound*, 2007.

Chapter IV explores the potential of the resulting lodged bubbles to alter the acoustic field and explores the applications that the altered field may have. Microbubbles scatter ultrasonic energy, a characteristic that has been employed in the form of ultrasound contrast agents. The larger bubbles created by ADV behave similarly, and their effects can be manipulated for therapeutic purposes. The material in this chapter is published in the following article:

- A.H. Lo, O.D. Kripfgans, P.L. Carson, and J.B. Fowlkes. "Spatial Control of Gas Bubbles and their Effects on Acoustic Fields." *Ultrasound in Medicine and Biology*, 32(1): 95-106, 2006.

Finally, Chapter V provides a summary of the findings in the previous chapters and explores ideas for continuation of this work. Future experiments for further understanding of the process as well as possible improvements for *in vivo* implementation are offered.

REFERENCES

[1] R. W. Chitwood, L. W. Nifong, W. H. H. Chapman, J. E. Felger, B. M. Bailey, T. Ballint, K. G. Mendleson, K. V. B., J. A. Young, and R. A. Albrecht, "Robotic surgical training in an academic institution," *Annals of Surgery*, vol. 234, no. 4, pp. 475–486, 2001.

[2] J. E. Wickham, "Minimally invasive surgery: Future developments," *British Medical Journal*, vol. 308, no. 6922, pp. 193–196, 1994.

[3] M. N. Kiggundu, *Managing Globalization in Developing Countries and Transition Economies: Building Capacities for a Changing World*. Praeger, 2002.

[4] W. Brendel, C. Chaussy, B. Forssmann, and E. Schmiedt, "New method of non-invasive destruction of renal calculi by shock-waves," *British Journal of Surgery*, vol. 66, no. 12, p. 907, 1979.

[5] C. Chuassy, E. Schmiedt, D. Jocham, W. Brendel, B. Forssmann, and V. Walther, "First clinical experience with extracorporeally induced destruction of kidney stones by shock waves," *J Urol*, vol. 127, pp. 417–420, 1981.

[6] C. Chaussy, W. Brendel, and E. Schmiedt, "Extracorporeally induced destruction of kidney stones by shock waves," *Lancet*, vol. 2, pp. 1265–1268, 1980.

[7] K. Perry, A. Zisman, A. J. Pantuck, N. Janzen, P. Schulam, and A. S. Belldegrun, "Laparoscopic and percutaneous ablative techniques in the treatment of renal cell carcinoma," *Reviews in Urology*, vol. 4, no. 3, pp. 103–111, 2002.

[8] S. Rossi, F. Garbagnati, R. Lencioni, H. P. Allgaier, A. Marchiano, F. Fornari, P. Quaretti, G. Di Tolla, C. Ambrosi, V. Mazzaferro, H. E. Blum, and C. Bartolozzi, "Percutaneous radio-frequency thermal ablation of nonresectable hepatocellular carcinoma after occlusion of tumor blood supply," *Radiology*, vol. 1217, pp. 119–126, 2000.

[9] Model JC Haifu system, http://www.hifucancertreatment.co.uk.

[10] J. Arnott, "Practical illustrations of the remedial efficacy of a very low or anaesthestic temperature in cancer," *Lancet*, vol. 2, p. 257259, 1850.

[11] J. Baust, A. A. Gage, H. Ma, and C. M. Zhang, "Minimally invasive cryosurgery-technological advances," *Cryobiology*, vol. 34, no. 4, pp. 373–384, 1997.

[12] I. S. Gill, A. C. Novick, J. J. Sobule, G. T. Sung, E. M. Remer, J. Hale, and C. M. O'Malley, "Laparoscopic renal cryoablation: Initial clinical series," *Urology*, vol. 52, no. 4, pp. 543–551, 1998.

[13] D. Gervais, F. Mcgovern, R. Arellano, W. Mcdougal, and P. Mueller, "Renal cell carcinoma: Clinical experience and technical success with radio-frequency ablation of 42 tumors," *Radiology*, vol. 226, no. 2, pp. 417–424, 2003.

[14] T. Hsu, M. E. Fidler, and I. Gill, "Radiofrequency ablation of the kidney: Acute and chronic histology in porcine model," *Urology*, vol. 56, no. 5, pp. 872–875, 2000.

[15] T. J. Polascik, U. Hamper, B. R. Lee, Y. Dai, J. Hilton, C. A. Magee, J. K. Crone, M. J. Shue, M. Ferrell, V. Trapanotto, M. Adiletta, and A. W. Partin, "Ablation of renal tumors in a rabbit model with interstitial saline-augmented radiofrequency energy: Preliminary report of a new technology," *Urology*, vol. 53, no. 3, pp. 465–470, 1999.

[16] J. G. Lynn, R. L. Zwemer, A. J. Chick, and A. E. Miller, "A new method for the generation and use of focused ultrasound in experimental biology," *J. Gen. Physiol.*, vol. 26, pp. 179–193, 1942.

[17] G. R. ter Haar, "Review article: Therapeutic application of ultrasound," *Progress in Biophysics and Molecular Biology*, vol. 93, pp. 111–129, 2007.

[18] G. R. ter Haar and D. Robertson, "Tissue destruction with focused ultrasound *in vivo*," *Eur. Urol.*, vol. 23 (Suppl. 1), pp. 8–11, 1993.

[19] G. R. ter Haar, "Ultrasound focal beam surgery," *Ultrasound Med Biol*, vol. 21, pp. 1089–1100, 1995.

[20] C. Lafon, B. Bouchoux, F. Murat, A. Birer, Y. Theillere, J. Chapelon, and C. D., "High intensity ultrasound clamp for bloodless partial nephrectomy: *In vitro* and *in vivo* experiments," *Ultrasound Med Biol*, vol. 33, no. 1, pp. 105–112, 2007.

[21] Z. Xu, A. Ludomirsky, L. Y. Eun, T. L. Hall, B. C. Tran, J. B. Fowlkes, and C. C. Cain, "Controlled ultrasound tissue erosion," *IEEE Transactions on Ultrasonics Ferroelectrics and Frequency Control*, vol. 51, no. 6, pp. 726–736, 2004.

[22] W. W. Roberts, T. L. Hall, K. Ives, J. S. J. Wolf, J. B. Fowlkes, and C. A. Cain, "Pulsed cavitational ultrasound: A noninvasive technology for controlled tissue ablation (histotripsy) in the rabbit kidney," *J Urol*, vol. 175, no. 2, pp. 734–738, 2006.

[23] J. E. Parsons, C. A. Cain, G. D. Abrams, and J. B. Fowlkes, "Pulse cavitational ultrasound therapy for controlled tissue homogenization," *Ultrasound Med Biol*, vol. 32, no. 1, pp. 115–129, 2006.

[24] A. Vander, J. Sherman, and D. Luciano, *Human Physiology: The Mechanisms of Body Function*. McGraw Hill, 8th ed., 2001.

[25] American Cancer Society, *Cancer Facts and Figures: 2007*. American Cancer Society, 2007.

[26] American Cancer Society, *Cancer Facts and Figures: 2006*. American Cancer Society, 2006.

[27] R. Uzzo and A. C. Novick, "Nephron sparing surgery for renal tumors: Indications, techniques, and outcomes," *J Urol*, vol. 166, no. 1, pp. 6–18, 2001.

[28] J. Wolf, J. S., "Evaluation and management of solid and cystic renal masses," *J Urol*, vol. 159, no. 4, pp. 1120–1133, 1998.

[29] M. Marberger, G. Schatzl, D. Cranston, and J. E. Kennedy, "Extracorporeal ablation of renal tumours with high-intensity focused ultrasound," *BJU Int.*, vol. 95, Supplement 2, pp. 52–55, 2005.

[30] M. A. Bosniak, G. A. Krinsky, and J. Waisman, "Management of small incidental renal parenchymal tumors by watchful waiting in selected patients based on observation of tumor growth rates," *J Urol*, vol. 155, p. 574A, 1996.

[31] F. Wu, Z. B. Wang, W. Z. Chen, J. Bai, H. Zhu, and T. Y. Qiao, "Preliminary experience using high intensity focused ultrasound for the treatment of patients with advanced stage renal malignancy," *J Urol*, vol. 170, no. 6, pp. 2237–2240, 2003.

[32] S. N. Goldberg, P. F. Hahn, K. K. Tanabe, P. R. Mueller, C. A. Schima, W Athanasoulis, C. C. Compton, L. Solbiati, and G. S. Gazelle, "Percutaneous radiofrequency tissue ablation: Does perfusion-mediated tissue cooling limit coagulation necrosis?," *J Vasc Interv Radiol*, vol. 9, no. 1, pp. 101–111, 1998.

[33] S. C. Campbell, V. Krishnamurthi, G. Chow, J. Hale, J. Myles, and A. C. Novick, "Renal cryosurgery: Experimental evaluation of treatment parameters," *Urology*, vol. 52, no. 1, pp. 29–34, 1998.

[34] K. U. Köhrmann, M. S. Michel, J. Gaa, E. Marlinghaus, and P. Alken, "High intensity focused ultrasound as noninvasive therapy for multilocal renal cell carcinoma: Case study and review of the literature," *J Urology*, vol. 167, pp. 2397–2403, 2002.

[35] M. Marberger, "Ablation of renal tumours with extracorporeal high-intensity focused ultrasound," *BJU Int.*, vol. 99, pp. 1273–1276, 2007.

[36] T. Boehm, J. Folkman, T. Browder, and M. S. OReilly, "Antiangiogenic therapy of experimental cancer does not induce acquired drug resistance," *Nature*, vol. 390, pp. 404–407, 1997.

[37] W. Castañeda Zúñiga, *Interventional Radiology*. Williams & Wilkins, third ed., 1997.

[38] B. A. Ellman, B. J. Parkhill, P. B. Marcus, T. S. Curry, and P. C. Peters, "Renal ablation with absolute ethanol," *Invest. Radiol.*, vol. 15, no. 5, pp. 416–423, 1984.

[39] A. J. Lussenhop and W. T. Spence, "Artifical embolization of cerebral arteries: report of use in a case of arteriovenous malformation," *Journal of the American Medical Association*, vol. 172, pp. 1153–1155, 1960.

[40] J. M. Shenkin and E. B. Sptiz, "Renal artery embolization: Clinical indications and experience from over 100 cases," *Neurosurg.*, vol. 5, pp. 165–172, 1948.

[41] M. Nusbaum and S. Baum, "Radiographic demonstration of unknown sites of gastrointestinal bleeding," *Surg Forum*, vol. 13, pp. 374–377, 1963.

[42] S. Baum and M. Nusbaum, "The control of gastrointestinal hemorrhage by selective mesenteric arterial infusion of vasopressin," *Radiology*, vol. 98, no. 3, pp. 497–505, 1971.

[43] M. J. Schwartz, E. B. Smith, D. W. Trost, and E. D. J. Vaughan, "Renal artery embolization: Clinical indications and experience from over 100 cases," *BJU Int.*, vol. 99, pp. 881–886, 2006.

[44] T. S. Kim, J. H. Park, Y. Lee, J. W. Chung, and M. C. Han, "An experimental study on thrombogenicity of various metallic microcoils with or without thrombogenic coatings," *Invest Radiol*, vol. 33, no. 7, pp. 407–410, 1998.

[45] B. A. Ellman, C. E. Green, E. Eigenbradt, J. C. Garriott, and T. S. Curry, "Renal infarction with absolute ethanol," *Invest. Radiol.*, vol. 15, pp. 318–322, 1980.

[46] B. K. Somani, G. Nabi, P. Thorpe, J. Hussey, and S. McClinton, "Therapeutic transarterial embolisation in the management of benign and malignant renal conditions," *The Surgeon*, pp. 348–352, 2006.

[47] J. E. Gottesman, E. D. Crawford, H. B. Grossman, P. Scardino, and J. D. McCracken, "Infarction-nephrectomy for metastatic renal carcinoma. southwest oncology group study," *Urology*, vol. 25, pp. 248–250, 1985.

[48] R. C. Flanigan, "The failure of infarction and/or nephrectomy in stage iv renal cell cancer to influence survival or metastatic regression," *Urol Clin North Am*, vol. 14, pp. 757–762, 1987.

[49] N. Kothary, M. C. Soulen, T. W. I. Clark, A. J. Wein, R. D. Shlansky-Goldberg, P. B. Crino, and S. W. Stavropoulos, "Renal angiomyolipoma: Long-term results after arterial embolization," *J Vasc Interv Radiol*, vol. 16, no. 1, pp. 45–50, 2005.

[50] J. Kobak, E. J. Gandras, L. Fleury, J. Macura, and J. Shams, "Embolization for treatment of gastrointestinal hemorrhage secondary to recurrent renal cell carcinoma," *Cardiovasc Intervent Radiol*, vol. 29, pp. 1117–1120, 2006.

[51] C. L. Tillotson, S. C. Geller, L. Kantrowitz, M. R. Eckstein, and A. C. Waltman, "Small bowel hemorrhage: Angiographic localization and intervention," *Gastrointest Radiol*, vol. 13, pp. 207–211, 1988.

[52] M. Okazaki, S. Furui, H. Higashihara, F. Koganemaru, S. Sato, and R. Fujimitsu, "Emergent embolothearpy of small intestine hemorrhage," *Gastrointest Radiol*, vol. 17, pp. 223–228, 1992.

[53] W. T. Kuo, D. E. Lee, W. E. A. Saad, N. Patel, L. G. Sahler, and D. L. Waldman, "Superselective microcoil embolization for the treatment of lower gastrointestinal hemorrhage," *J Vasc Interv Radiol*, vol. 14, no. 12, pp. 1503–1509, 2003.

[54] T. P. Smith, "Embolization in the external carotid," *J Vasc Interv Radiol*, vol. 17, no. 12, pp. 1897–1913, 2006.

[55] J. J. Bissler, J. Racadio, L. F. Donnelly, and N. D. Johnson, "Reduction of postembolization syndrome after ablation of renal angiomyolipoma," *Am J Kidney Diseases*, vol. 39, no. 5, pp. 966–971, 2002.

[56] O. D. Kripfgans, *Acoustic droplet vaporization for diagnostic and therapeutic applications*. PhD thesis, University of Michigan, 2002.

[57] R. E. Apfel, "U.S. patent 5 840 276: Activatable infusable dispersions containing drops of a superheated liquid for methods of therapy and diagnosis," 1998.

[58] O. D. Kripfgans, J. B. Fowlkes, M. Woydt, O. P. Eldevik, and P. L. Carson, "*In vivo* droplet vaporization for occlusion therapy and phase aberration correction," *IEEE Trans Ultrason Ferroelect Freq Control*, vol. 49, no. 6, pp. 726–738, 2002.

[59] A. J. Calderón, J. B. Fowlkes, and J. L. Bull, "Bubble splitting in bifurcating tubes: A model study of cardiovascular gas emboli transport," *J Appl Physiol*, vol. 99, pp. 479–487, 2005.

[60] O. D. Kripfgans, C. M. Orifici, P. L. Carson, K. A. Ives, O. P. Eldevik, and J. B. Fowlkes, "Acoustic droplet vaporization for temporal and spatial control of tissue occlusion: A kidney study," *IEEE Trans Ultrason Ferroelect Freq Control*, vol. 752, pp. 1101–1110, 2005.

[61] S. Rossi, E. Buscarini, F. Garbagnati, M. Di Stasi, P. Quaretti, M. Rago, A. Zangrandi, S. Andreola, D. Silverman, and L. Buscarini, "Percutaneous treatment of small hepatic tumors by an expandable rf needle electrode," *Am J Roentgenol*, vol. 170, pp. 1015–1022, 1998.

[62] O. D. Kripfgans, J. B. Fowlkes, D. L. Miller, O. P. Eldevik, and P. L. Carson, "Acoustic droplet vaporization for therapeutic and diagnostic applications," *Ultrasound Med Biol*, vol. 26, no. 7, pp. 1177–1189, 2000.

CHAPTER II

Acoustic Droplet Vaporization Threshold: Effects of Pulse Duration and Contrast Agent

2.1 Introduction

Embolotherapy describes the obstruction of blood flow in the vasculature, which is caused intentionally for therapeutic purposes. It is currently used in hemorrhage control and has potential utility in cancer therapy, either as an occlusive treatment to effect tissue infarction [1] or in the future, as an adjunct to current treatments such as radiofrequency ablation. A possible implementation of embolotherapy was patented by Apfel et al. [2], who suggested the use of superheated immiscible liquid droplets. Variations of such droplets have already been evaluated as potential ultrasound contrast agents [3], where sub-micron sized droplets of liquid perfluorocarbon (PFC) were in part vaporized prior to injection into the body [4]. Another formulation of droplets presented as embolotherapy agents for acoustic droplet vaporization (ADV) [5] are larger in size (1-10 μm). Injected into the body as stabilized liquid emulsions, they vaporize in response to an acoustic field into gas bubbles that are five to size times [5] larger in diameter than that of the original droplet. ADV has been successfully shown in vivo to produce gas emboli and reduce blood flow [6].

Embolization by ADV is advantageous because it can potentially be performed transcutaneously with essentially no damage outside the treatment region. However, the applied ultrasound must be able to overcome attenuation from tissue when the

target is deep inside the body. Low frequencies are advantageous to reduce the effects of attenuation, which should increase the range of depths and available aperture at which ADV can be accomplished. However, previous studies have shown that the pressures required to produce ADV increase with decreasing frequency [7]. Although the application is therapeutic and the bioeffects of high amplitude exposure perhaps an acceptable consequence, it remains favorable to minimize the amplitudes required to produce the desired effect for the robustness of the technique and from the patient and the logistic perspective. Hardware necessary to generate high pressures may be expensive and/or large for feasible use in the operating room.

In order to use low frequency ultrasound, other parameters may be changed to lower the ADV threshold. It may be possible that inertial cavitation (IC) is linked to ADV, in which case the opposite relationship would exist. Since IC threshold decreases with decreasing frequency, ADV threshold may also lower at a low frequency when droplets are associated with IC. Giesecke et al. [8] showed that the IC threshold in the presence of various PFC droplets is indeed lower at low frequencies when using long millisecond pulses. The use of long pulses may also be advantageous because IC is a stochastic process, and the probability that IC occurs increases the longer ultrasound is applied [9].

This study investigates the effects of pulse duration and IC on ADV. The pressures required to induce each phenomenon were found for ultrasound exposures of microsecond to millisecond pulse durations at a low frequency of 1.44 MHz. Additionally, contrast agents (CAs), which have a low IC threshold, may lower the ADV threshold if in fact the two processes are linked. Therefore, a second experiment measures the ADV threshold when the droplets are in the presence of CAs.

2.2 Materials and Methods

Experiments investigating the effects of pulse duration on ADV threshold and ADV in the presence of CA were conducted in both a static environment and in flow. Table 2.1 summarizes the experimental conditions, including acoustic parameters and method of detection for ADV or IC. Details are described subsequently in this section.

Table 2.1: Summary of Experimental Conditions

Experimental Condition	**Pulse Duration Study**	**Contrast Agent Study [cm/s]**
Static	*Agents*: droplets *Detection*: B-mode, passive detector *Pulse seq.*: single 20 μs - 20 ms tone bursts, multiple pulses	*Agents*: droplets and CA *Detection*: B-mode, passive detector *Pulse seq.*: single 20 ms tone bursts
Flow	*Agents*: droplets *Detection*: B-mode *Pulse seq.*: single 20 μs tone bursts	*Agents*: droplets and CA *Detection*: B-mode *Pulse seq.*: single 20 μs - 20 ms tone bursts **Control*: CA only, 20 ms

Pulse duration experiments examined the ADV threshold when only droplets were present. CA experiments examined the threshold when both droplets and CA were present. A control experiment in which only CAs were exposed to 20 ms tone bursts also is listed.

2.2.1 PFC Droplets

As described in [5], dodecafluoropentane (DDFP) (09-6182, Strem Chemicals, Inc., Newburyport, MA) was combined with a 4 mg bovine albumin (A3803, Sigma-Aldrich, St. Louis, MO) /mL saline solution. The mixture was then shaken for 30 s in a vial mixer (Vialmix, DuPont, Billerica, MA) for droplet emulsification, where the DDFP liquid droplets become encased in albumin shells. The DDFP droplet will remain as a liquid at room temperature and, although DDFP has a boiling point of 29°C, will remain a liquid even at body temperature at 37°C.

At 37°C, DDFP is a superheated liquid that is stabilized against spontaneous evaporation due partially to the albumin shell [5]. All solutions of droplets were pushed through a series of syringe filters (Whatman, Maidstone, UK) so that the maximum droplet diameter was 6 μm [6] in order to accommodate *in vivo* conditions, where droplets must be able to pass through capillaries. A droplet concentration (as determined from samples counted using a hemacytometer imaged under microscopy) of approximately 5.3x10^7 droplets/mL was used in all experiments by diluting the stock droplet solution in de-ionized water. The dilution was then stored in the refrigerator between experiments.

2.2.2 Contrast Agent

In the CA experiments, various concentrations of Definity® contrast agent (Bristol-Myers Squibb Medical Imaging, North Billerica, MA), which are microbubbles consisting of PFC gas in phospholipid shells, were added to solutions with the same concentration of droplet as mentioned above. The concentrations that were used were $10^3, 10^4$, or 10^5 microspheres/mL and were determined according to appropriate dilutions of the concentration of Definity® specified in the package insert. Vials of Definity® were activated several days prior to the experiments and were re-used for separate measurements. PFC gas replaced the headspace as Definity® was aspirated from the vial for each experiment. Unless otherwise specified, further mention of CA will refer to the use of Definity®.

2.2.3 Acoustics

Single tone bursts of 20 μs, 100 μs, 500 μs, 1 ms, 5 ms, 10 ms, and 20 ms in duration and 1000 tone bursts (20 μs each in duration) at a pulse repetition frequency (PRF) of 500 Hz were transmitted at a carrier frequency of 1.44 MHz with an annular transducer (63 mm focal length, 63.5 mm aperture in diameter, 63.5 mm radius of curvature, Etalon 940501, Lebanon, IN). Pressure waveforms at the

spatial peak of the annular transducer were calibrated with an in-house fiber-optic probe hydrophone [10]. Pressure levels ranged from ambient pressure to 6 MPa peak rarefactional pressure (P_r).

To achieve the long pulse durations used in these experiments, a master function generator (Hewlett Packard 33120A, Palo Alto, CA) gated a second slave function generator (Hewlett Packard 3314A, Palo Alto, CA). The slave function generator then output a 1.44 MHz sinusoid to an amplifier (ENI A300, Rochester, NY), which was then sent to the annular transducer. The master function generator also triggered the appropriate detector to begin recording data.

The purpose of the first set of experiments was to explore the effect of pulse duration on ADV threshold; thus, all pulsing parameters described above were measured. In the second set of experiments, which explored the influence of CAs on ADV, only single 20 μs and 20 ms tone bursts were used.

2.2.4 Experimental Setup for Static Experiments

The focus of the annular transducer was positioned inside a closed vessel made of thin-walled dialysis tubing (5 mm diameter, Spectra/Por®, Spectrum Laboratories Inc., Laguna Hills, CA), which was replenished with a new solution of droplets or droplets with CA between each threshold measurement. A piece of sound absorbing rubber (SOAB, BF Goodrich, Jacksonville, FL) was placed at an angle on the distal side of the tube to minimize reflection and the possibility of standing waves. Experiments were performed in 37°C de-ionized water (Ex 7, ThermoNESLAB, Newington, NH). A schematic of the setup is shown in Fig. 2.1a.

Two methods of detection were used, although not concurrently in the actual experiment (Fig. 2.1b). One of these methods used a diagnostic ultrasound imaging system (Diasonics VST Series, Milpitas, CA) with a 10 MHz linear array positioned approximately 30° from the annular transducer, to record B-mode images for

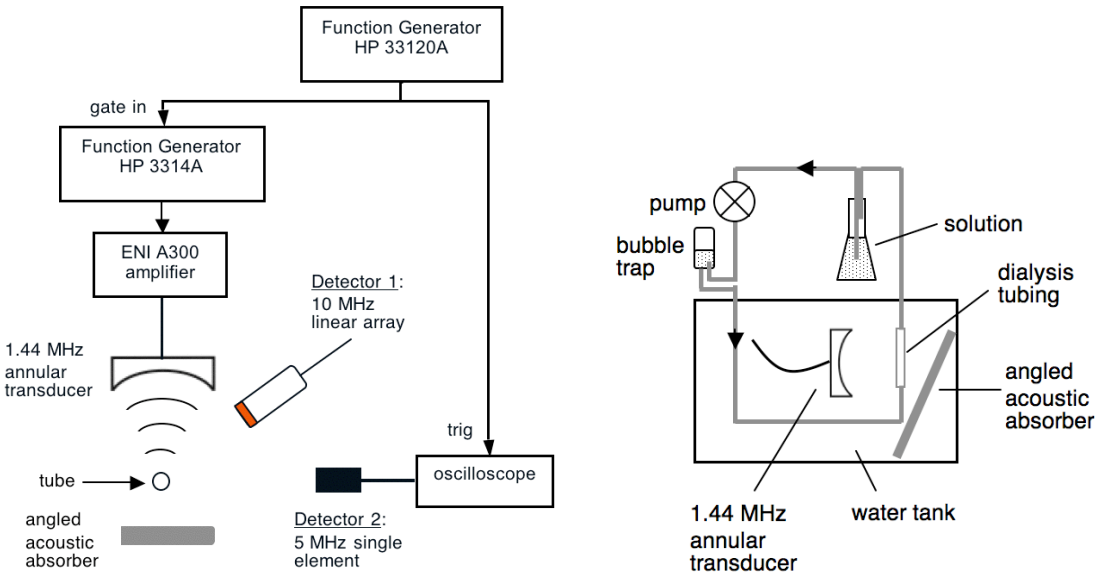

(a) (b)

Figure 2.1: (a) Top view of the experimental setup for measurements performed in a static environment. The therapeutic transducer and the associated electronics necessary to create millisecond pulses are shown. Both methods of detection also are illustrated and labeled as Detector 1 and Detector 2, though they were not used concurrently. (b) Schematic (side view) of the experimental setup used in studies measuring ADV threshold in the presence of contrast agents in a flow environment. Solutions contained either droplets, droplets and $10^3, 10^4$, or 10^5 microspheres/mL of Definity®, or 10^5 microspheres/mL of Definity®. Experiments were performed in 37°C deionized water.

detection of bright echoes from large bubbles created by ADV. The second method was to detect the acoustic emissions from IC, which was achieved with a passive 5 MHz single element transducer (Valpey-Fisher, Hopkinton, MA), positioned 90° from and confocal with the annular transducer. An oscilloscope (Lecroy 9310L, Chestnut Ridge, NY) was triggered with each transmitted pulse and captured the radiofrequency (RF) signals associated with any acoustic emission or scattering. The detectors were positioned as mentioned previously to minimize interference from the direct wave of the annular transducer. Similarly, because of acoustic interference from the linear array, the two detectors were used separately.

Each ADV threshold measurement was conducted as follows. A new sample was loaded into the closed vessel, leaving space at the top for gas expansion. The vessel was then connected to a holder, which oriented the vessel vertically and positioned it so that it coincided with the focus of the annular transducer. Single tone bursts or multiple tone bursts were then transmitted from the annular transducer 10-25 s apart (depending on the pulse duration) with increasing pressure amplitudes. This process was repeated five times for each acoustic parameter.

Once ADV threshold was reached, subsequent measurements at higher pressures were affected since lingering bubbles from the previous pulse facilitated further ADV. Vaporized droplets provided additional cavitation nuclei in the acoustic field of subsequent pulses if they adhered to the tube wall or if enough bubbles were produced that they could not clear the beam before the next pulse. Since we were only concerned with measuring the ADV threshold, the interference from remaining bubbles with successive pulses at super-threshold amplitudes did not affect the determined threshold.

Table 2.1 shows that both solutions (droplets and droplets with CA) were performed in a static environment. The majority of pulse duration experiments involving only droplets were performed in a static environment, though a limited

number of experiments were performed in flow for a comparison of the two environments. However, a static environment is not optimal when CAs are present because it is difficult to achieve a homogeneous distribution of CA and droplets due to a difference in buoyancy. Therefore, only a limited number of experiments with CA and droplets were performed in a static environment.

2.2.5 Experimental Setup for ADV in Flow

The circulating flow system is shown in Fig. 2.1b. A solution of droplets ($5.3\text{x}10^7$ droplets/mL), droplets and CAs ($10^3, 10^4$, or 10^5 microspheres/mL), or CA only (10^5 microspheres/mL) were continuously stirred in a reservoir and circulated via a peristaltic pump (Masterflex® pump and speed controller, Cole-Parmer, Chicago, IL) and tubing (Tygon®, Saint-Gobain Performance Plastics Co., Akron, OH) through the focus of the annular transducer, where a segment of dialysis tubing provided acoustic access. The pump setting was chosen to achieve a slow average flow velocity of 3.75 cm/s, which was calculated from a calibration of the volume flow rate of the pump and cross-sectional area of the tube, in order to maximize opportunity for ADV and for comparison to static experiments. Pulsatility of the flow was reduced by including an in-line capacitor in the flow system. The solution, which was first immersed and allowed to equilibrate to the 37°C tank water, was changed between each experiment. For each experiment, two pulses were transmitted one second apart at a specific amplitude, and the next pair of pulses were fired after five seconds. This cycle was repeated with increasing pressure amplitudes in both coarse (∼170 kPa) and fine steps (∼40 kPa) to encompass a large range (0.22-4.43 MPa) and to refine the threshold measurement in a small range (0.22-1.24 MPa), respectively. These experiments were repeated five times. Thus, 10 measurements were taken at each pressure in each of the two amplitude ranges, although 20 measurements existed for pressures that were equivalent in the separate ranges.

Only one detection method was used in these experiments. In flow, moving scatterers would introduce additional noise into the RF signals that are detected by the passive transducer, significantly reducing the signal to noise ratio (SNR). Therefore, B-mode images were used to make threshold measurements.

To maintain a nominally homogenous distribution of CA and droplets and to correctly characterize their behavior in concert, the majority of CA experiments were performed in flow. These solutions were exposed to 20 ms tone bursts, although an additional experiment of 10^5 microspheres/mL and droplet solutions were exposed to 20 μs pulses for a comparison of the effect on threshold due to short pulse duration in the presence of CAs. An experiment where only droplets were exposed to 20 μs tone bursts was also performed as mentioned in the previous section.

Although CAs are echogenic and provide substantial signal, scattering from bubbles with larger cross-sectional area produced by ADV are distinguishable in B-mode. The focus of the 10 MHz linear array was positioned on the proximal side of the tube and the output power was maintained at a low setting, thereby (1) reducing the signals from CA microbubbles while still detecting signal from ADV bubbles and (2) reducing the possibility of destroying CA and/or affecting the threshold measurement. Because the ADV threshold is low at a frequency of 10 MHz [7], the linear array itself is also capable of vaporizing droplets.

2.2.6 Analysis of B-mode Images

B-mode images recorded during the pulse duration and CA studies were analyzed for echoes from ADV bubbles, which appear as bright pixels in the image when compared to the background. Detection for the presence of these echoes was evaluated in terms of mean echo amplitude (MEA) in a given region of interest (ROI) and is described in [5]. The ROIs, each consistent in size for a given study, were positioned next to the focus of the annular array in the image and in the direction

of movement of the bubbles produced by ADV. For the static pulse duration study, the ROIs were positioned above the focus so that rising bubbles could be detected, and for the CA study where the droplets and CA were flowing, the ROIs were positioned downstream of the focus. The signal level at each pixel in the ROI was then linearized assuming a simple log compression. The MEA, or the mean of the decompressed pixel signal levels in an ROI, was then calculated and compared to a baseline MEA value when no pulses were transmitted in order to detect a rise in MEA and therefore the occurrence of ADV. Separate explanations of how this analysis for the two studies was evaluated are described in further detail in the Results section.

2.3 Results

2.3.1 Analysis for Pulse Duration Measurements

Detection with Imager

As described previously, the MEA for each B-mode image was computed. In this pulse duration study, the MEAs for all images in a given cineloop were averaged. A baseline mean MEA was then subtracted to compute the relative echo amplitude (REA), which was then plotted as a function of peak P_r (Fig. 2.2). A large change in REA indicates the ADV threshold. Therefore, the derivative of the REA vs. P_r curve was taken to detect a change in slope. The point where the change in slope exceeded a certain criterion was designated the threshold. This criterion was established empirically from a small subset of the data and was subsequently applied to all data. The ADV thresholds were then plotted in terms of pulse duration (Fig. 2.3).

Each data point found in Fig. 2.2 shows the result of consecutive pulses that increase in amplitude; therefore, these plots reflect the REA as a function of both time and pressure amplitude. If REA before the apparent ADV event is an indication

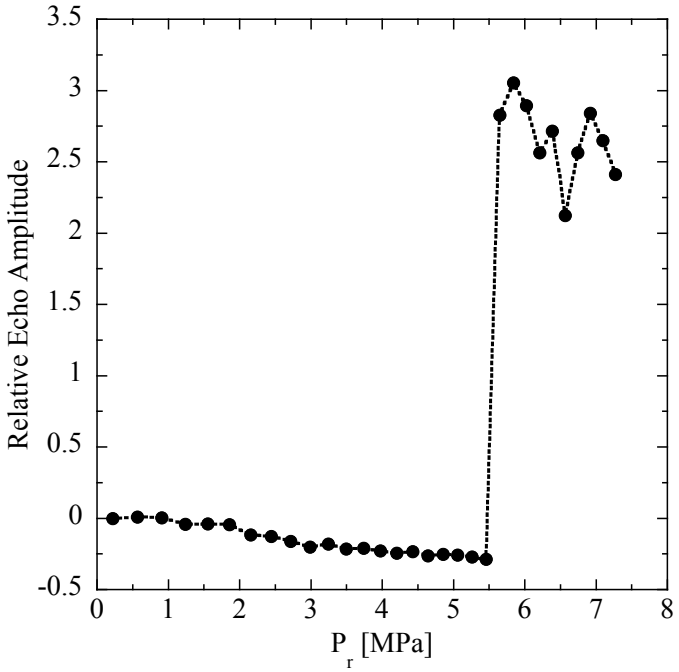

Figure 2.2: Example of REA against P_r for 500 μs pulses. The sharp change in slope at approximately 5.5 MPa reflects a rise in REA due to bubbles created by ADV.

of the droplet concentration, Fig. 2.2 shows a decrease in droplet concentration as a function of time, which is expected since DDFP droplets have a higher density (C_5F_{12}, 1.6 kg/m^3) than water and would therefore settle to the bottom. However, no correlation was found between any apparent variation in droplet concentration and ADV threshold found in the data.

The placement of the ROIs vertically above the focus in the B-mode images was important in order to detect rising bubbles. At near-threshold amplitudes, long millisecond pulses created echogenic scatterers, which could be misinterpreted as echogenic bubbles if they did not fall with gravity. Three frames in a B-mode cineloop illustrating this process are shown in Fig. 2.4(a). One hypothesis is that these sinking scatterers are DDFP droplet aggregates similar in concept to aggregated forms of CAs during an acoustic pulse [11]. Further experiments would be needed to test this hypothesis. The formation of such scatterers, henceforth

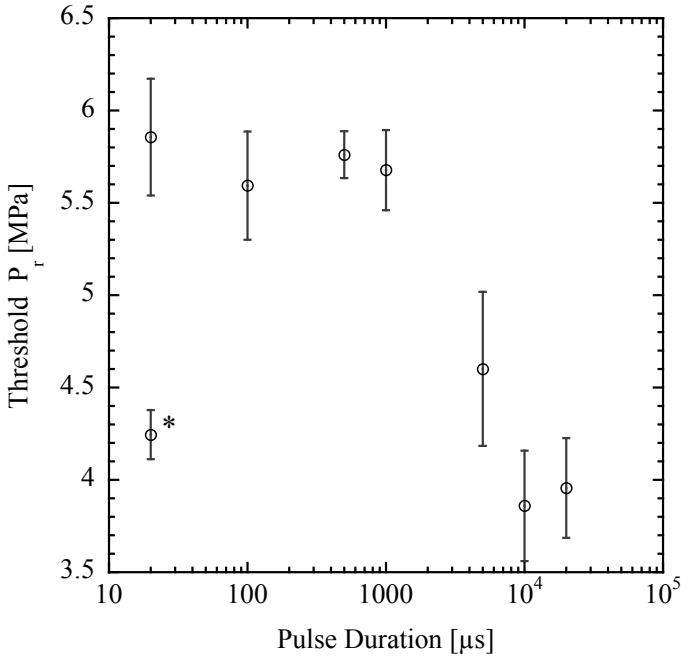

Figure 2.3: Threshold in P_r as detected in B-mode images. Error bars reflect the standard error of the mean. $(*)$ Refers to 1000 pulses (20 μs each in duration) at a PRF of 500 Hz. All other data points are the thresholds for single pulses with pulse durations indicated along the abscissa.

referred to as sinking scatterers, only occurred during millisecond pulses. For super-threshold amplitudes, ADV was confirmed with the persistence of bubbles after insonification. Fig. 2.4(b) shows three frames after a super-threshold pulse was transmitted. Echogenic scatterers seemed to disperse above and below the focus due to radiation force (Frame 3), but scatterers in this case moved against gravity, confirming the production of ADV bubbles (Frames 10 and 20).

Passive Detection

A 5 MHz single element transducer recorded the acoustic emissions and scattering to detect IC. IC is defined as the growth and the subsequent collapse of a gas bubble during an ultrasonic wave. Its acoustic emission is characterized by the appearance of broadband noise. To specifically identify such an event, the Fourier transform was computed for the entire RF waveform, and two frequency bands were analyzed by

the techniques described in [12], where the root-mean-square (RMS) was calculated to quantify spectral content. These values were then plotted as a function of P_r. To detect broadband noise, a frequency band between 2 and 2.4 MHz was chosen because it lies between the fundamental frequency at 1.44 MHz and the second harmonic at 2.88 MHz. A smaller more specific frequency band (between 0.7 and 0.74 MHz) was chosen to detect the subharmonic frequency at 0.72 MHz, which is an indicator of the presence of bubbles. Bubbles in this case may be created either by cavitation or ADV.

Two curves were then generated for each experiment. The RMS values for the two frequency bands described above were plotted as a function of P_r. Fig. 2.5a is a plot of the RMS values of the subharmonic range. Unlike the plots measuring REA (Fig. 2.2), the plots for spectral content varied from experiment to experiment due to variability in the number of inertial cavitation events that may occur with each tone burst and also between the different pulse durations. Therefore, a criterion computed from the baseline or pre-threshold RMS value was used for each separate experiment. A histogram for each curve like that in Fig. 2.5b was used to determine the baseline value. Since the increase in acoustic emission within a band is significant, a bimodal distribution should exist. RMS values for a baseline value are then determined and used as the criteria for ADV threshold as indicated by the dotted line (Fig. 2.5a) and arrow (Fig. 2.5b).

Because of the statistical nature of IC, some events occurred at low amplitudes. For example, a spike in RMS that met the criterion for ADV may have occurred but did not recur with the following pulse at a higher amplitude. In order to choose a threshold value that would reliably predict when IC would occur, these events were not considered threshold. We required that at least two consecutive events occur to be classified as threshold. Therefore, a median filter of size three was used (Eq. 2.1).

$$y_i = median(x_i, x_i + 1, x_i + 2), i = [1, N - 2] \tag{2.1}$$

Once the median value y_i met the criteria, a threshold was determined. Fig. 2.6 shows the mean IC threshold for five measurements taken for each pulse duration. Thresholds detected by both the presence of subharmonics and broadband noise are shown.

Effects of Total "on-time" on Cavitation

To visualize the occurrence of IC and how it relates to pulse duration and on-time, time-frequency plots were generated from the RF waveforms for both 20 ms pulses and for 1000 pulses (20 μs each in duration). These two pulse sequences have the same on-time, which is the cumulative duration of all tone bursts. Fig. 2.7a shows three examples of scattering from 20 ms pulses at different amplitudes, and Fig. 2.7b shows four examples from the series of 20 μs pulses also at different amplitudes. Time-frequency plots for 20 ms pulses were generated by short time Fourier transforms with the spectrogram function in Matlab (The Mathworks, Inc., Natick, MA) using 20 μs segments for comparison between the two pulse sequences. RF waveforms in Fig. 2.7b were acquired in segmentation mode on the oscilloscope, and each segment was time-gated to capture only the scattering during the short transmitted pulse. Fourier transforms were then taken of each segment and also displayed against time in Fig. 2.7b. Fig. 2.7c shows the results for 3.24, 4.20, and 4.85 MPa in Fig. 2.7b when the baseline spectrum (from the first time segment) is subtracted from each of the spectra of the remaining pulses in the sequence.

2.3.2 Analysis for CA Studies

Similar to the analysis performed on the B-mode images in the pulse length studies, ROIs were drawn in the images to detect a rise in pixel intensity and therefore bubble production. In flow experiments, any bubbles created by ADV would be quickly carried away after each pulse due to flow instead of buoyancy. Therefore, an ROI positioned downstream of the focus was used to capture the

transit of the ADV bubbles. Fig. 2.8 shows the MEA of such an ROI and how it changes with time. The steady-state MEA can be seen during the first nine frames and is then followed by two transient increases in MEA that characterize the passage of bubbles and therefore successful ADV. Acoustic interference from the annular transducer manifesting as white bands in the B-mode image is seen in frames 10, 11, 30, and 31, and the corresponding MEAs are therefore omitted from the MEA vs. time plots.

From these plots, a threshold can be determined. Since the occurrence of each of the two pulses is known beforehand, time intervals for a baseline MEA (first nine frames), first pulse (frames 12-15), and second pulse (frames 32-35) can be defined. Thus, MEA of the first and second pulses can be compared and evaluated for successful ADV according to a threshold criterion computed from the statistics of the baseline. Calculation of the criterion for ADV threshold is described as follows.

An accurate depiction of the baseline MEA was first obtained. Bubbles unassociated with ADV occasionally traveled through the acoustic window, were recorded in the B-mode cineloops, and were represented as aberrant spikes in the MEA vs. time plots. These bubbles appeared to be vapor bubbles that formed in tubing located beyond the acoustic beam. By comparing only the frames that were expected to reflect either the first pulse (frames 12-15) or second pulse (frames 32-35) to the baseline (frames 1-9), the probability that these spurious bubbles would affect ADV detection was minimized. However, these bubbles can skew the data if they appeared in the time frame used to calculate a baseline value. In order to accurately represent the baseline value, an outlier detection method was used to identify spikes in MEA in the baseline time interval and remove them from further calculations.

The box plot method, a standard method used for outlier detection, was applied to the first nine MEA data points to detect an outlier. The points were first rearranged in ascending order such that $x_1 < x_2 < \ldots x_8 < x_9$. The interquartile

range (IQR) was defined as $Q_{0.75} - Q_{0.25}$, where $Q_{0.25} = 1/2 \cdot (x_2 + x_3)$ and $Q_{0.75} = 1/2 \cdot (x_7 + x_8)$. An outlier was detected if it exceeded $1.5 \cdot IQR$ above the third quartile, $Q_{0.75}$. Bubbles unassociated with ADV typically appeared as single spikes (echogenic bubbles that raise the MEA), so the criterion was only applied for the highest data point, or x_9. Therefore, if $x_9 > 1.5 \cdot IQR + Q_{0.75}$, then x_9 was an outlier and discarded from the baseline measurement. Outliers were detected 5% of the time when using this method.

After any potential outliers were removed, the mean and standard deviation (SD) were calculated for the baseline. An ADV event occurred if the MEA associated with a pulse exceeded a criterion, which was computed from the mean and SD of the MEA baseline values and which was assessed for reliability as follows. The results (N=10 or 20 as explained in the Methods section) according to various criteria, which differed only in the number of SDs above the mean, were compiled and plotted as a probability for each P_r and for each CA concentration ($10^3, 10^4$, or 10^5 microspheres/mL) in Fig. 2.10a). To evaluate the reproducibility of the results, we compared the results of an applied criterion with predictions based on a binary logistic regression model (SPSS Ver.14, Chicago, IL) (Eq. 2.2). The predictors in the binary logistic regression were based on exogenous factors including the concentration of CA and applied pressure. The model is expressed below,

$$\ln \frac{P(E)}{1 - P(E)} = m_1 + m_2 \cdot I_1 + m_3 \cdot I_2 + m_4 \cdot p \tag{2.2}$$

where m_1, m_2, m_3, m_4 are constants, I_1 and $I_2 = 0$ *or* 1 and are indicators for CA concentration, and p is pressure. Though the agreement between the results using a specified criterion was high (>90%) when the number of standard deviations varied between three and eight, the best overall results were obtained with a criterion MEA that exceeded the mean by five SDs (Fig. 2.9). The model is plotted alongside the data in Fig. 2.10a using a five SD criterion and shows 50% probability of

vaporization at 0.67, 0.51, and 0.41 MPa and 95% probability at 2.0, 1.92, and 1.8 MPa for CA concentrations of $10^3, 10^4$, and 10^5 microspheres/mL, respectively. All results are statistically significant ($p<0.01$). A control experiment that measured the threshold in a solution with only 10^5 microspheres/mL of CA and no droplets was evaluated according to the same five SD criterion and plotted with the previous data (Fig. 2.10b). The threshold for the control experiment is substantially higher than those for solutions containing both droplets and CA of any concentration, suggesting that the thresholds measured here are in fact due to ADV and not the CA themselves. Fig. 2.11a also further supports this argument in that a highly echogenic signal appears only with the combination of droplets and CA, whereas insonation at the same pressure amplitude actually decreases the signal level when only CA are present (Fig. 2.11b). In addition, the thresholds measured when only CAs are present may only reflect an increase in echogenicity due to CA aggregates [11] that form in the side lobes of the acoustic beam (Fig. 2.11c).

2.3.3 ADV in Flow (Droplets Only)

A comparison was also made to observe any effects of flow on ADV. Fig. 2.12 shows the results of an experiment with only droplets in flow along with the ADV threshold found in the static experiments for 20 μs pulses. Because of the possibility of forming echogenic scatterers other than ADV bubbles during long 20 ms pulses, it would be difficult to differentiate between the bright echoes due to bubbles and those due to sinking scatterers in flow since both move in the direction of flow. Therefore, 20 μs pulses were used for this comparison. Fig. 2.12 shows that an average flow velocity of 3.75 cm/s does not significantly affect ADV threshold for 20 μs pulses, the shortest tone burst used in this paper. Because the annular transducer has a 6 dB lateral beam width of 1.14 mm and a single droplet will have moved 750 nm in 3.75 cm/s flow, nominally all droplets in the beam will have been exposed to the

entire 20 μs pulse. Thirty-four percent of the droplets in the 6 dB lateral beam width will have been exposed to an entire 20 ms pulse, which may result in an elevated threshold measurement due to limited detector sensitivity. Additionally, the results for an ADV threshold experiment for 20 μs pulses in the presence of CA were plotted in Fig. 2.12, illustrating a reduction in threshold for short pulses as well.

2.3.4 ADV in a Static Environment (Droplets and CA)

A limited number of experiments with CAs (10^5 microspheres/mL) and droplets were performed in a static environment with 20 ms pulses since, as mentioned previously, it is difficult to differentiate bubbles from sinking scatterers in a flow environment. From these static experiments, we can confirm from B-mode cineloops that at 0.43 MPa, echogenic scatterers rise after insonification. This is the same pressure that generates echogenic scatterers in a flow experiment and is approximately 20% that of the pressure required to generate sinking scatterers in a static environment. The results from the static case support the claim that the echogenic scatterers detected in the flow environment are in fact buoyant bubbles produced by amplitudes as low as 0.43 MPa (MI=0.4).

Passive detection of acoustic scattering was also used in these limited static experiments where droplets were mixed with CA at a concentration of 10^5 microspheres/mL. The apparent threshold for broadband noise in these experiments was approximately 0.8 MPa, which is just above the range of the transition of probability from 0 to 1 in the flow experiments. This difference may be due to the inhomogenous distribution of CAs and droplets, which results from a difference in buoyancy and consequently a separation of material. The elevated threshold is not likely due to a difference in detector sensitivity since there is good agreement between the thresholds detected by the imager and passive detector in the static experiments (Figs. 2.3, 2.6). Nevertheless, these results indicate that IC is occurring

at these low pressure amplitudes.

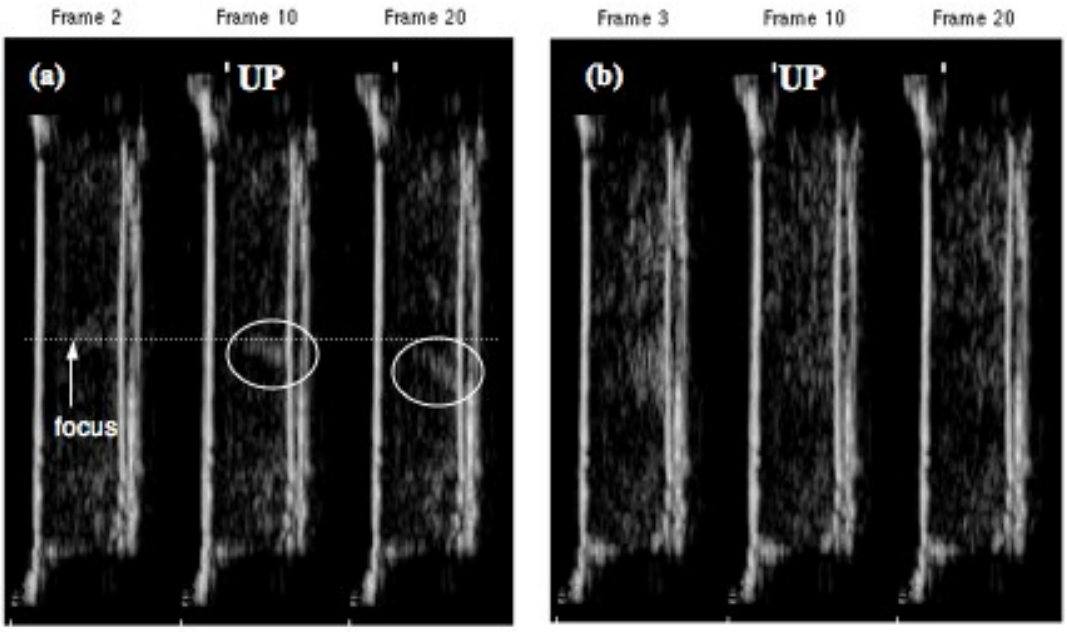

Figure 2.4: (a) Sequential frames of a B-mode movie show effects of a 20 ms pulse at 1.86 MPa P_r . Frame 2 immediately follows the tone burst in Frame 1, during which acoustic interference was seen and thus is not shown here. The tube was oriented vertically, and the imager as well as the annular transducer was positioned to the left of these images. Echogenic scatterers, nonbubbles, sink toward the bottom of the tube as indicated by the circles in Frames 10 and 20. (b) Sequential frames of a B-mode cineloop show effects of a 20 ms pulse at 3.74 MPa P_r . Frame 3 immediately follows the tone burst, during which acoustic interference was seen. Acoustic interference may span from one to two frames; in this case, interference spanned from Frame 1 to 2. Due to radiation force, the echogenic scatterers were pushed against the tube wall, then dispersed above and below the beam. However, the scatterers in these images rise toward the top against gravity, indicating the creation of bubbles, and therefore, the occurrence of ADV.

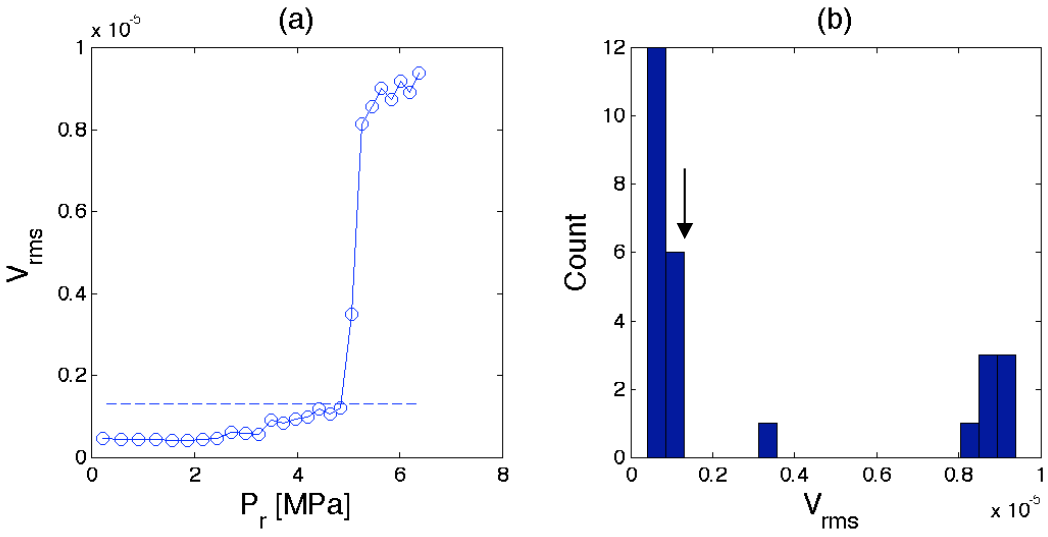

Figure 2.5: ADV threshold experiment for 10 ms tone bursts. (a) Example of the spectral content of a subharmonic frequency band in terms of V_{rms} plotted against P_r. A histogram of the V_{rms} values is seen in (b), in which the lowest V_{rms} values can be separated (↓) as the baseline values. V_{rms} values greater than the baseline value (-) are determined as above threshold.

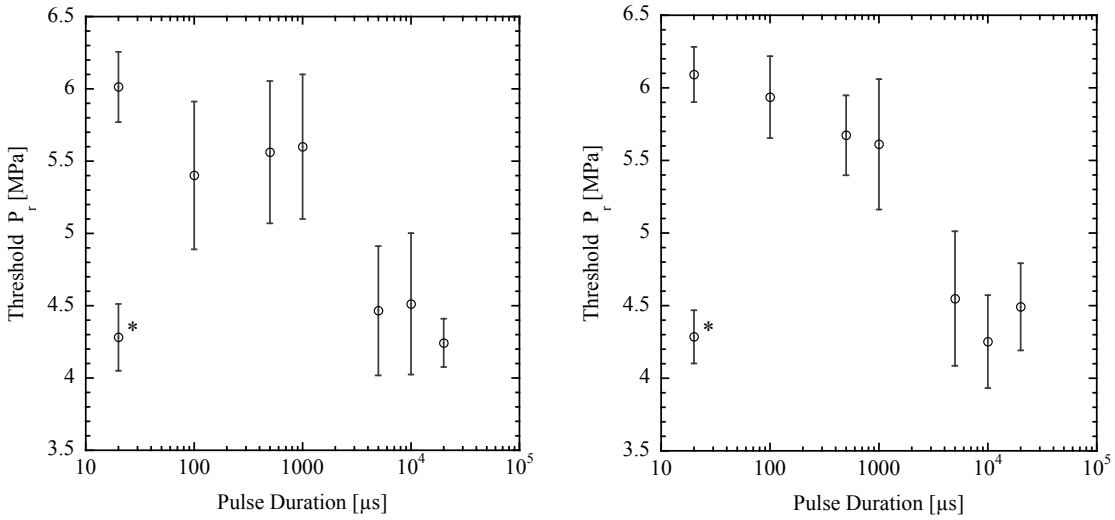

Figure 2.6: Threshold in P_r as detected by the passive 5 MHz passive transducer. Error bars reflect the standard error of the mean. (∗) Refers to 1000 pulses (20 μs each in duration) at a PRF of 500 Hz. (a) Shows threshold measurements based on RMS values of the subharmonic range from 0.7-0.74 MHz. (b) Shows threshold measurements based on the presence of broadband noise.

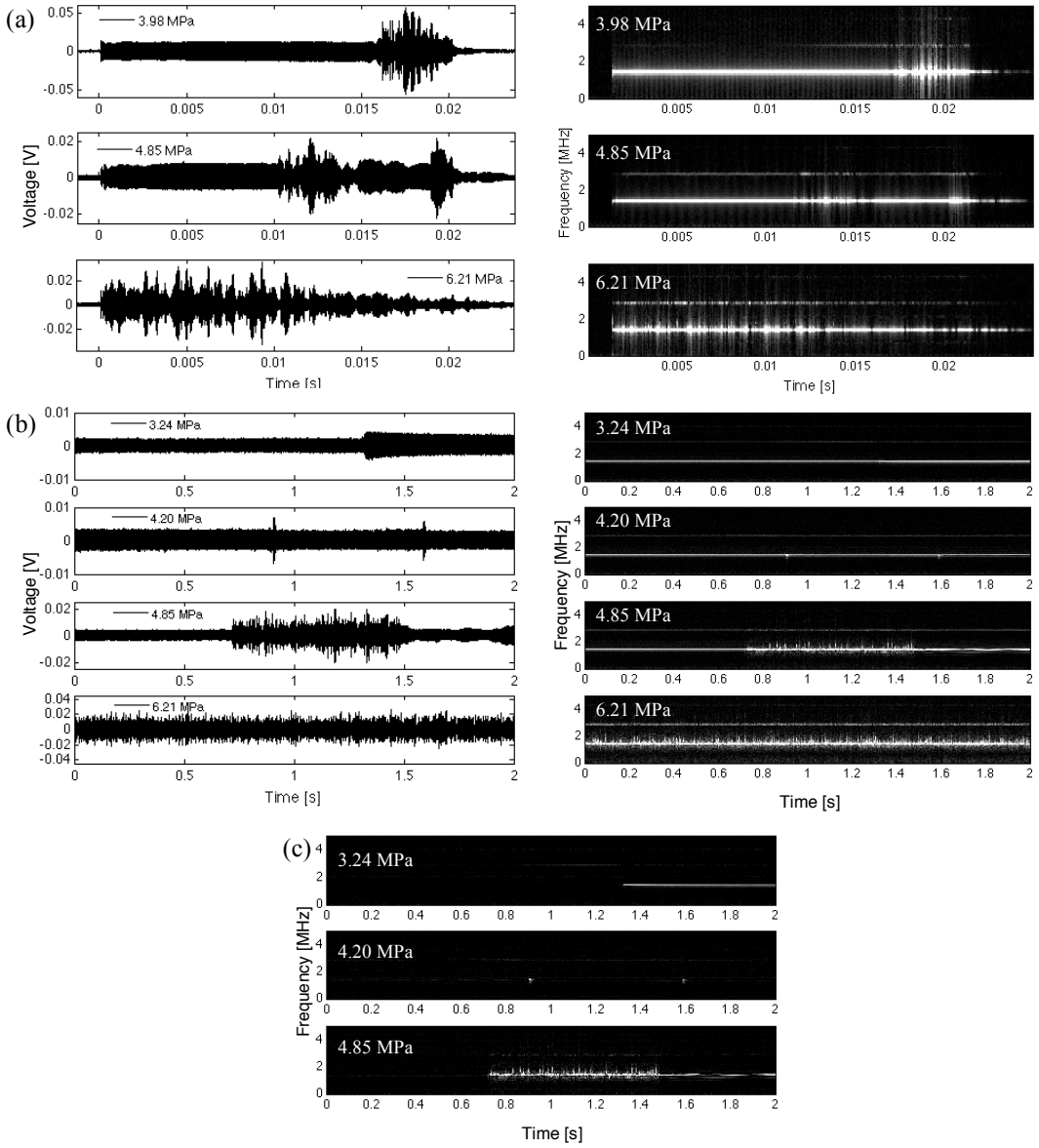

Figure 2.7: RF signals are displayed for single (a) 20 ms tone bursts and for (b) 1000 pulses (20 μs each in duration) at a PRF of 500 Hz for various pressure amplitudes. The associated time-frequency plots of the acoustic emissions are shown to the right in (a) and (b). (a) Examples of scattering at pressures above ADV threshold. (b) Four examples of RF signals, for which 3.24 and 4.20 MPa are considered below ADV threshold and 4.85 and 6.21 MPa are considered above threshold. (c) Better illustrates the change in time-frequency plots for waveforms in (b) when subtracting the spectra of the scattering from the first 20 μs pulse. The time-frequency plot for 6.21 MPa is not shown in (c) because there is no clear baseline spectrum because IC is occurring during the entire pulse sequence.

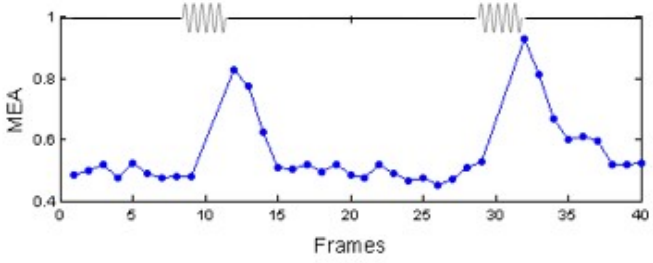

Figure 2.8: Data points reflect the MEA of a given ROI through consecutive frames in a B-mode cineloop. Statistics drawn from the mean MEA of the baseline, defined here as the first nine data points, are used as criteria for ADV detection. Pulses of the same amplitude are shown on the top and illustrate the timing of the pulse firing during a given cineloop. Frames associated with acoustic interference with the passive detector during pulse transmission are omitted (10, 11, 30, and 31).

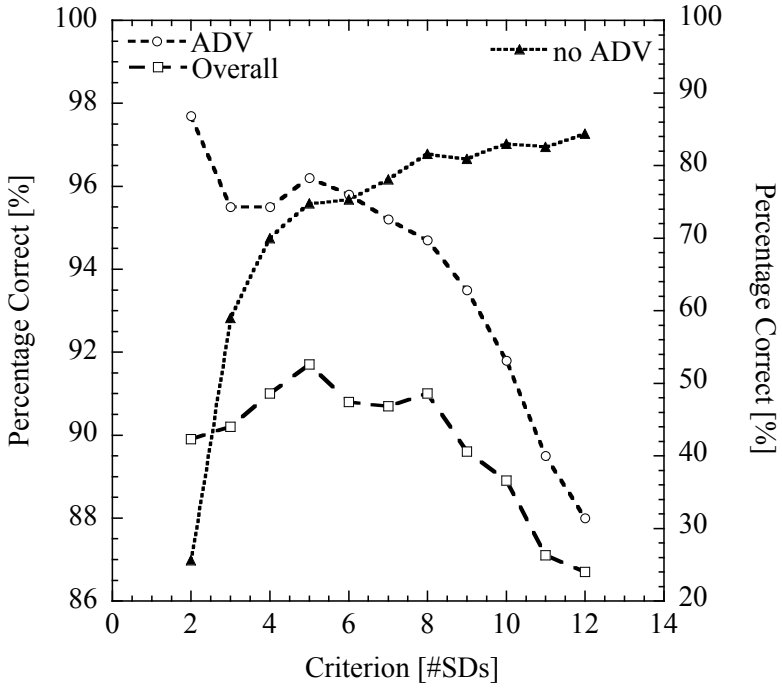

Figure 2.9: Percentage of correct predictions made by a binary logistic regression model for different criteria (number of SDs). Displayed on two different scales are true negatives (no ADV) on the right ordinate and on the left ordinate, true positive as well as an overall accuracy percentage (ADV, Overall). The maximum overall percentage is 91.7% when using a criterion of five SDs above mean, meaning data and model have the best agreement for this criterion.

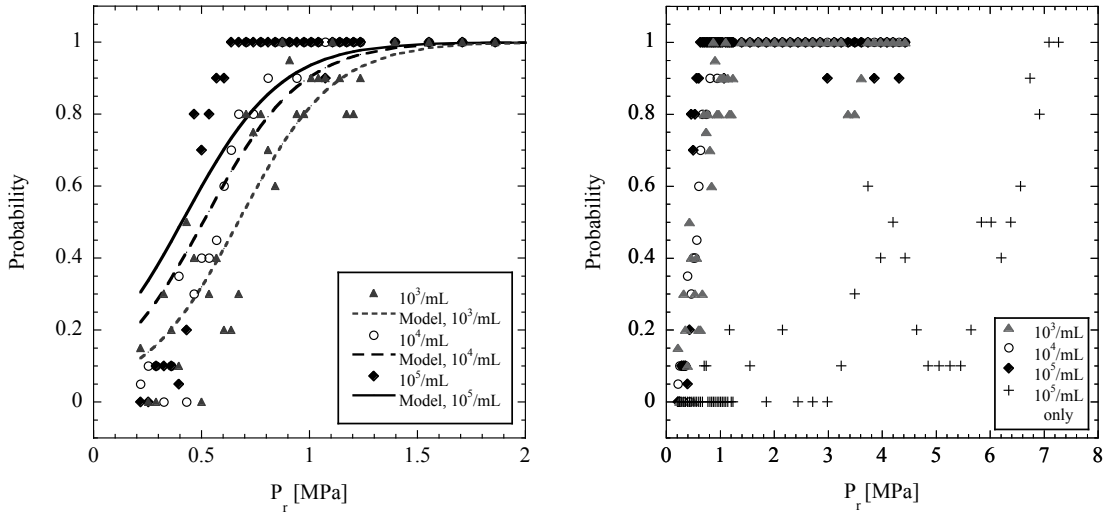

(a) (b)

Figure 2.10: (a) Probability for ADV computed in the presence of 10^3 , 10^4 , and 10^5 microspheres/mL of Definity® according to a criterion of five SD above mean. Data at a given pressure amplitude show the result for N = 10 or 20 measurements. The entire dataset, including results for $P_r > 2$ MPa, is not shown in order to better display the transition of probability from 0 to 1. Curve fits are taken from the regression model described in the text. (b) The entire dataset for the experiments in (a) is displayed here along with data that were collected with only CA present (+), which show a higher threshold than the solutions containing droplets. Data for (+) reflect N = 10 measurements.

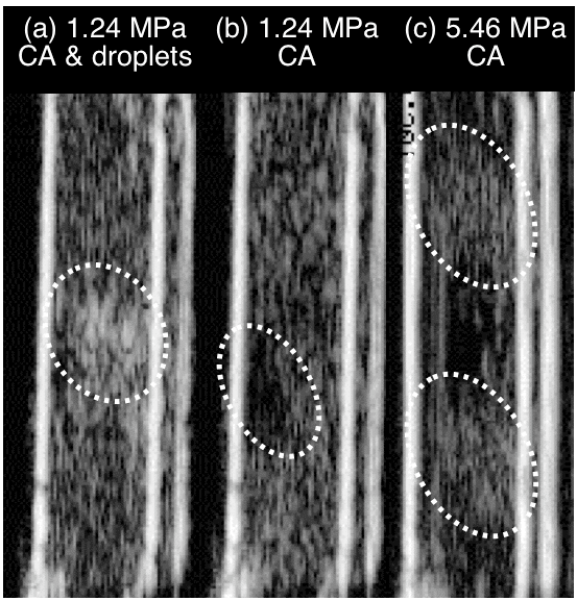

Figure 2.11: Frames immediately following acoustic interference are shown when solutions containing both (a) droplets and CA and (b), (c) CA only are exposed to 20 ms pulses. ADV occurs in (a) at 1.24 MPa as indicated by the circle. At the same pressure, CAs are destroyed as indicated by low echogenicity when droplets are absent (b). Increasing the pressure to 5.46 MPa further causes high echoes in areas surrounding the focal zone, which may be the aggregation of CA microspheres in the side lobes.

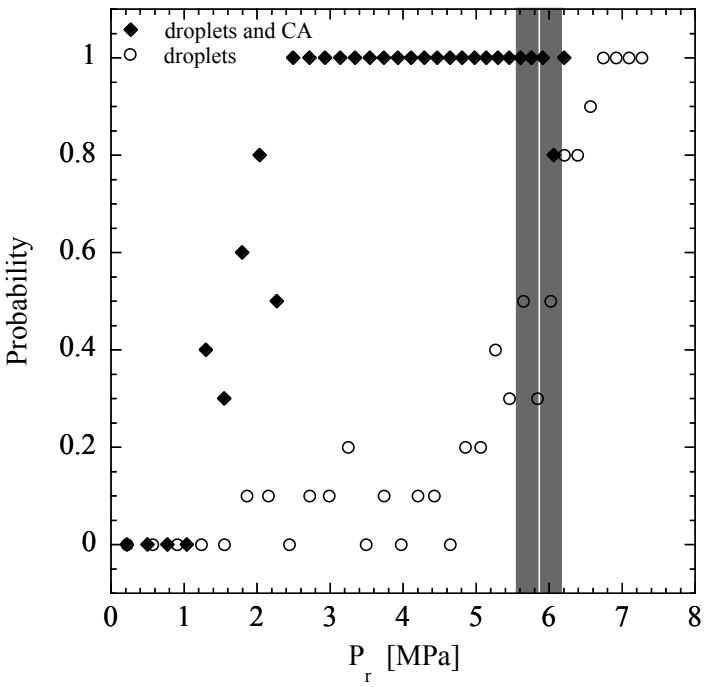

Figure 2.12: Probability results for ADV using 20 μs tone bursts. CA concentration is 10^5 microspheres/mL. Circles and diamonds are data collected from ADV in flow conditions. The white vertical line and the gray region indicate the mean ADV threshold in P_r with no CA present and the associated standard error, respectively, found in the static experiments using detection by B-mode cineloops.

2.4 Discussion

The results show that the ADV threshold can be lowered by both lengthening pulse duration as well as by adding CA. In evaluating these two methods in the following sections, the occurrence and role of IC are also examined.

2.4.1 ADV Threshold with Droplets Only

From the static experiments, it appears that the ADV threshold remains relatively constant (5.5-5.9 MPa) for pulse durations shorter than 1 ms for a 1.44 MHz carrier frequency (Fig. 2.3). The threshold drops for pulse durations longer than 1 ms, whereupon it appears to reach a plateau (3.8-4.6 MPa). Although 20 ms may vaporize droplets at a lower P_r than microsecond pulse durations, it may not be optimal for *in vivo* conditions because of heat deposition on overlying tissue layers. Thus, we investigated if the total on time," or the cumulative duration of all tone bursts, had an effect on the ADV threshold by transmitting 1000 pulses at 20 μs duration each (20 ms on time) at a PRF of 500 Hz (1% duty factor). Fig. 2.3 illustrates that the threshold for this case (mean of 4.25 MPa) is not statistically significant from the threshold found for a 20 ms tone burst (mean of 3.96 MPa).

2.4.2 The Role of Inertial Cavitation in ADV

To investigate the role of inertial cavitation, where broadband noise signifies the occurrence of an event, the acoustic scattering from the exposure of droplets to ultrasound was recorded and compared to the data captured by the imager. The thresholds as determined by the two different detection methods as well as the threshold trends seen in terms of pulse duration (Figs. 2.3, 2.6) agree. A constant threshold for pulse durations less than 1 ms is seen in Figs. 2.3 and 2.6 and is consistent with the literature [13], where the time-averaged cavitation activity in blood remained constant for pulse durations from 20 μs-1 ms at 1 MHz. Both curves

also show that the threshold drops for pulse durations longer than 1 ms. There is no indication in the data presented here nor in the literature that suggest that the threshold would drop further for pulse durations longer than 20 ms [8]. This consistency amongst the data suggests at least that IC plays a role in ADV at frequencies below several MHz, though it is not clear whether the inertial cavitation occurs inside or outside of the droplet in the experiments when only droplets are exposed to ultrasound.

The elevated threshold for broadband noise of 4.5 MPa (MI=3.8) for 20 ms pulses as compared to the results found in the literature [8] may be explained when considering that IC and ADV are linked. With a lower f/number transducer (1 versus an f/number of 2 in [8]), fewer higher harmonics accumulate because of reduced time for high amplitude ultrasound propagation. Since high frequencies are associated with a reduced ADV threshold, it may be more difficult for a low f/number transducer to vaporize droplets. As this difference in threshold is shown in *in vitro* experiments, transducer geometry and the effects of nonlinear propagation must be further investigated for in vivo applications, where tissue provides substantial attenuation. Although the nonlinearity coefficient β is similar for both water and tissue (3.6 and 4-6.2, respectively [14]) the Goldberg number is much higher in water than in tissue [15]. High harmonics generated during propagation through water would be attenuated to some degree if instead the medium were tissue.

2.4.3 IC and "On-time"

The decrease in ADV threshold with increasing pulse duration along with the comparable thresholds of equivalent on-time pulses is reminiscent of the behavior of IC. It was shown that hemolysis, which reflects the quantity of IC, increased with longer pulse duration and total "on-time" [9]. It may take as few as one available nucleus to induce IC [9], and the opportunity for this to occur increases with longer

pulse durations.

Examples of RF waveforms and the associated time-frequency plots are shown in Fig. 2.7. Given adequate time for insonification, the chances of a cavitation nucleus passing through the acoustic beam increases, and with increasing amplitude, the initiation delay for cavitation decreases [16]. At 3.98 MPa, IC occurs only a portion of the time during the 20 ms pulse (Fig. 2.7a). The duration of IC increases with increasing amplitude and is eventually occuring during the entire pulse at (6.21 MPa). This increase in IC duration can also be seen in the multiple 20 μs pulses at 4.85 and 6.21 MPa (Fig. 2.7b). These amplitudes are considered above threshold, where there is a spread in the spectral content indicating broadband noise. Fig. 2.7b also shows RF waveforms at amplitudes below ADV threshold (3.24, 4.20 MPa) that contain an interesting characteristic that is not seen in single 20 ms pulses. For the case at 3.24 MPa, the scattering amplitude increases at approximately two thirds into the duration of the pulse sequence and may appear to reflect the accumulation of sinking scatterers, which was seen in B-mode cineloops. This is consistent with an increase in scattering only at the fundamental frequency of 1.44 MHz. At 4.20 MPa, spikes in the scattering signal occur at two time points and appear to reflect the generation of only a few bubbles per spike. Although there is a slight spread into frequencies lower than the carrier frequency, it was not sufficient to meet threshold criterion for subharmonics. The change in acoustic emissions during insonification is better realized in Fig. 2.7c. Since the imaging array and passive single element transducer could not be used concurrently, there is no direct evidence coupling the aforementioned events though they can be seen during separate experiments at the same amplitude.

2.4.4 Inertial Cavitation External to a Droplet

The possibility that cavitation outside of the DDFP droplet may trigger ADV was investigated by the addition of CA to the solution. CAs such as Albunex® ([12], [17][18][19]) and Levovist® [18] have been shown to lower the IC threshold of the host medium and in the case of Optison™, lower it even further than the broadband emission threshold for PFC droplets [8]. At diagnostic power levels, ultrasound exposure of Definity® has been shown to cause bioeffects thought to be associated with cavitating microbubbles. These bioeffects include an increase in troponin T at MI=1.2 [20] and petechial hemorrhages at an apparent threshold of 0.37 MPa for 1.7 MHz, or MI=0.3 [21]. These thresholds are significantly lower than the cavitation threshold found with droplets present at MI=3.8 for 20 ms pulses. If cavitation is linked to ADV as an initiator of the phenomenon, then there could be a reduction in ADV threshold with the presence of CAs. We see that in Figs. 2.10 and 2.12, there is indeed a reduction in threshold with the introduction of CA. In fact, it is lowered by an order of magnitude for 20 ms pulses for the three CA concentrations investigated here and by a factor of three for 20 μs pulses and 10^5 microspheres/mL of CA. Although IC in the host medium may not always be the trigger for ADV, these results indicate that it can be.

With a higher concentration of CA, there is a higher probability of cavitation occurring with each pulse since there are more nuclei present [22]. As such, 10^5 microspheres/mL provide more nuclei and therefore there is a higher chance of IC, and a higher chance that the event occurs in proximity to a droplet. The initial threshold is considered here as the amplitude where there is at least one event (Fig. 2.10a. Although this threshold is similar for all concentrations of CA, the transition to achieving a probability of 1 rises more quickly with increasing P_r for 10^5 microspheres/mL. The logistic binary regression model showed that the results of all three CA concentrations were statistically significant relative to each other

($p<0.01$), with the probability of an occurrence of an ADV event increasing with the concentration of CA Fig. 2.10a. A similar result was seen with Levovist® and Albunex® CAs, each of which had an IC threshold (detected by H_2O_2 production) of 0.41 MPa independent of the concentration of CA added [18]. There was no statistical difference in the amount of cavitation activity when comparing activity increase from various dilutions of one or the other CA that were added to denucleated phosphate buffered solution. However, when Albunex® was added to a solution with higher gas content, a notable rise in cavitation activity resulted. The solutions in the experiments described in this paper were not degassed, and perhaps the combination of higher gas content, droplets, and Definity® provided substantially more nuclei to show a significant difference between the three CA concentrations.

While the results of the CA studies in this section have been discussed in comparison to thresholds of other types of CA, they do not reflect the effects of all types of CA. It has been shown that CA oscillations differ with the type of stabilizing shell [23][24], and we can reason from bubble dynamics that the type of gas will also affect the contrast agent behavior. However, it has also been shown in [21] that the bioeffects (petechial hemorrhages) resulting from IC occur at the same pressure amplitude for Optison™, Definity®, and Imagent®, and that the degree of bioeffects depends on the number of microbubbles and is independent of the type of CA. Since our passive detection method was used to identify the occurrence of IC and the thresholds for IC and ADV were similar, the effect of CA on the ADV threshold may be the same regardless of the type of CA.

2.4.5 ADV Threshold *In Vivo*

It is noted here that the findings of these studies may not represent droplet behavior in blood. It has been shown *in vitro* that the ADV threshold increases when blood is the host medium [5], although further investigation is required to determine

the effects of blood flow in vivo. Additionally, the solutions in these experiments were not degassed and were expected to be either at equilibrium with air as they were circulated in the flow system, or slightly supersaturated in the static system, where gas dissolved into the solution during refrigeration before being placed into the 37°C water bath. However, there did not appear to be a significant difference in ADV threshold between the two systems (Fig. 2.12). However, human arterial blood has a P_{N_2} of 571 mmHg, P_{O_2} of 102 mmHg and a P_{CO_2} of 40 mmHg [25]. Arterial blood, which is the target location for embolotherapy for cancer treatment, would therefore have a slightly different gas content than that found in these experiments. Still, with the addition of CA and consequently an even lower IC threshold, the ADV threshold is likely to be also reduced in blood.

Additionally, for successful therapy in vivo, the bubbles resulting from ADV must expand to an appropriate volume to be able to occlude arterial feeder vessels to the cancer. While there has been success in a lepus kidney model [6] as mentioned previously, verification of sufficient bubble sizes is necessary for applicability in humans.

2.5 Conclusions

In order to achieve ADV at a low ultrasonic frequency and reduced input energy, ADV threshold was measured as a function of pulse duration for single tone bursts and for multiple pulses fired at a given PRF. By increasing pulse duration at 1.44 MHz, both the ADV and IC thresholds decreased in a similar trend. It was also found that repetitive pulsing could induce the same effect at similar amplitudes as a single pulse if the two have equivalent on-times. This may suggest a link between the two phenomena, though proof of a causal relationship and determination of whether IC occurs inside or outside of the droplet remains for future investigation.

In testing for the influence of IC on ADV, further experiments were conducted to

evaluate the role of IC external to a droplet by the addition of CAs. The presence of CAs greatly reduced the ADV threshold by an order of magnitude for 20 ms pulses and by a factor of three for 20 μs pulses. Perhaps, with the use of CAs and by choice of an appropriate pulse duration that reduces ADV threshold while minimizing input power, routine ADV can be feasible at a range of useful locations in the body.

REFERENCES

[1] T. Boehm, J. Folkman, T. Browder, and M. S. OReilly, "Antiangiogenic therapy of experimental cancer does not induce acquired drug resistance," *Nature*, vol. 390, pp. 404–407, 1997.

[2] R. E. Apfel, "U.S. patent 5 840 276: Activatable infusable dispersions containing drops of a superheated liquid for methods of therapy and diagnosis," 1998.

[3] J. G. Riess and M. P. Krafft, "Fluorocarbons and fluorosurfactants for *in vivo* oxygen transport (blood substitutes), imaging, and drug delivery," *Mater Res Soc*, vol. 24, pp. 42–48, 1999.

[4] J. M. Correas and S. D. Quay, "Echogen^{TM} emulsion: A new ultrasound contrast agent based on phase shift colloids," *Clin Radiol*, vol. 51, pp. 11–14, 1996.

[5] O. D. Kripfgans, J. B. Fowlkes, D. L. Miller, O. P. Eldevik, and P. L. Carson, "Acoustic droplet vaporization for therapeutic and diagnostic applications," *Ultrasound Med Biol*, vol. 26, no. 7, pp. 1177–1189, 2000.

[6] O. D. Kripfgans, C. M. Orifici, P. L. Carson, K. A. Ives, O. P. Eldevik, and J. B. Fowlkes, "Acoustic droplet vaporization for temporal and spatial control of tissue occlusion: A kidney study," *IEEE Trans Ultrason Ferroelect Freq Control*, vol. 752, pp. 1101–1110, 2005.

[7] O. D. Kripfgans, J. B. Fowlkes, M. Woydt, O. P. Eldevik, and P. L. Carson, "*In vivo* droplet vaporization for occlusion therapy and phase aberration correction," *IEEE Trans Ultrason Ferroelect Freq Control*, vol. 49, no. 6, pp. 726–738, 2002.

[8] T. Giesecke and K. Hynynen, "Ultrasound-mediated cavitation thresholds of liquid perfluorocarbon droplets *in vitro*," *Ultrasound Med Biol*, vol. 29, no. 9, pp. 1359–1365, 2003.

[9] D. L. Miller and A. R. Williams, "Nucleation and evolution of ultrasonic cavitation in a rotating exposure chamber," *J Ultrasound Med*, vol. 811, pp. 407–412, 1992.

[10] J. E. Parsons, C. A. Cain, and J. B. Fowlkes, "Cost-effective assembly of a basic fiber-optic hydrophone for measurement of high-amplitude therapeutic ultrasound fields," *J Acoustic Soc Amer*, vol. 119, pp. 1432–1440, 2006.

[11] P. A. Dayton, K. E. Morgan, A. L. S. Klibanov, G. Brandenburger, K. R. Nightingale, and K. W. Ferrara, "A preliminary evaluation of the effects of primary and secondary radiation forces on acoustic contrast agents," *IEEE Trans Ultrason Ferroelect Freq Control*, vol. 644, pp. 1264–1277, 1997.

[12] W. S. Chen, A. A. Brayman, T. Matula, and L. A. Crum, "Inertial cavitation dose and hemolysis produced in vitro with or without optison®," *Ultrasound Med Biol*, vol. 529, pp. 725–737, 2003.

[13] E. C. Everbach, I. R. S. Makin, M. Azadniv, and R. S. Meltzer, "Correlation of ultrasound-induced hemolysis with cavitation detector output in vitro," *Ultrasound Med Biol*, vol. 423, pp. 619–624, 1997.

[14] F. A. Duck, *Physical Properties of Tissue: A Comprehensive Reference Book*. London Academic Press, 1990.

[15] T. L. Szabo, F. Clougherty, and C. Grossman, "Effects of nonlinearity on the estimation of in situ values of acoustic output parameters," *J Ultrasound Med*, vol. 118, pp. 33–41, 1999.

[16] Z. Xu, J. B. Fowlkes, E. D. Rothman, A. M. Levin, and C. C. Cain, "Controlled ultrasound tissue erosion: the role of dynamic interaction between insonation and microbubble activity," *J Acoust Soc Am*, vol. 117, no. 1, pp. 424–435, 2005.

[17] C. K. Holland and R. E. Apfel, "Thresholds for transient cavitation produced by pulsed ultrasound in a controlled nuclei environment," *J Acoust Soc Am*, vol. 88, no. 5, pp. 2059–2069, 1990.

[18] D. L. Miller and R. M. Thomas, "Ultrasound contrast agents nucleate inertial cavitation *in-vitro*," *Ultrasound Med Biol*, vol. 821, pp. 1059–1065, 1995.

[19] P. P. Chang, W. S. Chen, P. D. Mourad, S. L. Poliachik, and L. A. Crum, "Thresholds for inertial cavitation in albunex suspensions under pulsed ultrasound conditions," *IEEE Trans Ultrason Ferroelect Freq Control*, vol. 148, pp. 161–170, 2001.

[20] S. Y. Chen, M. H. Kroll, R. V. Shohet, P. Frenkel, S. A. Mayer, and P. A. Grayburn, "Bioeffects of myocardial contrast microbubble destruction by echocardiography," *Echocardiography-A Journal of Cardiovascular Ultrasound and Allied Techniques*, vol. 619, pp. 495–500, 2002.

[21] P. Li, W. F. Armstrong, and D. L. Miller, "Impact of myocardial contrast echocardiograph on vascular permeability: Comparison of three different contrast agents," *Ultrasound Med Biol*, vol. 30, pp. 83–91, 2004.

[22] G. Iernetti, "Cavitation threshold dependence on volume," *Acustica*, vol. 24, pp. 191–196, 1971.

[23] N. de Jong, L. Hoff, T. Skotland, and N. Bom, "Absorption and scatter of encapsulated gas filled microspheres: Theoretical considerations and some measurements," *Ultrasonics*, vol. 30, pp. 95–103, 1992.

[24] C. C. Church, "The effects of an elastic solid-surface layer on the radial pulsations of gas bubbles," *J Acoust Soc Amer*, vol. 97, pp. 1510–1521, 1995.

[25] R. M. Berne and M. N. Levy, *Physiology*. Mosby-Year Book, 3rd ed., 1993.

CHAPTER III

Consideration of Attenuation and Efficiency in Acoustic Droplet Vaporization for Embolotherapy

3.1 Introduction

The acoustic droplet vaporization (ADV) threshold is dependent on independent variables such as frequency and pulse duration as discussed in the Chapter II. One of the tradeoffs that arises from choosing a high versus low frequency, or short versus long pulse duration is acoustic power. At high frequencies, less acoustic power is required to achieve ADV [1] but considerably more may be needed when attenuation is present. Smaller amplitudes are required to vaporize with long pulses than with short pulses [2]; on the other hand, long pulse durations lead to increased time average power and consequently increased risk of heating.

The addition of ultrasound contrast agent (CA) alleviates many of the decisions that must be made to weigh these tradeoffs because the inertial collapse of CA microbubbles appears to trigger the vaporization of a neighboring droplet [2]. For lower frequencies, CAs have a low inertial cavitation (IC) threshold and can collapse at pressures that are lower than thresholds for ADV. Thus, a significant reduction in pressure amplitude is required to achieve ADV under these conditions if the inertial collapse of CA is a trigger.

Having the ability to lower the ADV threshold with the addition of CA or with lengthening pulse duration, we must now consider the effects of overlying

tissue when attempting to vaporize droplets transcutaneously. Because the current demonstrational target of embolotherapy by ADV is renal cell carcinoma (RCC), we consider the acoustic access to the kidney. Three options are viable: through the (1) abdomen, (2) intercostal space, or (3) retroperitoneum. The intercostal space limits the effective aperture size of the transducer as sound will not easily penetrate through bone; additionally, ultrasound (US) must first propagate through the renal parenchyma, where acoustic shadowing by bubbles could effectively block further distal ADV [3]. If the target is to vaporize droplets in the cortex, intercostal penetration may be a reasonable option. Acoustic access through the abdomen or retroperitoneum is more ideal for targeting the renal or a segmental artery; of these two options, retroperitoneal access must penetrate through a larger portion of renal parenchyma before reaching the arterial supply, and the position of the rib cage and spine may confine positional adjustments necessary for anatomical variability. Abdominal access also penetrates through some parenchyma and must contend with the proximity of the bowel. Patient orientation and gravity can be used to reduce possible interference from gas in the bowel.

Thus, *in vivo* studies will concentrate on acoustic access through the abdominal wall, which is composed of layers of skin, fat, and muscle. On average, the human abdominal wall as a whole has been found to be 2.4 ± 0.6 cm thick with a mean attenuation of 1.13 dB MHz^{-1} cm^{-1} [4]. The set of experiments presented in this chapter assess the success of ADV in an *in vitro* environment that simulates abdominal transcutaneous ADV. In a simplified representation, overlying tissue layers are simulated by using a 6 cm thick tissue-mimicking (TM) phantom equivalent to 3 dB attenuation at 1 MHz, or approximately 3 cm human abdominal wall. Under these conditions, ADV thresholds are measured with and without the presence of CAs. The efficiency of the process is also measured with varying droplet concentrations and pulse repetition frequencies (PRFs).

3.2 Materials and Methods

3.2.1 Perfluorocarbon Droplets and Contrast Agents

Liquid perfluorocarbon droplets with albumin shells were manufactured according to Kripfgans et al. [1]. Bovine albumin (A3803, Sigma-Aldrich, St. Louis, MO) was first combined with saline at a concentration of 4 mg/mL. The albumin-saline solution (750 μL) and dodecafluoropentane (250 μL) (09-6182, Strem Chemicals, Inc., Newbury Port, MA) were then amalgamated (Wig-L-Bug, Crescent Dental Mfg. Co., Lyons, IL) to form droplet emulsions. Immediately before performing experiments, 1 mL stock droplet solution was diluted in 10 mL saline and filtered with syringe filters (Whatman, Maidstone, UK) that were connected in series and ordered in decreasing pore size (20, 16, 8, and 5 μm; Whatman, Maidstone, UK). Based on previous measurements using a hemacytometer and imaged under microscopy [5], a droplet concentration of 2.85 x 10^6 droplets/mL resulted from this process and was designated as the standard concentration in this study. Other concentrations, which are diluted after droplet filtration, are described in reference to this standard value, such as a half, a quarter, and a tenth.

Definity® (Bristol-Myers Squibb Medical Imaging, North Billerica, MA) ultrasound CA, which consists of lipid shelled octafluoropropane gas microspheres, was used in this study. Based on the appropriate dilution of the reported stock concentration on the label, a concentration of 10^5 microspheres/mL in saline was used for these experiments. Definity® was activated 1-14 days prior to the experiment, and gently agitated to a milky white color immediately before the experiments. PFC gas replaced the headspace in the vial after CA was drawn from it. Four different formulations were used in these experiments: droplets only, droplets and CA, CA only, and saline only.

3.2.2 Experimental Setup

The setup used in this study was similar to the flow environment setup described in [2] and Chapter II. A 1 MHz annular array (10 cm aperture, 9 cm focus, 16 concentric rings; Imasonic, Besançon, France) was focused in the center of a flow tube, where a segment of thin-walled dialysis tubing provided acoustic access (5 mm diameter, Spectra/Por®, Spectrum Laboratories Inc., Laguna Hills, CA). All elements were driven in phase for these experiments. Droplets and/or CA were continuously stirred in a reservoir and circulated with a peristaltic pump (Masterflex® pump and speed controller, Cole-Parmer, Chicago, IL) through the flow tube and acoustic window, where they were exposed to ultrasound. The maximum flow speeds were nominally 8 and 16 cm/s, and an in-line bubble trap served as a capacitor to ostensibly maintain constant flow and remove large bubbles from circulation.

For simulation of overlying tissue, a tissue-mimicking (TM) phantom consisting of two layers of 16 x 16 cm^2 Zerdine® slabs (1540 m/s sound speed, 0.5 dB MHz^{-1} cm^{-1} attenuation, CIRS, Inc., Norfolk, VA), one 2 cm thick and the other 4 cm thick, was positioned between the annular array and the flow tube. A frame to hold the phantom was put in place prior to any measurements for simple insertion of the Zerdine® slabs between measurements. Because Zerdine® is hydrophilic and any uptake of water would alter its acoustic properties, the slabs were contained in a re-sealable plastic bag with castor oil (CA208, Spectrum Chemical Manufacturing Corp., Gardena, CA) ($c = 1.477$ mm/μs, $\rho = 0.969$ g/cm^3 (Onda Corp., Sunnyvale, CA)) for coupling. Excess air was suctioned from the bag. As will be described later, the total insertion loss was measured. The entire setup was situated in degassed and deionized water that was heated and maintained at approximately 37°C (Ex 7, ThermoNESLAB, Newington, NH).

A 5 MHz phased array (FPA 5 MHz, System Five, General Electric Vingmed, Milwaukee, WI) inserted into the center hole of the annular array was used to

align the focus of the annular array with the target. For alignment purposes, high amplitude pulses were transmitted from the annular array to induce IC in degassed deionized water and consequently bubble clouds at the focus. These clouds were visible in the B-mode images from the 5 MHz phased array, and their location was noted for alignment with the flow tube.

The ADV threshold was determined by transmitting successive US exposures with increasing applied pressure amplitudes in a step-wise fashion, starting at ambient pressure and ending at pressures beyond the ADV threshold. Each US exposure at each pressure amplitude consisted of 10-cycle pulses that were transmitted at a specified pulse repetition frequency (PRF) for approximately five seconds. A 10 MHz linear array (FLA 10 MHz, System Five, General Electric Vingmed, Milwaukee, WI) was positioned 90° from the annular array and on the distal side of the TM phantom to image any bubbles resulting from ADV. The 10 MHz linear array was used for ADV detection rather than the 5 MHz phased array for two reasons: (1) it provided superior images and (2) its placement allowed imaging to remain uncompromised by additional attenuation introduced by the TM phantom. However, because the 10 MHz imager itself is capable of vaporizing droplets, the power output of the imager was minimized by setting the mechanical index (MI) to 0.3. The B-mode images were then transferred via video output to a desktop computer, where frame grabbing software (NIH Image Version 1.61, U.S. National Institutes of Health, Bethesda, MD) captured the images at a 20 Hz frame rate and recorded them in TIFF format. This image transfer was ideal for efficient data storage due to the larger memory capacity of the desktop computer. The B-mode TIFF movies were then analyzed to determine the ADV threshold.

Table 3.1 summarizes the acoustic parameters for each formulation tested. For formulations containing CA, a slower flow rate was used for better detection of the resulting bubbles and because it has been shown to be successful in the past

Table 3.1: Summary of Experimental Parameters

Agents	**Attenuation**	**Velocity [cm/s]**	**PRF [Hz]**	**N**
Droplets	no	8	100	5
			10-500	1
			500	4
	yes	16	100	5
Droplets + CA	no	8	10	7
	yes	8	10	7
		16	20	5
CA only	yes	16	20	5
		8	10	5
Saline only	no	16	20	1
	yes	16	20	1

Threshold experiments were conducted for the acoustic parameters for the specified agent(s) listed, where velocity refers to flow velocity, PRF refers to pulse repetition frequency, and N refers to the number of repetitions. Two Zerdine® slabs totaling 6 cm in thickness were used to provide attenuation.

for measuring ADV thresholds; however, in order to make a comparison to the formulations containing only droplets, the flow velocity also was matched at 16 cm/s and the PRF was increased proportionally. The implications of the range of PRFs used is discussed subsequently in the Results and Discussion sections. Although the presented results were attained using the 10 MHz linear array, a limited number of experiments were performed using the 5 MHz phased array to detect bubbles produced by ADV from a different imaging plane.

3.2.3 Transducer Calibration

The 1 MHz annular array was calibrated with an in-house fiber optic probe hydrophone (FOPH) [6] in de-ionized and 80% degassed water. The output pressures resulting from a 10-cycle excitation pulse and a range of applied voltages were measured at the spatial maximum. After a free water calibration, where the spatial maximum was located and named Position 1, the setup for *in vitro* experiments was reproduced by inserting the Zerdine® slabs immersed in castor oil, along with its

holder between the annular array and the hydrophone. The derated pressures were measured again at Position 1 with the attenuating layers in place. With greater nonlinear absorption, the location of the spatial maximum in fact changes with the presence of the TM phantom. The shifted spatial maximum was then located (Position 2), and the resulting pressures were measured again for a range of applied voltages. During *in vitro* experiments, the flow tube was always aligned with the spatial maximum in the acoustic field.

A theoretical fit derived from the Khokhlov-Zabolotskaya-Kuznetsov (KZK) equations was used to characterize the transducer response in peak rarefactional pressure (P_r) to the range of applied voltages. The true attenuation provided by the TM phantom was also characterized since the addition of the castor oil, re-sealable plastic bag, and discontinuity between the slabs are causes of additional absorption and/or scattering. These results are provided below.

3.2.4 Image Analysis

The TIFF images recorded by the frame grabber were converted to the appropriate linear grayscale before threshold analysis. Because the grayscale of the images saved in TIFF format was different from that used by the System Five diagnostic scanner (echoPAC format), the appropriate conversion was needed to recover the original image which is quantified in terms of the relative echo amplitude.

A calibration was performed in order to determine the correct grayscale conversion from TIFF to echoPAC format. Several images of the same Zerdine® slabs used in the experiments were captured and saved in both echoPAC and TIFF format. Gain, time gain compensation, and focal depth were varied for each image. The combination of attenuating medium and variation in imaging parameters allowed for testing of the full dynamic range and any change in conversion with imaging parameters. The echoPAC pixel intensities were extracted using proprietary software

(General Electric, Milwaukee, WI) operating in Matlab (The MathWorks, Inc., Natick, MA) and were then decompressed according to the algorithm provided by the manufacturer. The pixel values between the TIFF images and the decompressed echoPAC images were compared and a quadratic function was fit to the conversion curve. This grayscale conversion was applied to all images.

3.3 Results

3.3.1 Sound Field through Zerdine®

Fig. 3.1a shows results of four acoustic field calibrations performed in degassed deionized water and measured with an FOPH. A theoretical curve for achievable P_r was generated using time-domain methods to solve the KZK equation [7], where the annular array was modeled as a single element transducer. Attainable pressures were simulated from a range of source pressures, and assuming a linear relationship between source pressures and applied voltages, a fit was produced.

The attenuation effects from the TM phantom can be seen in Fig. 3.1b, where the derated pressures (Position 2) as measured by the FOPH is plotted as a function of the expected pressure in a water path. Otherwise stated, for an applied voltage, the maximum pressure attained in a water path and the maximum pressure attained through the TM phantom is shown. The slope of the fit in Fig. 3.1b is 0.7 and corresponds to -3.1 dB in pressure, indicating that there was no significant contribution from the layer of castor oil, bag, or gap between Zerdine® layers. Additionally, a calibration confirmed that the same pressures were achieved with and without the phantom holder.

With the insertion of Zerdine®, there is a slight shift in the spatial maximum in the proximal direction by approximately 1.5 mm (Fig. 3.2). In order to understand the effects of the TM phantom, the spectral composition of two waveforms with the same P_r, one traveling through water and one traveling through the phantom, were

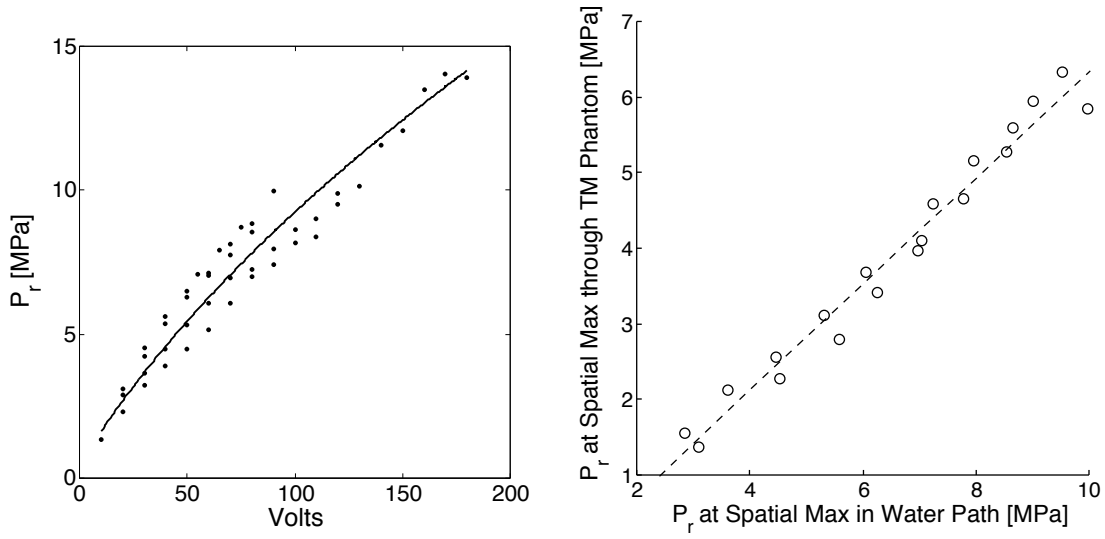

(a) (b)

Figure 3.1: a) Data from four different free water calibrations, where pressure was measured with a fiber optic probe hydrophone. The data was fit with a simulated curve derived from the KZK equation. b) For a given pressure attained in a water path, the corresponding *in situ* pressure from the same acoustic source achieved through an attenuating gel is plotted.

examined. The Fourier transforms of the waveforms are compared in Fig. 3.3, where it appears that the amplitudes at the fundamental frequency and harmonics are nominally equivalent with the exception of the third harmonic at 3 MHz.

3.3.2 Threshold Analysis

After grayscale conversion and decompression, the B-mode images captured by the 10 MHz linear array were analyzed to detect the creation of bubbles according to procedures described in [1] and Chapter II. A region of interest (ROI) in the B-mode images was chosen downstream of the focus to capture persisting bubbles. The mean echo amplitude (MEA) was then computed by averaging the pixel values within the ROI for each frame, and subsequently over all 100 frames in a given movie. This calculation was performed for each movie, where each movie captured US exposures at different pressure amplitudes. Thus, an MEA was calculated for each P_r tested

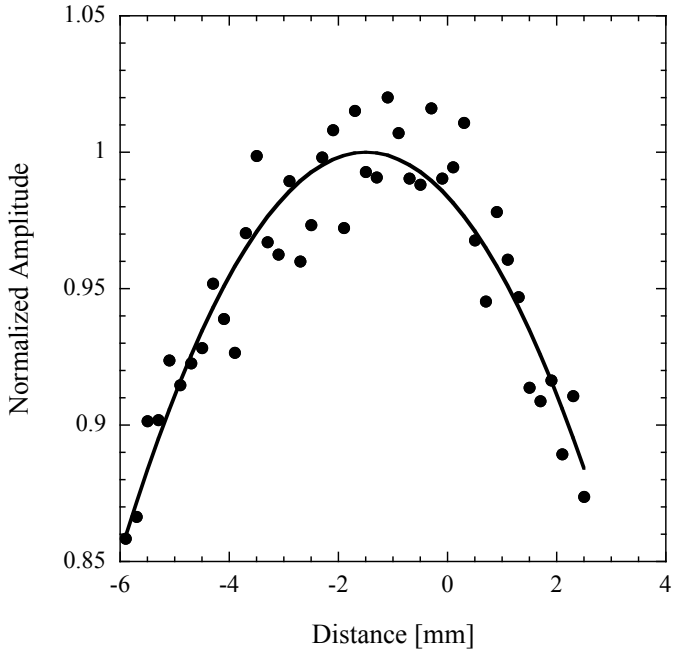

Figure 3.2: Axial beam profile with Zerdine® insertion. Each data point indicates the P_r at each location normalized to the maximum value of the second degree polynomial fit (line). Position 1, or the spatial maximum in a water path, is located at 0 mm. When the majority of the water path was replaced with an attenuating medium, the spatial maximum shifted approximately 1.5 mm (Position 2) toward the transducer. The amplitude at Position 2 was only 2% greater than that at Position 1 when the two locations were measured in the presence of Zerdine®. This ratio, however, increases with amplitude.

in a given experiment. The baseline MEA, i.e. the MEA during no US exposure, was subtracted from all MEAs within an experiment to obtain the relative echo amplitude (REA).

The pressure amplitudes along with their associated REAs were then plotted and analyzed to detect the ADV threshold. Fig. 3.4 shows examples of REA vs. P_r curves for droplets only and for droplets with CA. When only droplets were present, a sharp rise in REA indicated the ADV threshold and was preceded by a slight linear decrease in the sub-threshold REA, the reasons for which will be discussed shortly.

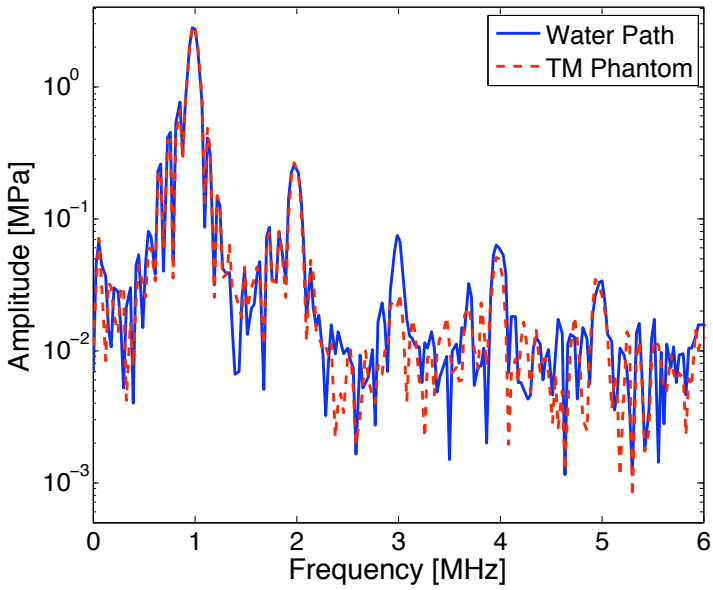

Figure 3.3: The Fourier transforms of two waveforms with an *in situ* P_r of 5.4 MPa. One waveform was measured in a water path, and the other through a Zerdine® TM phantom.

Thus, the curve could be defined by two line segments (Eq. 3.1) [1],

$$REA(p) = (a_1 \cdot (p - p_{theshold} + b) \cdot w_1 + (a_2 \cdot (p - p_{theshold} + b) \cdot w_2 \tag{3.1}$$

where p is P_r, and a_n and w_n are the slopes and windowing functions for each line segment, respectively. An example of an REA vs. P_r curve with its associated curve fit is shown in Fig. 3.4a. This threshold detection technique was also applied to curves associated with experiments with only saline. In this case, a rise in REA was due to bubbles generated by IC.

With the presence of CAs, the REA vs. P_r curve takes a different shape. Contrast disruption occurs at low amplitudes in comparison to ADV, manifesting as a loss in echogenicity. The loss also results in a decrease in REA, which is illustrated in Fig. 3.4b. Although the REA also decreases when only droplets are present (Fig. 3.4a), the decrease appears linear and unlike the rapidly diminishing curve for droplets and CA. The decrease in REA in this case is most likely due to the loss of droplets as

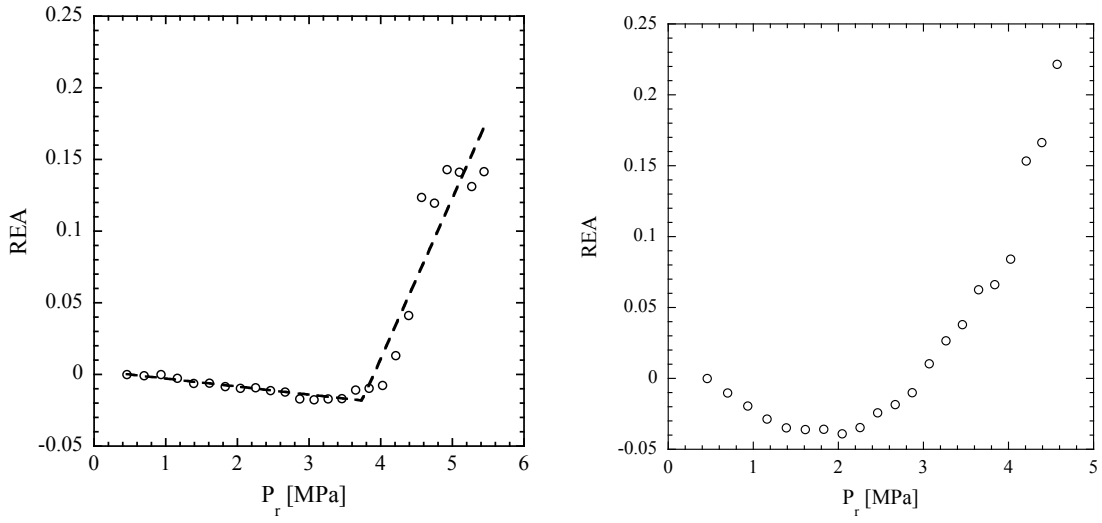

Figure 3.4: REA vs. P_r curve for formulations of (a) droplets, where the associated curve fit is also plotted, (100 Hz PRF) and (b) droplets with CA (10 Hz PRF). Both experiments were conducted in the absence of a TM phantom.

the solution is circulated.

Fig. 3.5 plots a normalized REA, REA/|REA_{min}|, to compare the functional dependence between the case of droplets with CA and CA only. With different imaging parameters such as gain, focal depth, and experimental variation in dilution, the absolute loss in REA may change from experiment to experiment. The point at which the two REA/|REA_{min}| curves deviate suggests new bubble production. Because REA/|REA_{min}| for only CA exponentially decays and does not rise with increasing pressures within the range of P_r tested, the possibility that the bubble production is due to coalesced or aggregated CA, or even from IC, can be excluded. This rise in REA/|REA_{min}| is most likely due to ADV.

Therefore, the ADV threshold in the presence of CAs was determined as the P_r at which the REA/|REA_{min}| began to deviate from the REA/|REA_{min}| curve for only CA. This point was consistently the point at which REA/|REA_{min}| began to increase. In order to find the shift from negative to positive slope, a second degree polynomial was fit to the REA/|REA_{min}| vs. P_r curve, and the minimum value

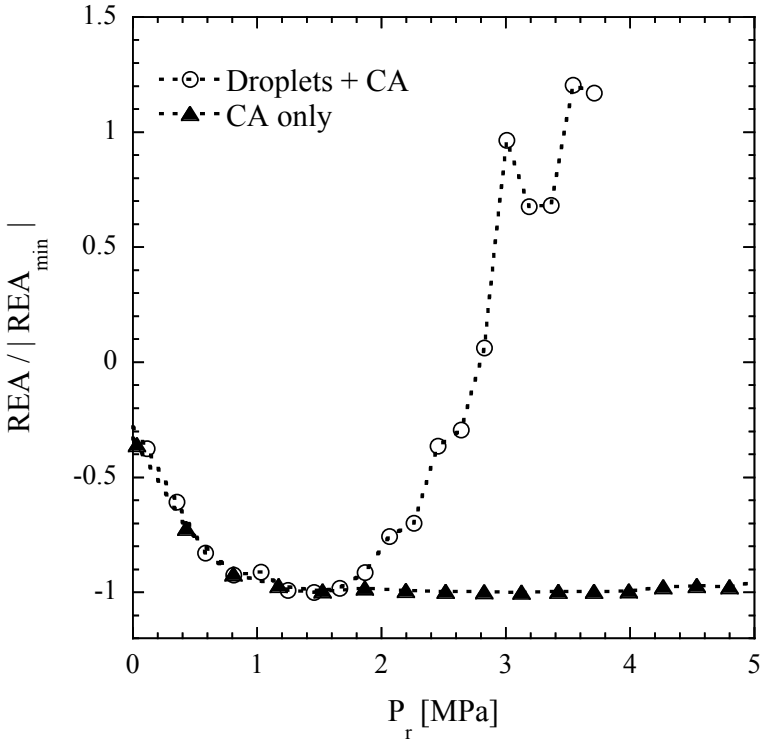

Figure 3.5: Example of REA/|REA_{min}| vs P_r curve for when droplets are mixed with CA and for CA only. Both experiments were conducted in the presence of a TM phantom. As such, P_r values are *in situ*.

signified the ADV threshold.

The threshold results in terms of *in situ* pressures and applied voltage to the transducer are summarized in Fig. 3.6. Using a t test for unequal variances, the difference when comparing the results for ADV with and without attenuation when only droplets were present were statistically significant ($p<0.01$). The thresholds for formulations with CA were much lower ($p<0.001$) such that approximately the same amount of source power was necessary to achieve ADV through an attenuating tissue mimicking (TM) phantom as it was without attenuation and with only droplets. The threshold when droplets and CA were circulated at a flow velocity at 8 cm/s was slightly reduced when the TM phantom was inserted ($p<0.04$). With a flow velocity of 16 cm/s and with attenuation, the threshold when compared to the slower velocity

at 8 cm/s with attenuation was different ($p<.01$) but was statistically the same as the 8 cm/s case without the TM phantom.

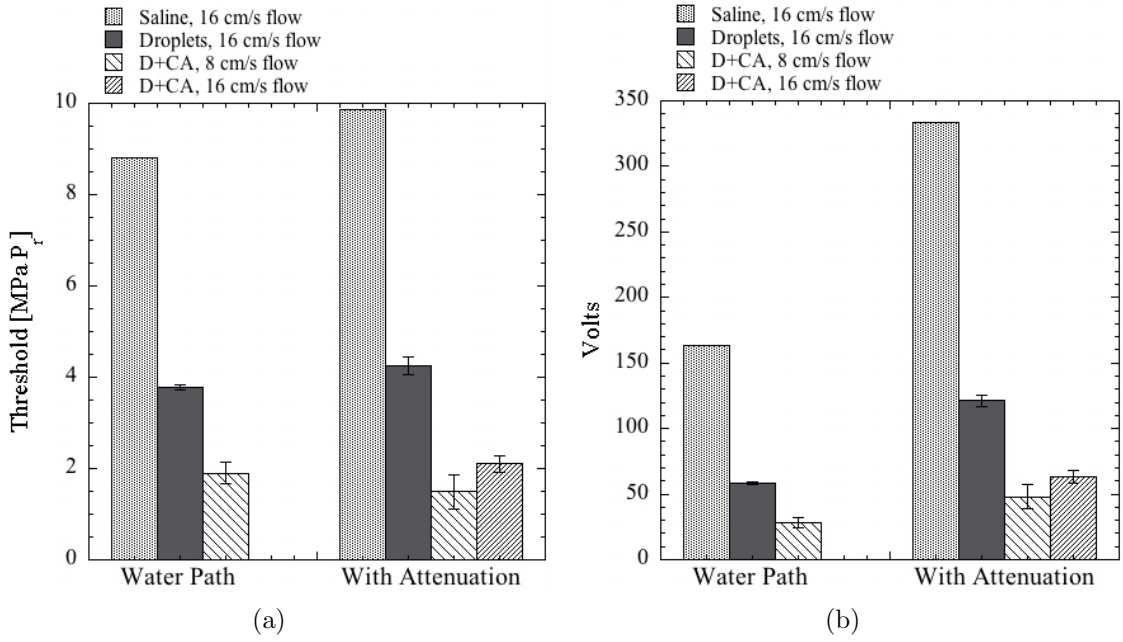

Figure 3.6: Summary of threshold results. Results in terms of *in situ* P_r and voltage applied to the transducer are in (a) and (b), respectively. The IC threshold was measured with only saline, and in all other measurements, the ADV threshold was measured. For the cases when there were droplets and CA (D+CA) or only saline, the PRF was 20 Hz for a 16 cm/s flow rate; when only droplets were present, the PRF was 100 Hz. For an 8 cm/s flow rate, a 10 Hz PRF was used. Error bars indicate standard deviation.

In order to confirm that the presence of the phantom holder did not affect the measurements, a limited number of experiments with only droplets were conducted without the phantom holder. The thresholds measured under these conditions were not statistically different from the thresholds measured with the phantom holder.

3.3.3 Image Analysis for Efficiency

ADV efficiency was explored with varying PRFs and droplet concentrations. In order to evaluate efficiency, B-mode movies were compared within a given setup, where equivalent imaging planes were captured. Small variations in alignment,

although insufficient to affect the detection of the ADV threshold, can capture different parts of the parabolic flow profile within the tube and may affect an accurate comparison of droplet conversion. Therefore, B-mode movies from different setups were not used in the same analysis. Four lines of pixels (similar to four partial M-mode lines) positioned in the flow tube were taken from each image, namely upstream of the focus and at the focus, as well as two cross-sections downstream of the focus (Fig. 3.7). The decompressed pixel intensities were integrated across these lines and were then averaged over the 100 frames in the movie. The integrated lines upstream of the focus, at the focus, just downstream of the focus ("Downstream"), and further downstream of the focus ("Downstream 2") will henceforth be referred to as IM_{up}, IM_{f}, IM_{d1}, and IM_{d2}, respectively. IM_{f}, IM_{d1}, and IM_{d2} were normalized to IM_{up} in order to compute an efficiency factor associated with each of the three positions. Any differences in IM_x for different depths due to focusing effects of the imager were corrected by simple multiplication based on baseline measurements taken without the application of the ADV field. Here, efficiency factor is only a relative metric, and does not describe the efficiency of droplet conversion in terms of an absolute value. Previous measurements have shown that at a higher frequency of 4 MHz, approximately 26% of droplets are converted to gas bubbles with each pulse [8]. It has not yet been determined whether this conversion efficiency holds for different frequencies.

The efficiency factor is plotted in Fig. 3.8 for 100 and 500 Hz PRFs and different droplet concentrations. The efficiency factor for both PRFs remains relatively constant for the two downstream values, but at the focus, the efficiency factor (IM_{f}/IM_{up}) decreases with increasing concentration. IM_{f}, however, is the same regardless of the droplet concentration; generally speaking, absent of any ADV, IM_x increases with increasing droplet concentration. Consequently, the ratio between IM_{f} and IM_{up} decreases with increasing droplet concentration.

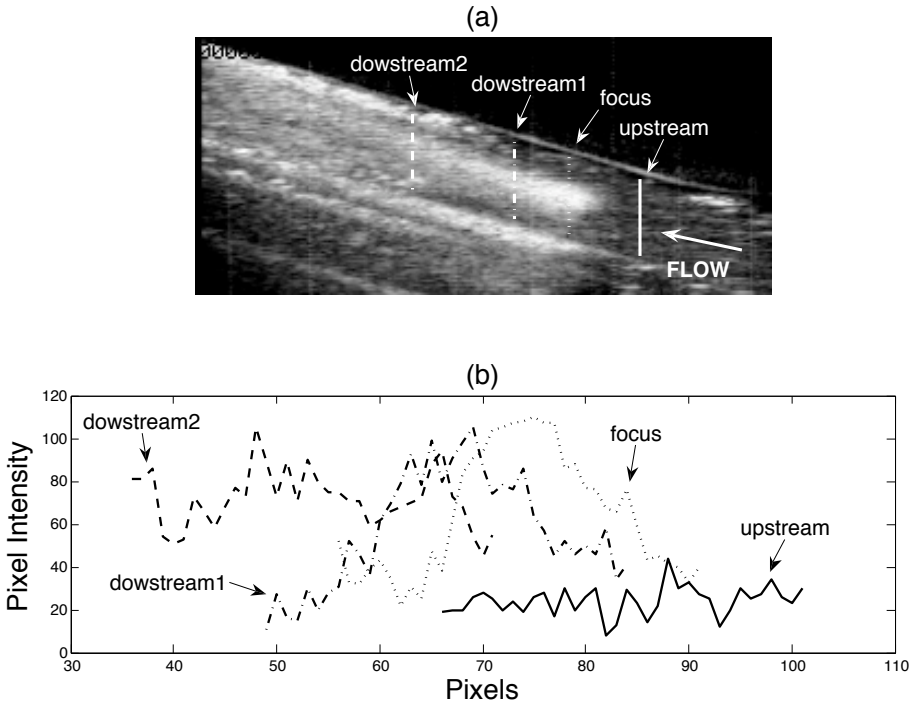

Figure 3.7: a) Lines of pixels taken upstream of the focus, at the focus, and two downstream of the focus are used to evaluate efficiency of ADV. This single frame is taken from a B-mode movie capturing events during an US exposure with 5.4 MPa P_r and 100 Hz PRF. b) The pixel values in these lines are displayed. The lines positioned at the focus and downstream of the focus show elevated pixel intensities when compared to the upstream baseline position.

When comparing PRFs, the efficiency factor is 2-3 times greater at 100 Hz than at 500 Hz. Upon closer examination of the role of PRF (Fig. 3.9), we find that a monotonic relationship does not exist between PRF and efficiency factor; instead, an optimal PRF is apparent.

Fig. 3.10 shows the calculated efficiency factor for US exposures of different amplitudes in an experiment. These data were collected when droplets were mixed with CAs. Unlike the cases in Fig. 3.8 and in the data collected for high PRFs (>100 Hz) in Fig. 3.9 where the efficiency factor at the focus was generally higher than that calculated for either downstream value, the efficiency factors for both downstream lines were in fact higher than that at the focus when CAs were present.

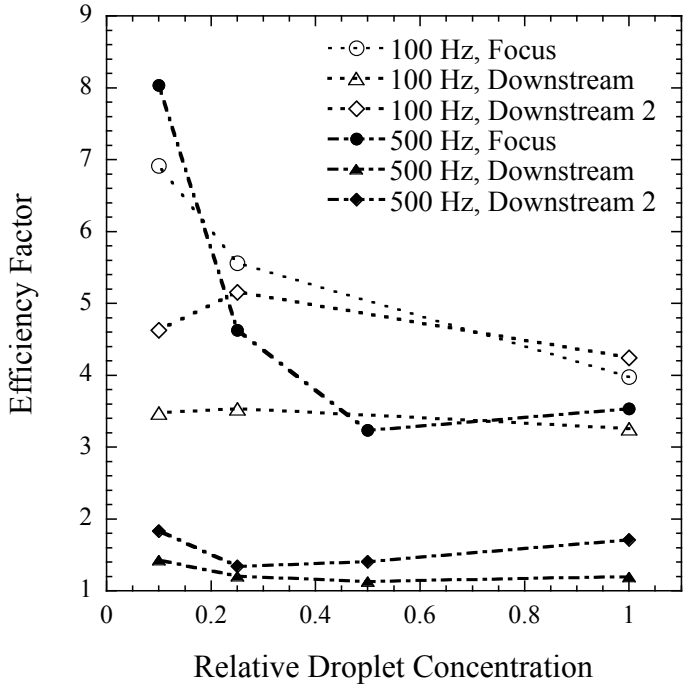

Figure 3.8: The pixels in each cross-sectional line were integrated and normalized to the baseline, i.e. the integrated value of the line placed upstream of the focus, to compute the efficiency factor. Thus, the efficiency factor is the multiplicative factor of the baseline droplet echogenicity. The efficiency factors for the focus, downstream, and downstream 2 positions are plotted against relative droplet concentration where a value of 1 indicates a concentration of 2.85 x 10^6 droplets/mL. A flow speed of 16 cm/s and an amplitude ∼40% higher (5.4 MPa P_r) than the ADV threshold was used for the measurements shown here. Data points represent single experiments in a given setup where the same imaging plane was used.

This inversion could logically be attributed to the difference of an order of magnitude in PRF as droplets and droplets with CA received pulses at PRFs of 100 Hz and 10 Hz, respectively. However, Fig. 3.11 compares sequential IM_x values in a movie for a formulation of droplets and CA (Fig. 3.11a) and droplets only (Fig. 3.11b). Unlike the majority of CA and droplet experiments, the same PRF of 100 Hz was used for these two experiments. The pressure amplitude in these examples for the case of droplets and CA was 200% greater than the measured ADV threshold for said formulation, and the applied pressure for the case of only droplets was 40%

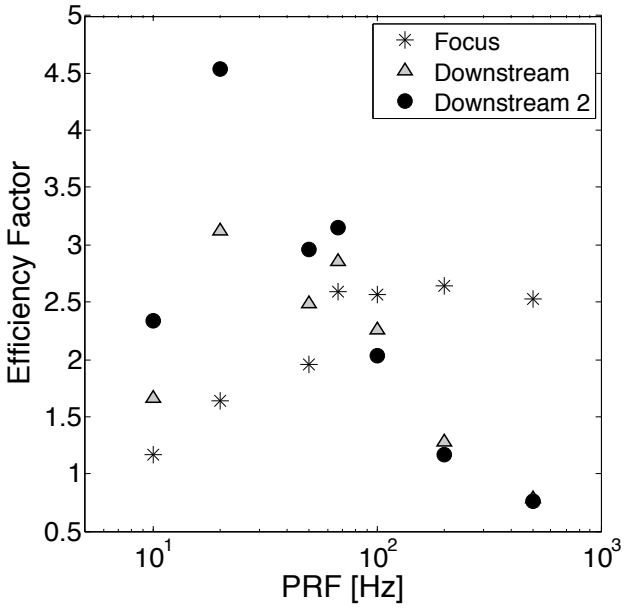

Figure 3.9: A comparison of the efficiency factor for varying PRFs for US exposures at 5.4 MPa P_r. The same calculated droplet concentration of 2.85 x 10^6 droplets/mL were used for these measurements. No CA were added.

greater than the measured ADV threshold for only droplets. Even at an amplitude significantly greater than the ADV threshold, $IM_{f,d1,d2}$ is more sporadic with CA and does not exhibit a clear separation from IM_{up} (Fig. 3.11a). Reducing the PRF to 10 Hz (Fig. 3.11c) shows a more apparent separation of IM_{up} and was therefore used for the majority of experiments involving CA. Nevertheless, the distinct behavior of $IM_{f,d1,d2}$ seems to suggest a different ADV mechanism when CAs trigger the process.

A prevailing trend seen in Figs. 3.8 - 3.10 is that the for the "Downstream 2" M-mode line is greater than or equal to the "Downstream" M-mode line. This increase could be caused by bubble growth, which will cause an increase in echogenicity. The vaporized droplets have traveled a longer distance to reach "Downstream 2" and therefore have had more time to take on gas. For a mean flow rate of 8 cm/s (16 cm/s maximum flow rate), droplets will take approximately 100 ms on average to reach the "Downstream 2" M-mode line, which is more than double the time to reach "Downstream". According to [1], carbon dioxide will begin to

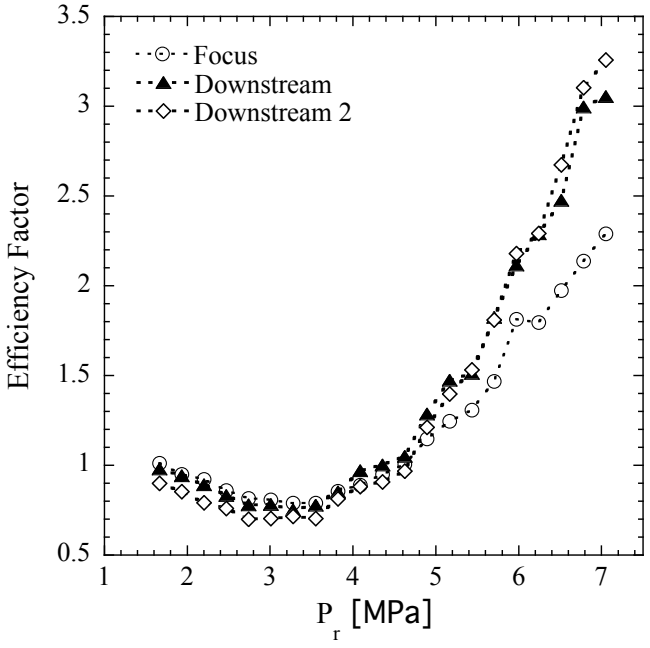

Figure 3.10: The efficiency factor for a range of amplitudes is plotted for US exposure of a combination of droplets and CAs of the same concentration.

diffuse into the bubble at 100 ns while others begin to diffuse at 1 ms, allowing the bubble to exponentially reach its maximum size at 2 s. The bubbles would double their size in 100 ms.

It was considered that radiation force may have played a role in the different efficiency factors at high PRFs. The data evaluated for droplet conversion were all collected with the 10 MHz linear array that was oriented perpendicularly to the direction of propagation of the annular array, and any droplets/bubbles that were created could have been pushed beyond the imaging plane. Thus, a limited number of experiments were performed with the 5 MHz phased array that was situated in the center hole of the annular array. If bubbles experienced radiation force, they would still be detected by the 5 MHz imager. However, the data collected with the 5 MHz imager, which captured the axial plane of the annular array, produced similar results as the 10 MHz imager, which captured the lateral plane. It is therefore unlikely

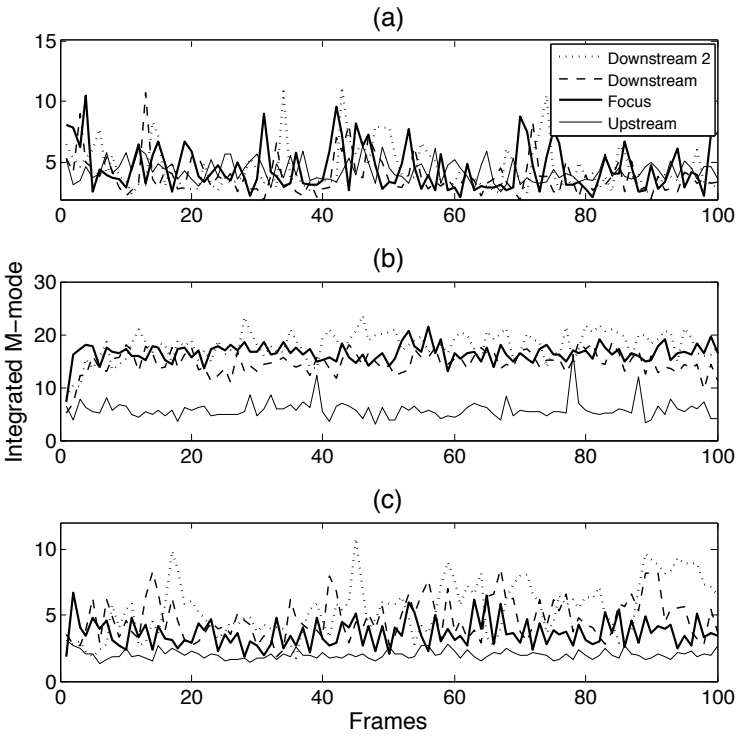

Figure 3.11: IM for sequential frames in a B-mode movie for (a) droplet and CA and (b) droplets only. PRF for both US exposures was 100 Hz. (c) shows IM values for a solution of droplets with CA for US exposures of 10 Hz PRF.

that the reduced number of bubbles detected downstream of the focus was due to radiation force.

3.4 Discussion

3.4.1 ADV Threshold

The threshold experiments that were summarized in Fig. 3.6 show that droplets were reliably vaporized through a TM phantom with 3 dB of attenuation and that ADV is highly dependent on the value of P_r for all formulations. Although the threshold measurements for only droplets with and without attenuation were statistically different, the mean values differed by only 11%. Since the rarefactional half-cycle is dominated by low frequencies, the fundamental frequency appears to

have a large effect on ADV rather than the higher harmonics, although the harmonic content was not substantially altered by the presence of the attenuating material as evidenced by Fig. 3.3.

For the solutions containing CA and droplets, there is inconsistency within the data. When comparing thresholds for the 8 cm/s flow velocity, the same trend as seen with only droplets might be expected. However, the inverse relationship exists as the threshold decreases with the addition of the TM phantom. Increasing the flow velocity to 16 cm/s increases the threshold, which is expected since faster flowing bubbles are more difficult to detect. Still, this threshold is not statistically different than that for droplets and CA at 8 cm/s flow velocity. This inconsistency seems to suggest variability in the interaction of droplets and CA due to perhaps dilution or a focus whose level of aberration changes from experiment to experiment with the propagation path through the TM phantom.

The addition of CA reduced the ADV threshold such that approximately the same amount of input power was required when droplets were vaporized with CA and attenuation, as when droplets were vaporized without CA and without attenuation (Fig. 3.6b). CA lowered the ADV threshold by 1.5-2 times, which is also similar to the results found for repetitive short microsecond pulses at 1.44 MHz in [2]. As discussed in [2] and in Chapter II, the lowered ADV threshold with CAs present indicates that IC external to the droplet may be an initiator for ADV. It appears from Fig. 3.5 that there may be one of two effects that must occur before a vaporization event occurs. First, the fall in $\mathrm{REA}/|\mathrm{REA}_{\mathrm{min}}|$ may be initially due to the disappearance of CA unassociated with IC, but upon reaching threshold, the CAs inertially collapse and trigger the surrounding droplets. Secondly, a certain amount of IC may be required before ADV can be triggered. The diminishing CA levels may be due to contrast disruption. However, ADV does not occur until higher pressures are reached, perhaps due to the increased amount of IC that occurs within

the widening contrast disruption zone or that the strength of the IC collapses are sufficient. In any case, once a requisite amount of IC occurs, ADV thresholds do not change significantly, which was witnessed when an increase in CA concentration did not substantially lower the ADV threshold [2].

It is also possible that IC is the initiator when CA are absent. In this case, the threshold for ADV absent of any CA is half that of IC in saline indicating that the droplets, in providing inhomogeneities in the liquid, could lower the IC threshold in the host fluid. However, it has been shown through high speed photography that cavitation can occur inside the droplet itself [9]. These two mechanisms may be dominant in their own frequency domain as with higher frequencies (or larger droplets), the droplet may interact more with the ultrasound wave.

3.4.2 Efficiency

The efficiency of droplet conversion for a solution of droplets and CA was difficult to quantitatively assess in comparison to results from a solution with only droplets. As discussed in the previous section, the effective disruption zone for CA is larger than the effective vaporization zone for ADV once the ADV threshold is reached. The PRFs used for droplet and CA experiments were therefore lowered by an order of magnitude in order to ensure that the intended population of CA and droplets was replenished for each US pulse. However, a maximum flow rate of 16 cm/s and a 20 Hz PRF seems to be the apparent optimal PRF even when only droplets are present. It may be that, with the flow parameters and center frequency used in these experiments, a slow PRF of 20 Hz (Fig. 3.9) will allow optimal efficiency with minimal power input into the system. However, further investigation is required to compare droplet conversion efficiency with and without the presence of CAs. The amount of bubbles following an US pulse must be measured and differentiated from the remaining droplet and CA population. Optical measurements in a static

environment would allow for single bubble detection for counting, as well as the ability to differentiate between converted droplets and the remaining agents.

When considering that IM is a direct indication of echogenicity, it has been seen that the echogenicity at the focus remains the same when the PRF was high (100, 500 Hz) regardless of droplet concentration (Fig. 3.8). It may be inferred that the same amount of bubbles were generated in the focal region, be it from IC or ADV. However, if pulsing was too frequent, the bubbles that were created at the focus may have been destroyed before leaving the field. With a PRF of 100 Hz, a maximum flow rate of 16 cm/s assuming a parabolic flow profile, and full width half maximum (FWHM) of ∼1.5 mm, each droplet that passed through the field was exposed to at most one US pulse. For average flow, each droplet was exposed to two pulses. A decrease in the efficiency factor is observed if the exposure is increased to 4 pulses per droplet on average. In fact, as mentioned previously, for a 1 MHz carrier frequency, a 20 Hz PRF is more efficient at converting droplets to gas bubbles than higher or lower PRFs (Fig. 3.9).

A simple equation can be used to calculate the optimal PRF for any flow rate and beam width. Assuming that 20 Hz is the optimal PRF, or PRF_{opt}, based on the data points in Fig. 3.9, the ratio between the average transit time for the FWHM beam width ($(beamwidth)/(flowrate)$ =18.7 ms) and the pulse repetition period (PRP) (50 ms) is 0.375 for the parameters used in these experiments. Thus, given an average flow rate v and beam width d,

$$PRF_{opt} = \frac{0.375v}{d}. \tag{3.2}$$

It is noted here that this change in efficiency appears not to be applicable to other frequencies most likely because the threshold for IC increases for higher frequencies and with bubble size [10]. At 4 MHz, data has shown that efficiency increases with PRF as each sequential pulse continues to vaporize a percentage of the remaining

un-vaporized droplets [8]. The efficiency saturates at high PRFs as the remaining droplet population diminishes but does not decrease as in the case with a 1 MHz carrier frequency.

From literature [10][11][12][13], pressure thresholds for inertial collapse can be theoretically predicted. Based on the perfect gas law and an assumed adiabatic collapse, attained temperatures can be related to bubble size (Eq. 3.3)

$$T' = T_0 \left(\frac{R'}{R_0} \right)^{3(1-\gamma)} \tag{3.3}$$

where γ is the ratio of specific heats, T_0 is the initial temperature, T' is the maximum temperature, R_0 is the initial bubble radius, and R' is the minimum bubble radius.

The analytical theory in [12] improves upon that presented in [11], which applies to bubble sizes greater than 10 μm for frequencies below 2.5 MHz. Apfel [12] includes the consideration of surface tension and viscosity, expanding the relevance of the model to bubble sizes greater than 0.5 μm in radius and to frequencies representative of biomedical applications. Holland and Apfel [13] further examined the effects of surface tension to be able to consider bubbles as small as 0.1 μm in radius. Since the bubbles produced by ADV are large, we use the prediction presented in [12],

$$f = \frac{\frac{1}{3\pi R_0}\sqrt{\frac{P_0(p-1)}{\rho}}\left(\sqrt{\frac{2(p-1)}{p}} + \sqrt{\frac{2(p-p_b)}{p}}\right)}{\left(\frac{T'/((\gamma-1)T_0)}{1+\frac{2}{3}(p-1)}\right)^{\frac{1}{3}} + \frac{8\mu}{3R_0}\sqrt{\frac{1}{\rho P_o(p-1)}} - 0.46} \tag{3.4}$$

where f is the insonating frequency, ρ is density, P_0 is the ambient pressure, p is the peak acoustic pressure amplitude normalized to ambient pressure, and p_b is the Blake threshold normalized to ambient pressure.

The theoretical thresholds were computed (Mathematica, Wolfram Research, Inc., Champaign, IL) for various bubble sizes and frequencies (Fig. 3.12) for an initial temperature (T_0) of 310 K, or 37°C, and attained temperatures (T') of 2500 K. The ADV threshold at 1 MHz is slightly higher than the threshold for inertial

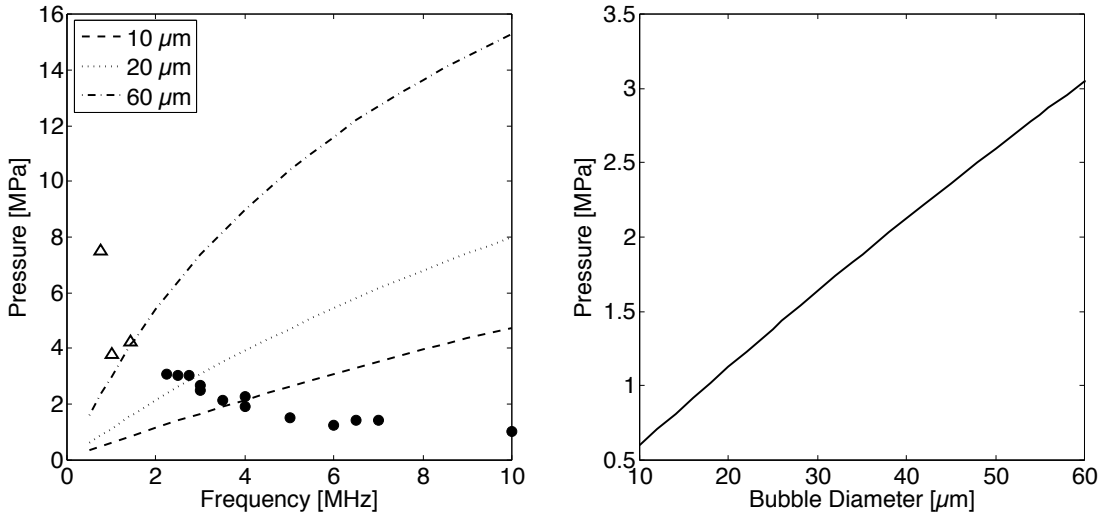

(a) (b)

Figure 3.12: a) Collected data for ADV thresholds and theoretical predictions [12] for inertial collapse for bubbles 10, 20, and 60 μm in diameter. (•) are collected data from [14], (△) are from previous publications for microsecond repetitive pulses [3][2]. b) Theoretical predictions for inertial collapse for bubbles of a range of diameters for insonation at 1 MHz. Bubbles resulting from ADV span the range of 10-60 μm in diameter [14].

bubble collapse at 3 MPa for a bubble with a 60 μm diameter (Fig. 3.12a), the largest bubble size measured from ADV of filtered droplets [14]. Bubbles can be as small as 10 μm, where the threshold for inertial collapse is approximately 0.6 MPa and is lower than the measured ADV threshold (Fig. 3.12b).

It therefore appears advantageous to choose the lowest possible frequency that, for the bubble size distribution created by ADV, has a higher threshold for inertial collapse than it does for ADV. This frequency would be the optimal frequency for tissue penetration while retaining high conversion efficiency. For a 1 MHz insonating frequency, the threshold for inertial collapse increases by almost a factor of three for bubbles ranging from 10-60 μm. It appears that in Fig. 3.12a, bubbles created by ADV may only be safe from inertial collapse upon the arrival of the second US pulse if the frequency is above 4 MHz and the applied pressure is just above ADV threshold. However, 10 μm bubbles only comprise a small percentage of the total number of

bubbles and perhaps are not worth the sacrifice in frequency. The population of 20 μm bubbles is the largest [14], and perhaps should dictate the optimal frequency. Further investigation is needed to ascertain the most advantageous balance between droplet conversion efficiency, insonating frequency, and ADV pressure threshold.

3.5 Conclusion

Transcutaneous ADV was simulated *in vitro* in the experiments presented in this study. It was found that ADV was reliably achieved through 6 cm of attenuation, and that, with the annular array used, there is sufficient power capacity to overcome the effects of even more attenuation. The option to reduce the power input while retaining the ability to vaporize droplets is available with the use of CAs. However, with CAs, PRF must be reduced in order to ensure that a fresh supply of CAs accompany a fresh supply of droplets. PRF also becomes important at these low frequencies where the bubbles created from droplets are subject to inertial collapse if they remain in the acoustic field. At 1 MHz, PRF must be reduced in order to avoid subsequent bubble destruction. Thus, for the different conditions under which ADV may be optimal, there are considerations that must be understood.

REFERENCES

[1] O. D. Kripfgans, J. B. Fowlkes, D. L. Miller, O. P. Eldevik, and P. L. Carson, "Acoustic droplet vaporization for therapeutic and diagnostic applications," *Ultrasound Med Biol*, vol. 26, no. 7, pp. 1177–1189, 2000.

[2] A. H. Lo, O. D. Kripfgans, P. L. Carson, E. D. Rothman, and J. B. Fowlkes, "Acoustic droplet vaporization threshold: Effects of pulse duration and contrast agent," *IEEE Trans Ultrason Ferroelect Freq Control*, vol. 54, no. 5, pp. 933–946, 2007.

[3] A. H. Lo, O. D. Kripfgans, P. L. Carson, and J. B. Fowlkes, "Spatial control of gas bubbles and their effects on acoustic fields," *Ultrasound Med Biol*, vol. 32, no. 1, pp. 95–106, 2006.

[4] L. M. Hinkelman, T. D. Mast, L. A. Metlay, and R. C. Waag, "The effect of abdominal wall morphology on ultrasonic pulse distortion. part i. measurements," *J Acoust Soc Am*, vol. 104, no. 6, pp. 3635–3649, 1998.

[5] O. D. Kripfgans, C. M. Orifici, P. L. Carson, K. A. Ives, O. P. Eldevik, and J. B. Fowlkes, "Acoustic droplet vaporization for temporal and spatial control of tissue occlusion: A kidney study," *IEEE Trans Ultrason Ferroelect Freq Control*, vol. 752, pp. 1101–1110, 2005.

[6] J. E. Parsons, C. A. Cain, and J. B. Fowlkes, "Cost-effective assembly of a basic fiber-optic hydrophone for measurement of high-amplitude therapeutic ultrasound fields," *J Acoustic Soc Amer*, vol. 119, pp. 1432–1440, 2006.

[7] Y. S. Lee, *Numerical solution of the KZK equation for pulsed finite amplitude sound beams in thermoviscous fluids*. PhD thesis, University of Texas at Austin, 1993.

[8] O. D. Kripfgans, *Acoustic droplet vaporization for diagnostic and therapeutic applications*. PhD thesis, University of Michigan, 2002.

[9] O. D. Kripfgans, M. L. Fabiilli, P. L. Carson, and J. Fowlkes, "On the acoustic vaporization of micrometer-sized droplets," *J Acoust Soc Am*, vol. 116, no. 1, pp. 272–281, 2004.

[10] R. E. Apfel and C. K. Holland, "Gauging the likelihood of cavitation from short-pulse, low-duty cycle diagnostic ultrasound," *Ultrasound in Medicine and Biology*, vol. 17, no. 2, pp. 179–185, 1991.

[11] R. E. Apfel, "Acoustic cavitation prediction," *J Acoust Soc Am*, vol. 69, no. 6, pp. 1624–1633, 1981.

[12] R. E. Apfel, "Possibility of microcavitation from diagnostic ultrasound," *IEEE Transactions on Ultrasonics Ferroelectrics and Frequency Control*, vol. 33, no. 2, pp. 139–142, 1986.

[13] C. K. Holland and R. E. Apfel, "An improved theory for the prediction of microcavitation thresholds," *IEEE Transactions on Ultrasonics Ferroelectrics and Frequency Control*, vol. 36, no. 2, pp. 204–208, 1989.

[14] O. D. Kripfgans, J. B. Fowlkes, M. Woydt, O. P. Eldevik, and P. L. Carson, "*In vivo* droplet vaporization for occlusion therapy and phase aberration correction," *IEEE Trans Ultrason Ferroelect Freq Control*, vol. 49, no. 6, pp. 726–738, 2002.

CHAPTER IV

Spatial Control of Gas Bubbles and their Effects on Acoustic Fields

4.1 Introduction

Insonified microbubbles can serve as various tools for tissue treatment. They play beneficial roles in creating lesions by both cavitation and the enhancement of thermal ablation, though the mechanisms for these two classes of therapeutic regimes are distinct.

In inertial cavitation, ultrasound (US) pulses cause bubbles to oscillate nonlinearly and collapse, producing mechanical forces and potentially thermal and chemical effects that impact the surrounding tissue. These effects of cavitation can cause desirable damaging bioeffects in the case of therapeutic targets such as cancerous tissue. With the use of microbubbles, more effective and predictable lesions can be produced than when only treating tissue with high intensity US. [1] demonstrated the useful applications of microbubbles, particularly contrast agents (CA), by showing that the damage thresholds for lesions created in their presence were lowered because of the active role that CA served as cavitation nuclei. Not only were lower intensities required (threshold intensity for a visually apparent biological effect from a single 250 ms burst decreased by a factor of two when microbubbles were in circulation), but also the threshold for producing nonthermal lesions was also more predictable. Additionally, as higher intensities were applied, shorter burst lengths of 48 μs were

required to create lesions with microbubbles present as compared to the 18 ms required without microbubbles, resulting in a reduction in energy by more than two orders of magnitude.

In another application, bubbles insonified by long pulses and/or high pulse repetition frequency (PRF) as considered for imaging or Doppler [2], absorb enough acoustic energy to cause thermal bioeffects. Wu [3] used continuous wave conditions to simulate the temperature rise from a Gaussian beam and a perfectly absorbing disc model for Albunex® contrast agent. Wu found that temperature rises with increasing perfusion lengths, time duration, focal gain, and acoustic power. The highest computed temperature rise was approximately 12°C for a perfusion length of 3 mm, 60 s time duration, 1.67 focal gain, and total acoustic power of 110 mW. Applications such as hyperthermia would benefit from the controlled thermal therapy that microbubbles would provide [4]. Holt and Roy [4] proposed that the use of bubbles would allow for thermal bioeffects with reduced input energies, which in turn provides another advantage of reducing heat deposition in overlying tissues.

Both cavitational and thermal methods of bubble-mediated therapy are compelling arguments for the utility of microbubbles. It would seem even more advantageous if the spatial locations of these bubbles could be controlled, thereby dictating the location of the desired therapy. For example, if the target tissue were a cancerous tumor, the placement of preexisting bubbles in the area of interest would aid in applying therapy to that specific region. This spatial localization is difficult to accomplish when restricted to the vasculature as CA are, although some formulations of CA and droplets may be small enough to be passed into the extravascular space, particularly in the case of cancer with its higher vascular permeability. Attempts to produce bubbles in tissue without pre-existing nuclei present may be undesirable or perhaps counterproductive if the exposures require the application of long durations and/or high pressure amplitudes to generate bubbles through cavitation activity.

One way to control the spatial distribution of microbubbles is through the use of droplets that are subsequently vaporized *in situ* to form bubbles. As developed by [5], these droplets, which are used in the experiments presented in this paper, are filled with dodecafluoropentane (DDFP) liquid and encased in albumin shells. They are superheated at body temperature and can vaporize during insonification, a process known as Acoustic Droplet Vaporization (ADV). When unfiltered, droplet sizes range from <1 μm to 18 μm [6] and produce bubbles that are 20-85 μm in diameter [7]. However, droplets filtered to <6 μm diameter [6] produce bubbles that are approximately 15-45 μm [7], compared to the already formed CA bubbles that are on the order of < 5 μm. Though droplets are not more favorably distributed throughout the body than CA are, they remain as droplets until insonifcation, whereupon they vaporize, grow, and have the potential to lodge. Whether it is simply the localized bubble production or the resulting lodged bubbles, subsequent microbubble-mediated treatment also becomes localized both spatially and temporally.

The generation of bubbles can be spatially controlled with droplets distributed in tissue or in the bloodstream, as focused US can specifically target a location and subsequently vaporize droplets. The bubbles resulting from ADV in the capillary bed would be trapped where the vaporization occurred, as these bubbles are large compared to the capillary diameter. Although spontaneous vaporization is possible (implications discussed in [7], filtering droplets to smaller sizes (<5 μm) reduces these chances because of increased surface tension. As a source of cavitation nuclei, in one experiment using the field of a shockwave lithotripter, Miller et al. [8] showed larger bubbles from ADV to be more effective in producing bioeffects than US contrast agents (CA). Miller and Song [9] also showed that bubbles created by ADV persisted in mouse tumors four days after intravenous droplet injections. It is unclear how long liquid droplets persist *in vivo* since their longevity in circulation depends on the type of animal model, the degree in which the lungs filter the droplets [6], and

their route of excretion, which may be similar to that of perfluorocarbon emulsions [10].

In this investigation, the vaporization of droplets in tissue-mimicking polyacrylamide gels is studied. The manner in which bubble clouds grow due to ADV in tissue or gel may be in part due to bubbles that scatter acoustic energy. When several bubbles are insonified, backscatter can cause an enhanced field in areas adjacent to the pre-existing bubbles, creating conditions favorable for additional ADV and therefore growth in cloud size. Thus, the concept of a plane of bubbles, or "bubble wall, can also create an environment where backscatter can cause further ADV. At the same time, the wall can cause interference in the beam pattern to diminish pressure amplitudes past the wall, thereby lowering the possibility of ADV beyond the wall. Bubble generation can therefore potentially be confined, and consequently, therapy can be localized. Thus the process of bubble cloud generation and the effects of a bubble wall, including specifically its effect on the threshold for ADV, are studied. The preliminary results are presented in this chapter.

4.2 Materials and Methods

4.2.1 Manufacturing Polyacrylamide Gels with DDFP Droplets

DDFP droplets were manufactured according to the process described by [5]. A solution of bovine albumin (A3803, Sigma-Aldrich, St. Louis, MO) and saline at a concentration of 4 mg albumin/ml saline was made and vigorously shaken with a VWR Scientific Vortex Genie (Model G-560). A pipette was then used to distribute 750 μl of the albumin-saline solution into separate vials. Due to rapid evaporation, liquid DDFP was added to each albumin-saline containing vial according to weight. After 425 μg (slightly more than the target volume of 250 μl to provide a margin for evaporation) of DDFP was measured, the vials (Cat. No. 223693, Shamrock Glass

Co., Seaford, DE) were immediately sealed with a rubber stopper and metal cap (Cat. No. 224100-094 and 224177-01, Shamrock Glass Co.) to prevent the further evaporation of DDFP. Lastly, the vials were shaken for 30 s at 5000 cycles/min with an amalgamator (Crescent Dental Mfg. Co., Lyons, IL).

Polyacrylamide gels (7.5% w/v) were made using a stock solution of bis-acrylamide (A3449, Sigma-Aldrich, 19:1, 30% w/v) solution diluted with deionized water at a ratio of 1:3 (bis-acrylamide to water). This solution was degassed for 20-25 min in a vacuum chamber with approximate pressures of 50 mm Hg. The DDFP droplets were then added to the solution and immediately followed by 10% ammonium persulphate (A3678, Sigma-Aldrich) and tetramethylenediamine (T8133, Sigma-Aldrich) to initiate cross-linking. The solution (80-100 ml) was gently stirred to minimize the reintroduction of gas and poured into a plastic container 5 x 5 cm^2 in cross-sectional area. Upon completion of cross-linking (approximately 20 min), a layer of deionized water was added to the surface of the gels to prevent dehydration.

In order to produce a reasonable number of microbubbles, a concentration of 5000 droplets/ml was used for all gels. The stock droplet solution of 10^7 droplets/ml [5] was diluted to 10^6 droplets/ml, and 5 μl of this diluted solution was added for each ml of polyacrylamide gel. Gels contained droplets of one of three size ranges: (1) unfiltered droplets with a mean diameter of 4 μm [5], (2) droplets that were filtered with a 20 μm and 16 μm syringe filter (Whatman, Maidstone, England) in series, or (3) droplets that were filtered further by the addition of 8 μm and 5 μm filters. After using a 5 μm filter, the maximum droplet diameter is 6 μm [6]. The syringe filters used consisted of filter paper of varying pore sizes contained in housing compatible for syringe use. Droplet solutions were pushed through these filters, and larger droplets were eliminated at each filter according the pore size.

4.2.2 Acoustic Source

An annular array transducer (Imasonic, Besançon, France) was used, which contains 9 annuli of equal area that are bisected to produce 18 elements. The array contains a central hole such that the active outer and inner diameters are 145 mm and 68 mm, respectively. The radius of curvature for the array is 100 mm and is operated at 750 kHz. The array is driven with custom electronics (photograph of system seen in Fig. 4.1) where, for these experiments, all elements were driven in-phase. This produced the nominal focal position assumed for all experiments and a field calibration, which was performed with an in-house fiber-optic hydrophone [11]. The data was fit with a third degree polynomial and the resulting range of pressures is shown in Fig. 4.2.

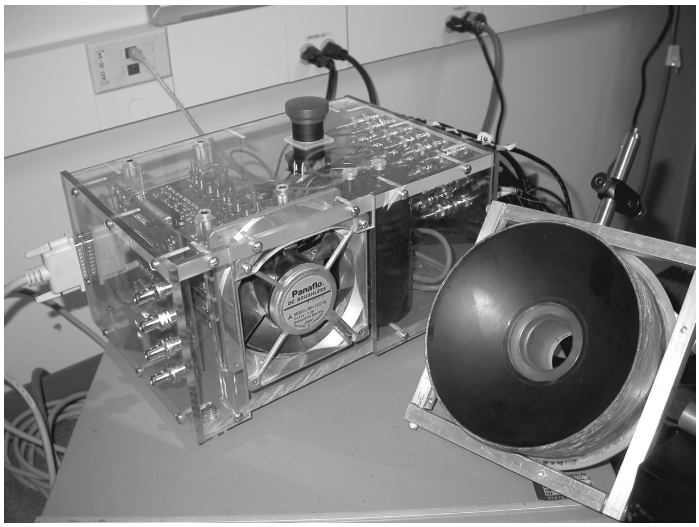

Figure 4.1: 18-element annular array with associated amplifier.

4.2.3 Experimental Setup

The array was mounted on a motorized positioning system (S83-136-MO motors, Compumotor; DRP60-1 controller, Parker; 120 V power supply, Daedal-Hannifin Corp., Rohnert Park, CA), which was used to accurately target locations inside a

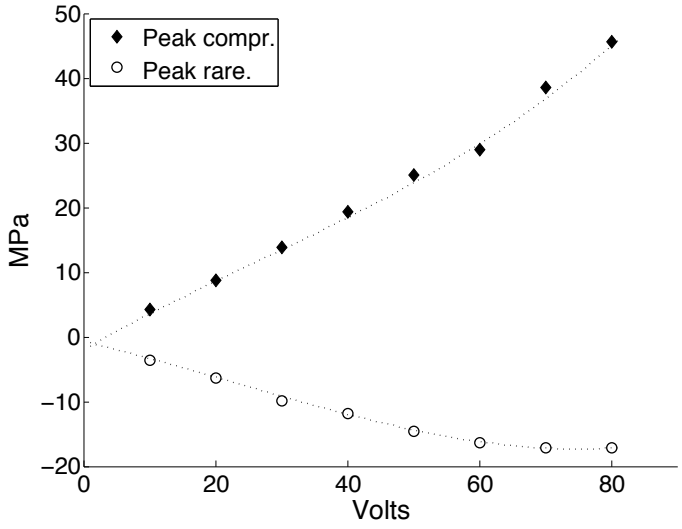

Figure 4.2: Calibration of the 18-element annular array with operating frequency of 750 kHz and geometric focus of 10 cm. The data were fit with a third order polynomial. This array is the therapy transducer used to create bubble clouds.

polyacrylamide gel. A 5 MHz phased array (FPA 5 MHz 2B, System Five, General Electric Vingmed, Milwaukee, WI) was placed inside the center of the annular array to acquire on-axis images. The gel was mounted in a fixed position in front of the annular array. The setup is shown in Fig. 4.3a. Fig. 4.3b illustrates another aspect of the experimental setup and will be described later in this section.

Each gel was exposed approximately 40 times with US, with each exposure placed in a single different location 5-10 mm apart depending on the size of the resulting cloud, and varying in pressure amplitude and number of pulses. Three conditions were studied: cloud generation by US exposure (1) in the absence of a bubble wall, (2) focused at a previously formed bubble wall, and (3) focused past a previously formed bubble wall. In Cases 2 and 3, exposures were made 15-60 min after the formation of the bubble wall. These experiments were performed with droplets of the various sizes described earlier. A B-mode frame from the central 5 MHz phased array was captured before and after each exposure, and the images were quantified and compared in Matlab (The MathWorks, Inc., Natick, MA). The phased array was

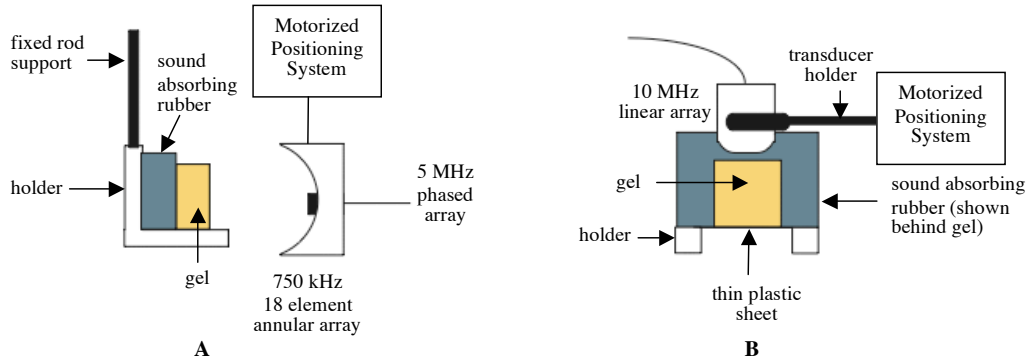

Figure 4.3: Experimental setup. The schematic drawing in (a) shows a side view of the arrangement for an ADV threshold experiment where the phased array is used to detect droplets vaporized by the annular array. (b) shows a frontal view of the arrangement for creating a bubble wall. After making a wall, the gel is then repositioned to the configuration in (A) for further threshold experiments. The same holder is used in both cases and is depicted in two views here.

operated at low power with a mechanical index (MI) of 0.4 to minimize its acoustic effects on the existing bubble wall during exposures from the annular array.

4.2.4 Analysis of B-mode Images

Fig. 4.4 shows three examples of B-mode images acquired from the 5 MHz phased array used for monitoring bubble activity. Regions of interest (ROI) were defined for each bubble cloud generated and were then compared with the same ROIs in the B-mode images acquired before US exposure. Four ROIs were chosen as numbered in Fig. 4.4 for the three different conditions that were previously described. For ROIs 2-4, where the bubble wall contributed to backscatter in the acoustic field, the position of each ROI was chosen to exclude the bubble wall in order to improve detection of new bubble formation.

Cloud size and average pixel intensity were then determined from each ROI. First, a threshold requirement for pixel intensity was applied to discern which pixels constituted part of the cloud and which were background scatter from the gel containing unconverted droplets. This threshold was determined as two standard

deviations above the mean pixel intensity in an ROI containing a gel and bubble clouds. Statistics of the distribution of pixel intensities were not taken into account in determining the threshold value, though a histogram of the pixel intensities inside an exemplary set of ROIs, as seen in Fig. 4.5, show that the value is sufficient in order to eliminate background noise and determine ADV threshold. The number of pixels above this threshold defined the bubble cloud size. To find the average pixel intensity, a mean pixel value of the ROI was computed after the thresholding was applied.

The data were then fit in Kaleidagraph (Synergy Software, Reading, PA). The data for experiments excluding a bubble wall were fit with three linear lines (Eq. 4.1) and those including a bubble wall were fit with two lines (Eq. 4.2). The reason for the two different fits will be discussed subsequently. The equations are shown below, where y is a characteristic of the cloud (intensity or size), p is pressure, and a_1 to a_6 are adjustable parameters that define the equation of the line segment. A windowing rect function w_k is multiplied to each line segment and defines the threshold value.

$$y = (a_1 \cdot (p - a_2) + a_3) \cdot w_1 + (a_4 \cdot (p - a_5) + a_3) \cdot w_2 + a_6 \cdot w_3 \tag{4.1}$$

$$y = (a_1 \cdot (p - a_2) + a_3) \cdot w_1 + (a_4 \cdot (p - a_5) + a_3) \cdot w_2 \tag{4.2}$$

4.2.5 Creating the Bubble Wall

The bubble walls were created as shown in Fig. 4.3b with a 10 MHz linear array (FLA 10 MHz 1A, System Five, GE Vingmed, Milwaukee, WI) since the ADV threshold has been shown to be lower at higher frequencies [7]. The MI was 1.2. The wall was created in the plane orthogonal to the central axis of the annular array. The imager was mounted on a motorized system to create walls of varying thicknesses. To create a plane of bubbles and in order to prevent shadowing, the electronic focus of the imaging transducer was manually moved from the lower region of the gel

(furthest from the transducer) to the upper (closest to the transducer). The focus was shifted every 3-5 s when no further ADV was visualized. The imaging plane was also translated in 0.5 mm steps up to 1 mm in the elevational direction on either side of the initial position to create bubble walls of 1-2 mm in thickness. As the imaging probe was translated to a new plane to increase the thickness of the bubble wall, the method of moving the electronic focus to prevent shadowing was followed for each plane. Variations in the bubble number density occurred due to variability in the droplet distribution and possibly inhomogeneities in the gel matrix.

The wall was characterized in terms of its backscattering and attenuation properties. The experimental setup to determine these characteristics, as shown in Fig. 4.6, is similar to that shown in Fig. 4.3a, with the exception that the holder was positioned at a 180 degree rotation about the rod to minimize interference with the hydrophone. For these measurements, the sound absorbing rubber was removed from the setup, and a window on the back of the holder was created to allow transmission of US. A single element passive transducer (Valpey Fisher, Hopkinton, MA) with a nominal center frequency of 5 MHz and nominal focus of 10 cm placed in the center of the array received backscatter signals with the associated weighting of harmonic signals from the bubbles. A hydrophone (NTR Systems, Model TNU100A, Seattle, WA) operating approximately between 1 MHz and 20 MHz was positioned on the opposite side of the gel sample to receive the US signals transmitted through the gel. We note that the carrier frequency of 750 kHz lies outside of the nominal range of the hydrophone, but only relative measurements are considered for the characterization of the bubble wall. The annular array was used as the transmit source (driven with 11 cycles or 15 μs pulses, 200 Hz PRF, 3 MPa rarefactional pressures) while the hydrophone received the transmitted acoustics through the bubble wall, and the 5 MHz passive transducer received the echoes off of the bubble wall. The backscattered and transmitted signals were recorded from a digital oscilloscope (LeCroy 9384L,

Chestnut Ridge, NY) from a droplet-containing gel lacking a bubble wall, then with the focus positioned at a bubble wall, and with the focus positioned distally to the same wall. The gel was translated in the transverse plane to evaluate the homogeneity of the bubble wall.

Since the eventual application of the bubble wall is *in vivo*, these measurements (and experiments) were made with a low frequency of 750 kHz. Higher frequencies may show similar or stronger results in attenuating and backscattering properties of the bubble wall because of off-resonance and/or greater distal attenuation.

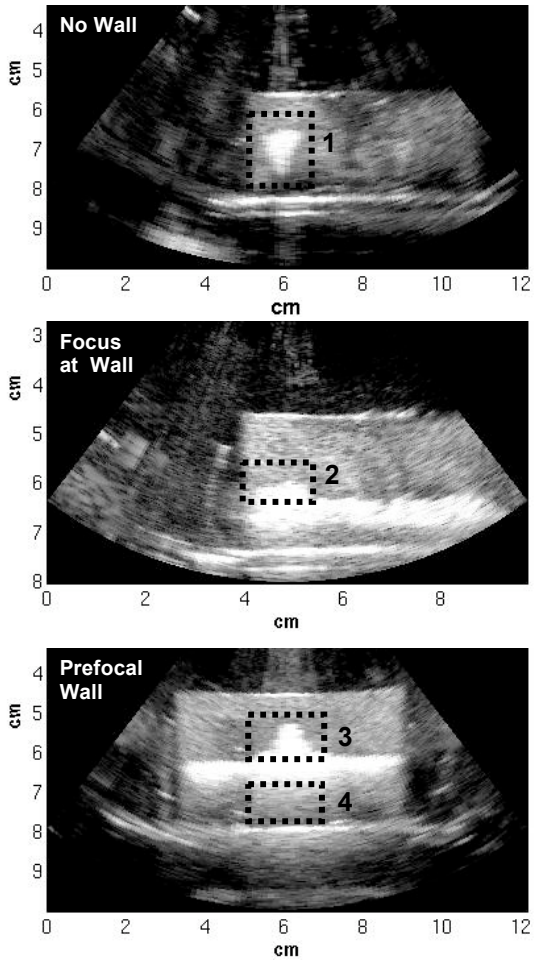

Figure 4.4: Examples of B-mode images taken from a 5 MHz phased array placed in the center of the annular array. These images were used to characterize bubble clouds as a function of rarefactional pressure. US exposures for three different conditions (as labeled) are pictured here, and the ROIs surrounding them (numbered 1-4) are defined by the dotted lines. The pixels in each ROI were evaluated in terms of pixel intensity and number of pixels per cloud.

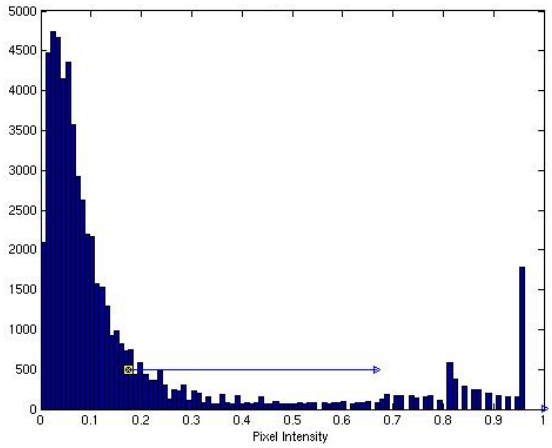

Figure 4.5: Histogram of the pixel intensity of four gels. Threshold was set at 0.67, which is approximately two standard deviations above the mean pixel intensity as indicated by □ (mean) and → (two standard devations).

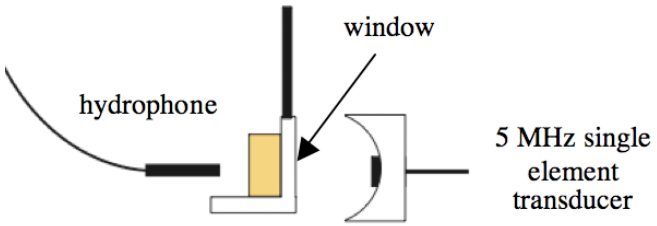

Figure 4.6: Experimental setup for the characterization of a bubble wall. The annular transducer transmitted ∼15 μs pulses at a PRF of 200 Hz and rarefactional pressure of ∼3 MPa. The echoes and the transmitted US were received by the 5 MHz transducer and hydrophone, respectively. A window in the vertical wall of the holder that was approximately the size of the cross-sectional area of the gel allowed US transmission through the gel.

4.3 Results

The parameter space associated with US pulses that can produce ADV is large. Frequency, PRF, pulse length (and consequently duty cycle), and amplitude along with their relationship to droplet size and acoustic medium all potentially affect ADV. To begin to understand the impact of these parameters on the creation of bubble clouds, only the effects of the number of pulses applied and pressure amplitudes of these pulses on three ranges of droplet sizes were investigated. Each pulse contained 15 cycles at 750 kHz for a pulse duration of 20 μs. The PRF was held constant during all experiments at 100 Hz, which maintained a low duty cycle (0.2%) and correspondingly low time average power. These pulse parameters prevent local heating that could arise from higher time average powers, though it has been shown that increasing the ambient temperature alone up to 60°C [5] does not cause droplets to vaporize. It is thus probable that ADV is not due to local heating.

The images presented in this section of the paper were taken with a digital camera. Before each photograph, the gels were sectioned to reduce the amount of overlying gel but to include the entire bubble cloud.

As might be expected intuitively, as pressure amplitudes increased, so did the size cross-sectional area of the resulting bubble cloud. A comparison between the resulting clouds from pressures of 9.8 MPa and 14.7 MPa peak rarefactional pressures is seen in Fig. 4.7c and 4.7d. The figure also shows various ranges of droplet sizes (Fig. 4.7a-4.7c) vaporized with the same pressure amplitude. Both clouds generated with 9.8 MPa rarefactional pressures in gels with 16 μm and 5 μm droplets are approximately 7 mm in length (Fig. 4.7b and 4.7c) while the cloud formed from unfiltered droplets is approximately 10 mm in length (Fig. 4.7a). Measure of length is defined in the longitudinal direction in all photographs.

Varying the number of pulses does not significantly change the size of the bubble cloud. Shown in Fig. 4.8, clouds created with rarefactional pressure amplitudes of

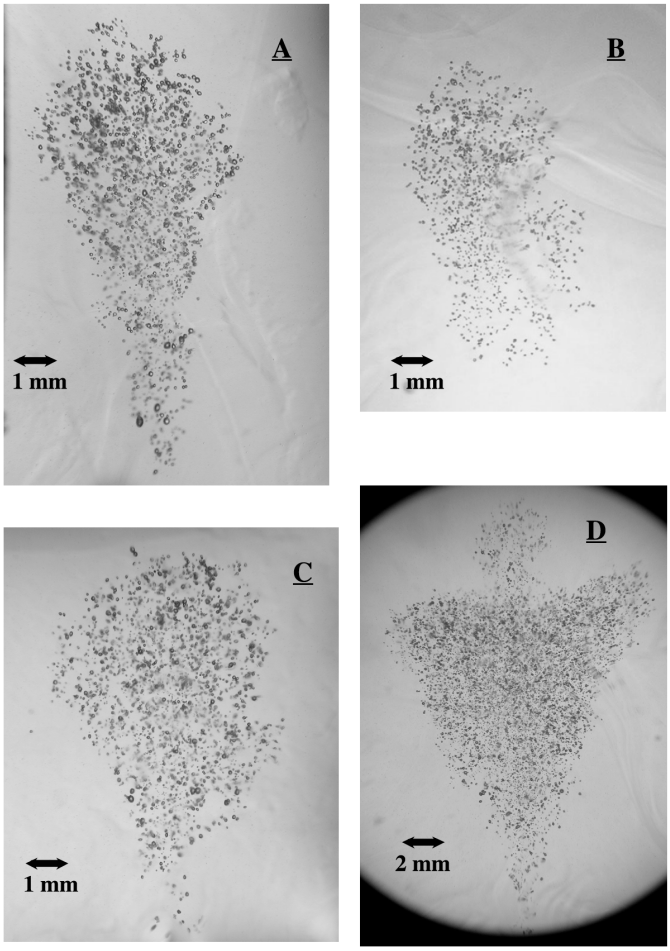

Figure 4.7: Optical images of bubble clouds generated with 200 pulses in 7.5% polyacrylamide gels. (a) unfiltered droplets; (b) droplets filtered to 16 μm; (c) droplets filtered to 5 μm all at 9.8 MPa (rarefactional); (d) 14.7 MPa, droplets filtered to 5 μm. A discussion of the cloud shape is included in the text.

9.8 MPa were approximately 9 mm in length. The cloud created with 20 pulses (left) takes the characteristic cigar shape of the focal zone whereas the cloud created with 1000 pulses (right) appears to take the teardrop shape that is typical of lesions distorted by enhanced prefocal absorption associated with cavitational processes [12][13][14]. Thus it appears that with 20 pulses, ADV occurs in the focal zone, where the acoustic field is at its highest intensity. Further distal ADV is prevented during additional insonification by the shadowing caused by the initial droplets vaporized by the first few pulses; instead, energy is backscattered, causing the cloud

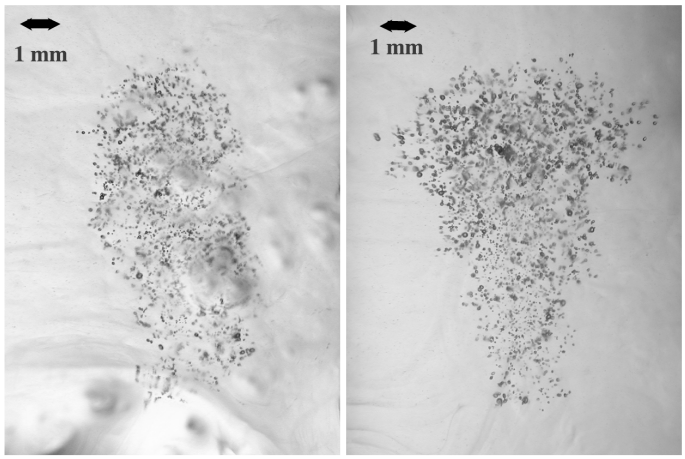

Figure 4.8: (left) Image of the cigar-shaped cloud generated by rarefactional pressures of 9.8 MPa with 20 pulses, and (right) teardrop-shaped cloud generated by 9.8 MPa with 1000 pulses. Droplets were unfiltered in both cases.

to grow toward the transducer. Since ADV occurs when pressures reach a certain threshold, it seems unlikely that additional pulses will cause further ADV, and thus, the cloud eventually stops growing.

When comparing Figs. 4.7 and 4.8, some variability in cloud shape and size is observed. This may be due to inhomogeneity in droplet and/or bubble distributions as well as in the gel structure. However, a tendency of growth toward a teardrop shape exists with increasing amplitudes and pulse numbers.

Observing the growth of these clouds (Figs. 4.7-4.8) shows that ADV occurs in a backward propagating direction toward the transducer. Considering that backscattered signals can enhance the proximal field, it seems that backscatter could help create conditions for ADV. If, perhaps, the scattering bubbles already existed, spatially localized ADV could occur. In other words, bubbles might be strategically placed to cause further bubble generation in a controlled fashion. A plane of bubbles, in particular, can scatter US energy in a way to produce superthreshold ADV pressure amplitudes in desired locations. This concept of using a plane of bubbles, or "wall," is demonstrated in Figs. 4.9 and 4.10. The ability to achieve these conditions

favorable for the creation and use of a bubble wall *in vivo* will depend on the tissue selected, flow conditions, and the appropriate placement of the acoustic field. These issues are considered further in the Discussion section.

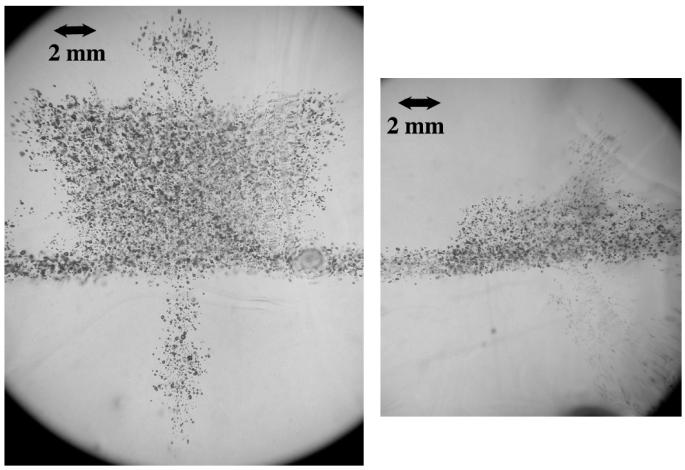

Figure 4.9: Both images show clouds generated by rarefactional pressures of 14.7 MPa with 200 US pulses propagating from the top of the photograph. On the left, the focus of the annular array is positioned on a nominally 1 mm wall, where some leakage occurs. On the right, the focus is positioned past the wall, exposing the bubble wall to the lower prefocal amplitudes, which are less likely to leak through the wall.

Fig. 4.9 shows two US exposures of 14.7 MPa pressure amplitudes in a gel containing droplets with interference from a nominally 1 mm thick bubble wall. The image on the left shows the resulting cloud when the focus, where the amplitude is the greatest, is positioned at the wall. With these high amplitude pulses, some leakage and ADV occurs past the wall. The image on the right shows that when focused past the bubble wall, leakage is less likely to occur because pressure amplitudes roll off prefocally and the wall is more effective at preventing leakage when it coincides with the location of the lower prefocal pressures.

Distal ADV may be prevented by increasing the backscatter and attenuation of the bubble wall, properties which can be varied by increasing the thickness and/or density of the wall. However, since density is dictated by the already high droplet

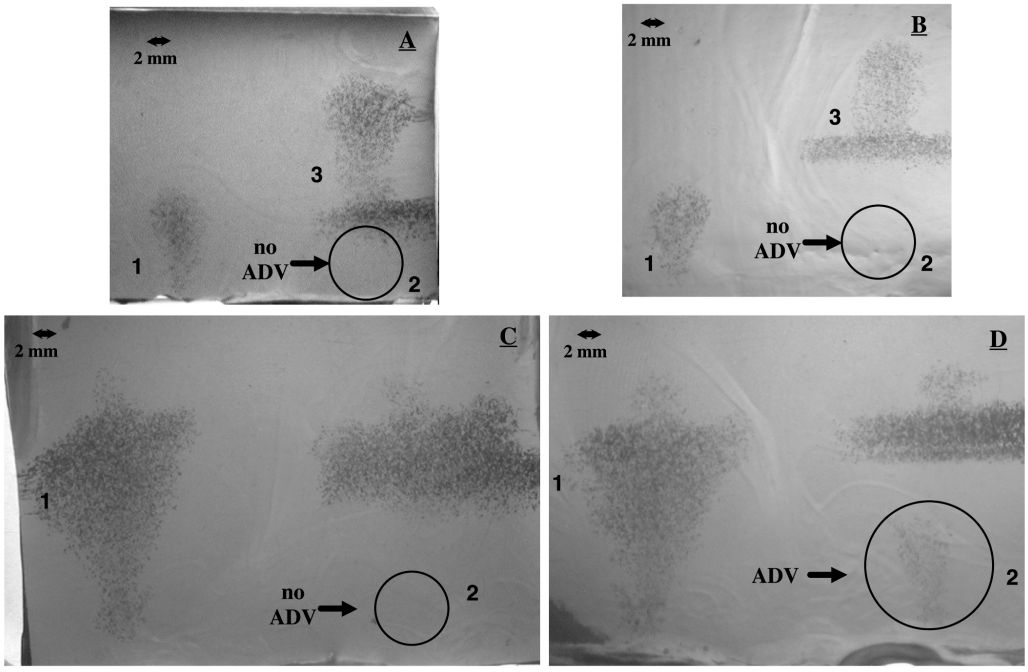

Figure 4.10: Optical photographs demonstrating the effects of a bubble wall created in a gel with droplets filtered to 5 μm. Pressure amplitudes for each exposure is the same for a given photograph and are stated as follows: (A) 1 mm thick bubble wall, 9.8 MPa; (B) 2 mm thick wall, 9.8 MPa; (C) 2 mm thick wall, 14.7 MPa (D) 2 mm thick wall, 14.7 MPa. The numbers indicate the sequence of US exposures, where the focus of the therapy array (annular transducer) is first translated laterally from positions 1 to 2, and then axially from 2 to 3. The direction of US propagation is from the top of all photographs. Locations labeled 1 correspond to exposures in the absence of a bubble wall, those labeled "2 correspond to exposures focused past a wall, and those labeled "3 correspond to exposures focused in front of a wall.

concentration used in these experiments, only wall thickness was changed. Fig. 4.10 compares the size and shape of bubble clouds in the presence of $\sim$1 and $\sim$2 mm thick bubble walls. Three cases, as numbered in Fig. 4.10, were demonstrated in the same gels in the following order: a 200 pulse US exposure (1) in the absence of a wall (left side), (2) focused past a wall (translated only laterally to the right, where the circles indicate the location of the focus), and (3) focused in front of the wall (subsequently translated only axially toward the transducer). The images show these three cases side by side in the same gel, where the direction of US propagation

is from the top of each photograph. Figs. 4.10a and 4.10b show all three cases while Fig. 4.10c and 4.10d show the first two.

The clouds created in Fig. 4.10a and 4.10b were vaporized by the same rarefactional pressures of 9.8 MPa with the varying parameter being a difference in wall thickness, where the nominal thickness in Fig. 4.10a is 1 mm and that of Fig. 4.10b is nominally 2 mm. Figs. 4.10c and 4.10d show two examples of clouds created by larger pressures of 14.7 MPa and show how they are affected by 2 mm thick walls.

For smaller rarefactional amplitudes of 9.8 MPa, a 1 mm thick wall is sufficient to prevent ADV past the wall (Fig. 4.10a, Case 2) as is a 2 mm thick wall (Fig. 4.10b, Case 2). However, a 1 mm wall is of insufficient thickness to completely block pulses of higher amplitudes, as demonstrated previously in Fig. 4.9, while a 2 mm wall (Fig. 4.10c) shows that it is effective in preventing ADV on the distal side of the wall with US of higher amplitudes. In essence, the wall seems to serve the same purpose as the bubbles created during the first few US pulses; both create backscattering conditions that cause ADV propagation back towards the transducer. It is necessary, though, that the plane of bubbles be large enough to span the beam of the transducer to provide sufficient interference. Fig. 4.10d (Case 2) shows that US can still cause ADV to occur if it propagates partially around the side of the wall without any aberration.

Fig. 4.10c shows that while there is distal shielding, ADV still occurs on the proximal side of the wall (Case 2) due perhaps to the backscattering and the resulting enhanced field. Because of this cloud formation, exposures in which the US was focused in front of the bubble wall were not performed in the experiments seen in Figs. 4.10c and 4.10d. Additionally, US with rarefactional pressures of 9.8 MPa focused on the proximal side of the bubble wall (Figs. 4.10a and 4.10b, Case 3) create bubble clouds that are larger at the base (near the focus) than those created in the walls absence (Case 1). This may be accounted for by the post-focal beam

reflecting off of the bubble wall, creating superthreshold pressure conditions on the proximal side of the wall to cause further ADV and therefore enlarge the cloud base.

4.3.1 ADV Thresholds

Plots shown in Fig. 4.11 illustrate quantification of the threshold level of ADV for three cases for gels with droplets with wall and focus cases as follows: (1) no bubble wall, (2) with US focused at a bubble wall, and (3) with US focused distal to a bubble wall. The extrapolated threshold values are listed in Table 4.1. These cases, all with exposure to 200 pulses, were performed for droplets filtered to 16 μm and for 5 μm to investigate the impact of size on bubble wall properties and thresholds. The data were obtained from B-mode US images taken from the 5 MHz phased array placed in the center of the therapeutic array as was described in Fig. 4.4.

Table 4.1: Summary of threshold values extrapolated from curve fits.

Threshold detection method	**Gel containing droplets (MPa)**	**US focused at bubble wall (MPa) (MPa)**	**US focused distal to wall, ROI proximal to wall (MPa)**
5-μm droplets			
Cloud size	7.51±0.02	3.93±0.50	11.61±0.81
Pixel Intensity	7.53±0.18	4.17±0.42	11.63±0.80
16-μm droplets			
Cloud size	7.50±0.15	3.53±0.78	9.91±1.89
Pixel Intensity	7.79±0.01	3.97±0.21	9.79±3.94

Values indicate the best fit approximation ± standard error values. In the case of analyzing an ROI at the focus with a prefocal bubble wall in place, the curve fits are almost completely linear, making distinguishing a threshold value unclear.

As previously mentioned, the data were fit to either two or three line segments (Eqs. 4.1 and 4.2), the reasons for which are discussed here. Three line fits are required when no bubble wall is present because the first droplets that are converted to gas bubbles vaporize in the spatial peak of the acoustic field, the focus. The spatial extent of the focus occupies a certain volume, thereby causing perhaps a

localized group of the droplets to vaporize at approximately the same time, a process that can be reflected in the jump in cloud size around the ADV threshold. This may not be the case with the presence of a scattering bubble wall, where the data lacks the jump apparent in the aforementioned data. In this case, a two-line regression fit the data well, as there was no step function at the threshold for detectable bubbles.

Because existing bubbles interfere with the acoustic field of the annular array, it is possible that the field of the imaging phased array could be disturbed as well. To confirm echoes that may originate from the proximal side of the bubble wall, further B-mode images were taken with a 10 MHz linear array during some experiments, where the transverse plane was oriented along the axis of the annular array. Fig. 4.12 shows the results from such an experiment for droplets filtered to 16 μm (Fig. 4.12a) and 5 μm (Figs. 4.12b and 4.12c). Average cloud pixel intensities were analyzed from the 5 MHz phased array and 10 MHz linear array and roughly correspond, though discrepancies may occur due to the different point spread functions, speckle patterns, and viewing directions of the two imaging probes. Individual data points demonstrate the variations that may occur in the bubble wall and how it may affect ADV when pressures are above the threshold. Fig. 4.12a shows the results from one experiment, and Fig. 4.12b and 4.12c both show data from a second experiment with the smaller sized droplets.

4.3.2 Characterization of Bubble Wall

As shown in Fig. 4.13, the increase in mean backscatter when the bubble wall is formed in the gel is approximately 25.5 dB and 22.7 dB for the two locations of the focus. The higher backscattered signal when focused at the bubble wall (Fig. 4.13a) is most likely due to the high amplitudes in the focal zone that are reflected back off the wall, whereas moving the focus past the wall (Fig. 4.13b), will reflect lower prefocal amplitudes in the beam. Both cases show a maximum backscatter of

approximately 40 dB and the minimum to be almost 0 dB, indicating an apparently large variability in bubble density and/or bubble size distribution. Values expressed in dB are relative to backscatter and attenuation measurements made in a gel with unvaporized droplets.

Measurements of the transmitted signals show similar mean attenuation of 12.4 dB and 12.5 dB as well as similar standard deviations of 4 to 5 dB when focused at the bubble wall (Fig. 4.13c) and when focused past the wall (Fig. 4.13d), respectively. Maximum attenuation values are approximately 27 dB, though non-attenuating areas are also present.

Though US is backscattered and attenuated similarly on average for both positions of the focus with respect to the bubble wall, it appears that focusing past the bubble wall defocuses the beam. Thus the spatial distribution of wall attenuation is more uniform (Fig. 4.13d), as evidenced by the fewer finely defined areas of minima and maxima that are seen in Fig. 4.13c when the focus is positioned on the wall.

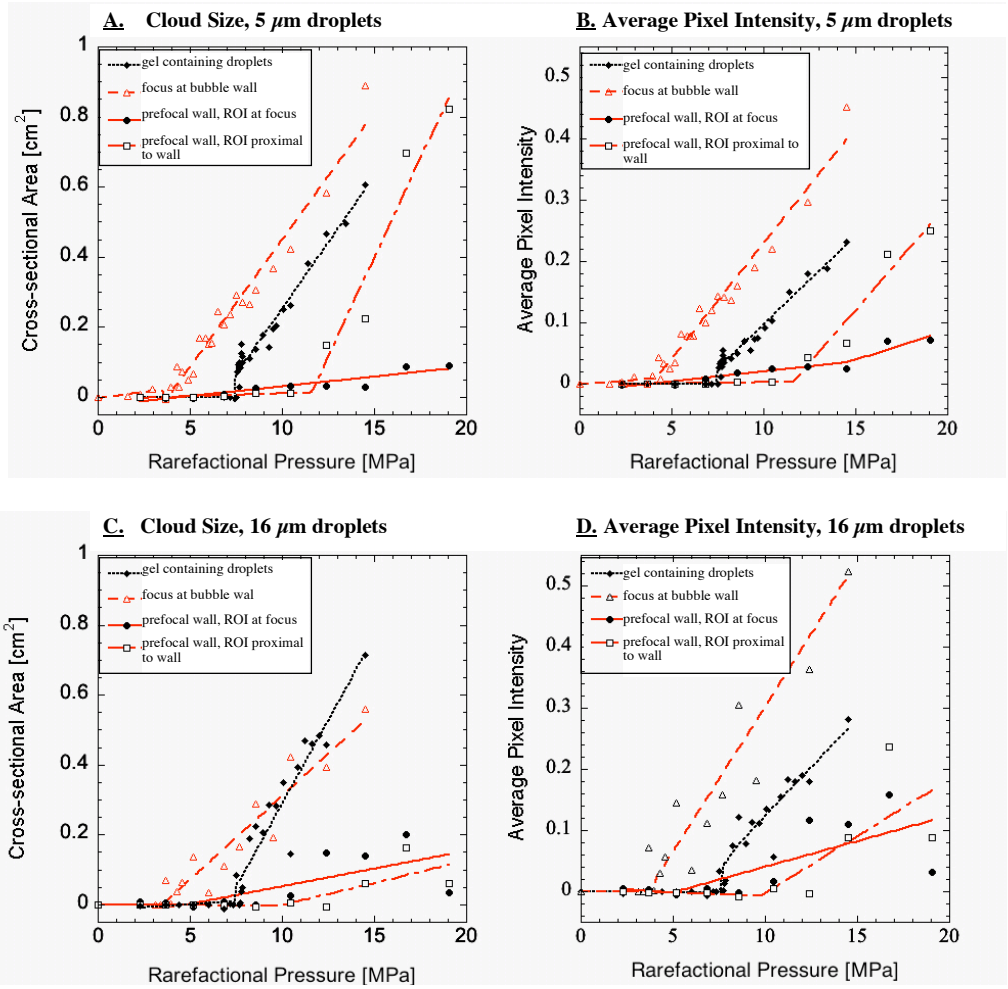

Figure 4.11: Plots of cloud size and intensity as a function of rarefactional pressure for two droplet distributions. Data were taken from B-mode images from a 5 MHz phased array, where the imaging and therapeutic planes were aligned. Both size and intensity increase with pressure, indicating that the overall cloud size grows as well as the echogenicity.

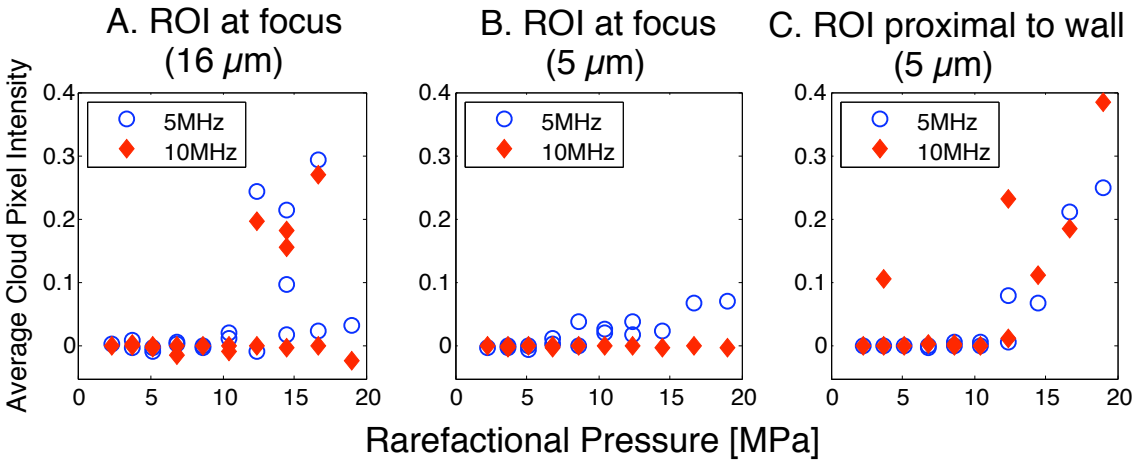

Figure 4.12: Results from experiments involving a prefocal bubble wall. The plot in A shows data from focal ROIs with 16 μm filtered droplets, and B and C show averaged data from focal and proximal ROIs, respectively, with 5 μm droplets. B-mode images were taken from an on-axis 5 MHz phased array (axial view) and a 10 MHz linear array, where the transverse plane was oriented parallel to the axis of the annular array (coronal view). Data from the two imaging probes confirm that the bubble wall can both reflect and consequently shield distally. Data points illustrate the variability that can occur in bubble walls and their resulting efficacy in serving as a shield, at least with high pressure beams.

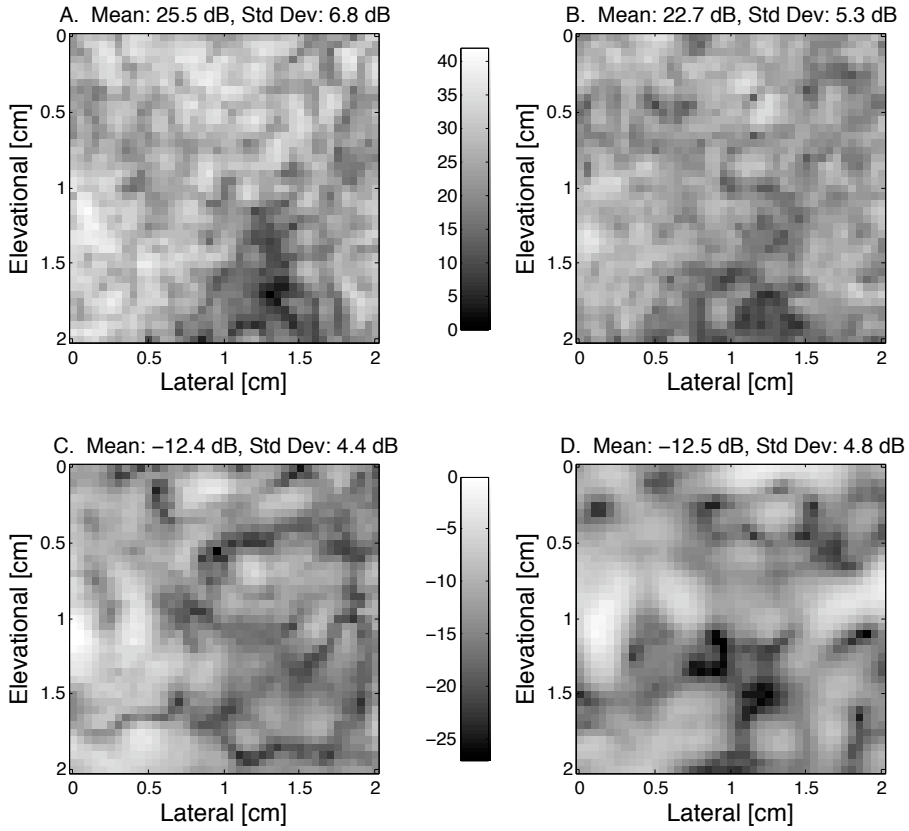

Figure 4.13: Backscattered and transmitted signals from and through a ∼2 mm thick bubble wall. The results are shown for two cases: (A, C) the focus of the annular array is positioned at the bubble wall , and (B, D) the focus is positioned approximately 1 cm past the bubble wall. In the comparisons of the backscattered signals (A, B), bright regions indicate high backscatter, and in the comparison of the transmitted signals (C, D), bright regions indicate high transmission. Signals in dB are calculated relative to the backscattered and transmitted signals from a gel with no bubble wall. The top sidebar indicating the dB scale corresponds to backscattered signals (A, B), and the bottom sidebar corresponds to transmitted signals (C, D).

4.4 Discussion

Both the size of the bubble clouds and threshold for ADV can change with the presence of a preexisting bubble wall. It appears that backscattering and the resulting field pattern generate pressures sufficient to cause ADV. Without the presence of a bubble wall in both size ranges of droplets, ADV occurs at approximately 7.6 MPa on average at this low, 750 kHz frequency, while the placement of a bubble wall in the focus produces ADV at applied pressures of approximately 3.9 MPa on average. The reduction in transmitted pressures is approximately half and seems to suggest that some constructive interference is occurring at least locally and even if the scatter from the wall is incoherent. Preexisting bubbles apparently enhance the proximal acoustic field, creating an environment that enhances the ADV effect or enables the achievement of a desired effect with approximately half the acoustic input originally required. In addition to constructive interference, harmonic backscatter from the bubbles may play a role, as the threshold for ADV decreases with increasing frequency [7]. Though pressures here could achieve an MI of ∼4 when using a bubble wall as compared to 1.9 as allowed by the Food and Drug Administration [15] for diagnostic purposes, we only propose these methods for therapeutic use for which the possibility of collateral damage may be acceptable to achieve the desired results.

The bubble wall can also serve as a protective layer, as simulated in these experiments where the bubble wall is prefocal. There is no apparent threshold for distal ADV as seen in Fig. 4.11 for the case of prefocal placement of the wall and ROIs placed at the focus. However, if the wall is not extensive enough to obstruct the lateral beam width, it is possible that ADV will occur at the focus (Fig. 4.10d). For higher pressures, increasing the wall thickness and/or bubble density can increase attenuation and backscatter. The effectiveness of the existing wall depend on the incident US since high pressures can still cause distal ADV if the attenuation and backscattering are not sufficient.

It would appear that when droplets are filtered to 5 μm (versus 16 μm), the bubble wall, when placed in the prefocal beam, is more effective in preventing ADV on the distal side and also in reflecting back energy to cause ADV on the proximal side. When examining cloud size, US pulses of 19 MPa produce clouds of 0.8 cm^2 cross sectional area in gels with 5 μm droplets (Fig. 4.11a, ROI proximal to wall) and 0.05 cm2 in gels with 16 μm droplets (Fig. 4.11c, ROI proximal to wall). The increased effectiveness of the bubble wall from 5 μm droplets may be due to a higher and more uniform bubble density.

Increasing the thickness and density of the wall can reduce the inhomogeneities found in thinner walls. A 2 mm thick bubble wall can vary by 4 and 6 dB in attenuation and backscatter (Fig. 4.13), respectively, thus affecting the ability to vaporize droplets on the proximal side and to prevent ADV on the distal side. The presence or absence of droplets in a particular location dictates the possibility of a vaporization event. The irregular distribution of droplets within the gel affects the creation of the bubble wall and also the creation of subsequent clouds. These issues need to be considered when using a bubble wall as a shield or as a reflector, since generating clouds with transmitted sub-threshold US requires sufficient backscatter. In order to successfully take advantage of the constructive interference patterns, droplets must be located in proximity of the focus because the resulting super-threshold volume is small.

While the structure of a bubble wall may be achievable in a tissue-mimicking gel, its ideal form will be more difficult to attain *in vivo*. For example, consider the situation of the vascular bed within perfused tissue. The spatial distribution of accumulated bubbles resulting from ADV will depend on many factors including the portion of the bed spanned by the acoustic field and the droplets vaporized within it. In capillaries, bubbles produced by ADV may become lodged as they are larger than the capillary diameter. If the bubbles are not large enough to immediately

lodge, they can lodge downstream, spreading the thickness of the wall, or lodge even further downstream into vasculature where their diffuse distribution does not substantially contribute to wall formation. Bubbles that are generated in the veins may also exit the insonified area and would not contribute to the wall at all. The lodging or containment of these bubbles in the structure of the wall may result in a higher bubble density in highly perfused tissues such as in the kidney and liver.

A second area of interest is tissue. Droplets can become extravascular if they pass through leaky capillaries, like those found in tumors or otherwise removed from the vascular system such as by the reticulo-endothelial system of the liver. In this case, a bubble wall can be created in a similar fashion as those in the experiments in this paper, but it is uncertain if the homogeneity in the distribution of droplets is adequate to produce a wall that is capable of acoustic field enhancement and shielding. The preliminary results presented in this paper in an *in vitro* environment are promising for *in vivo* application, though further investigation is needed.

4.5 Conclusions

The backscattering properties of microbubbles can augment or obstruct the sound field in the affected area. Constructive interference due to these effects reduces the transmitted pressures required for ADV, and the attenuation from these bubbles can create a protective boundary for distal areas. The potential result can be a defined area for therapy created by low pressures and amounts of energy. However, it is also important to take into account properties of the backscattering bubbles and how their spatial uniformity may affect subsequent US exposures.

REFERENCES

[1] B. C. Tran, J. Seo, T. L. Hall, J. B. Fowlkes, and C. A. Cain, "Microbubble-enhanced cavitation for noninvasive ultrasound surgery," *IEEE Trans Ultrason Ferroelect Freq Control*, vol. 50, no. 10, pp. 1296–1304, 2003.

[2] E. Stride and N. Saffari, "The potential for thermal damage posed by microbubble ultrasound contrast agents," *Ultrasonics*, vol. 1-942, pp. 907–913, 2004.

[3] J. R. Wu, "Temperature rise generated by ultrasound in the presence of contrast agent," *Ultrasound Med Biol*, vol. 24, no. 2, pp. 267–274, 1998.

[4] R. G. Holt and R. A. Roy, "Measurements of bubble-enhanced heating from focused, mhz-frequency ultrasound in a tissue-mimicking material," *Ultrasound Med Biol*, vol. 27, no. 10, pp. 1399–1412, 2001.

[5] O. D. Kripfgans, J. B. Fowlkes, D. L. Miller, O. P. Eldevik, and P. L. Carson, "Acoustic droplet vaporization for therapeutic and diagnostic applications," *Ultrasound Med Biol*, vol. 26, no. 7, pp. 1177–1189, 2000.

[6] O. D. Kripfgans, C. M. Orifici, P. L. Carson, K. A. Ives, O. P. Eldevik, and J. B. Fowlkes, "Acoustic droplet vaporization for temporal and spatial control of tissue occlusion: A kidney study," *IEEE Trans Ultrason Ferroelect Freq Control*, vol. 752, pp. 1101–1110, 2005.

[7] O. D. Kripfgans, J. B. Fowlkes, M. Woydt, O. P. Eldevik, and P. L. Carson, "*In vivo* droplet vaporization for occlusion therapy and phase aberration correction," *IEEE Trans Ultrason Ferroelect Freq Control*, vol. 49, no. 6, pp. 726–738, 2002.

[8] D. L. Miller, O. D. Kripfgans, J. B. Fowlkes, and P. L. Carson, "Cavitation nucleation agents for nonthermal ultrasound therapy," *J Acoust Soc Am*, vol. 107, no. 6, pp. 3480–3486, 2000.

[9] D. L. Miller and J. M. Song, "Lithotripter shock waves with cavitation nucleation agents produce tumor growth reduction and gene transfer in vivo," *Ultrasound Med Biol*, vol. 28, no. 10, pp. 1343–1348, 2002.

[10] R. F. Mattrey, "The potential role of perfluorochemicals (pfcs) in diagnostic imaging," *Artificial Cells Blood Substitutes and Immobilization Biotechnology*, vol. 222, pp. 295–313, 1994.

[11] J. Staudenraus and W. Eisenmenger, "Fiberoptic probe hydrophone for ultrasonic and shock-wave measurements in water," *Ultrasonics*, vol. 31, no. 4, pp. 267–273, 1993.

[12] M. R. Bailey, L. N. Couret, O. A. Sapozhnikov, V. A. Khokhlova, G. Ter Haar, S. Vaezy, X. G. Shi, R. Martin, and L. A. Crum, "Use of overpressure to assess the role of bubbles in focused ultrasound lesion shape in vitro," *Ultrasound Med Biol*, vol. 27, no. 5, pp. 695–708, 2001.

[13] W. S. Chen, A. A. Brayman, T. Matula, and L. A. Crum, "Inertial cavitation dose and hemolysis produced in vitro with or without optison®," *Ultrasound Med Biol*, vol. 529, pp. 725–737, 2003.

[14] N. A. Watkin, G. R. terHaar, and I. Rivens, "The intensity dependence of the site of maximal energy deposition in focused ultrasound surgery," *Ultrasound Med Biol*, vol. 22, no. 4, pp. 483–491, 1996.

[15] FDA (US Food and Drug Administration), "Information for manufacturers seeking marketing clearance of diagnostic ultrasound systems and transducers," 1997.

CHAPTER V

Conclusions and Future Work

5.1 Summary of Thesis Contribution

5.1.1 Introduction

The collected work presented in Chapters II-IV contribute to the transition of embolotherapy by acoustic droplet vaporization (ADV) to the intended *in vivo* conditions. Much of the fundamental science underpinning the manufacturing and behavior of droplets in response to an acoustic field was explored in a series of published journal articles [1][2][3]. The information gleaned from these findings forged the way to successful application of concept and execution in a small animal model [4].

However, in translating these findings to a larger animal model that is on the scale of human beings, additional issues needed to be addressed. The attenuation from overlying layers is a constant issue in any type of ultrasound, and likewise, it must be contended with here. Knowing that ADV is achievable *in vivo* but without any overlying tissues, two avenues can be approached: (1) ensure that the therapeutic transducer has enough acoustic power to achieve the necessary *in situ* pressures, and (2) to devise a strategy to reduce the necessary pressures for ADV. A single transducer may not have the capacity to effectively treat the high variability of patient types; therefore, tackling the latter solution is the simpler, less expensive, and perhaps more elegant approach.

Therefore, this dissertation explored strategies to reduce the requisite pressures for ADV. First, the role of inertial cavitation (IC) in ADV was investigated and then in turn, IC was induced, via the disruption at low amplitudes of ultrasound contrast agent (CA) to try to trigger ADV. This strategy involving CAs was then tested under *in vitro* transcutaneous conditions, where both threshold pressures were measured and droplet conversion efficiency was evaluated. A different strategy in which prudent targeting of droplets already situated in either the capillary bed or in tissues created spatially localized microbubbles. These microbubbles were found to serve as a "bubble wall," which could prevent further distal ADV and at the same time, could reduce the acoustic output necessary for proximal ADV.

5.1.2 Experimental Conclusions

Acoustic Droplet Vaporization: Effects of Pulse Duration and Contrast Agent

The role of IC in ADV was explored by a series of experiments that examined the effects of pulse duration from microsecond to millisecond pulses as well as the effects of ultrasound contrast agent (CA). ADV, contrast disruption, and broadband noise emissions, which are the acoustic signature of IC, were detected and compared for correlation to each other.

It was found that at 1.44 MHz, an almost bimodal relationship existed when pulse durations for single pulses ranged from 20 μs to 20 ms. ADV thresholds (as detected by B-mode US) were relatively constant until they dropped for pulse durations lasting longer than 1 ms. Repetitive 20 μs pulses had the same ADV threshold as single long 20 ms pulses when total on-time remained constant. The thresholds for broadband noise followed similar trends as the thresholds for ADV, as well as similar values of pressure. There has been no indication that any further change in broadband noise threshold exists for pulse durations lasting longer than 20 ms [5][6], the longest duration tested in these experiments. Therefore, it was

concluded that IC played a role in ADV, although it remains undetermined in what capacity.

The addition of CAs verified that IC external to a droplet can be a mechanism of ADV. CA concentrations from 10^3, 10^4, and 10^5 microspheres/mL all reduced the threshold by an order of magnitude when 20 ms pulse durations were used. Although the probability of ADV was the largest with the highest concentration of CA, the actual differences in threshold were modest. The decrease in ADV threshold with CA was less substantial with 20 μs pulses, which reduced the threshold by a factor of three (9.5 dB). Nonetheless, this reduction in threshold is appreciable when considering the amount of attenuation that is expected when treating a target transcutaneously, which is 10.75 dB on average for the human abdominal wall [7].

Attenuation and Efficiency Considerations in Acoustic Droplet Vaporization for Embolotherapy

The relationships found between ADV threshold and contrast agent were reconfirmed in the next set of experiments. A different transducer with a 1 MHz operating frequency, higher focal gain and greater power was used for its capability to be able to reach a target at depth for ADV.

It was found that approximately the same amount of power was necessary to achieve ADV through a water path as it was through an attenuating tissue-mimicking (TM) phantom when CA were added. Repetitive pulsing with 10 μs pulse durations were used for these experiments. When comparing pressures necessary to achieve the desired effect, the rarefactional pressure appeared to be the salient determinant of ADV. Although high frequencies are able to vaporize droplets more easily when propagating through a water path [1], the higher harmonics did not appear to be significant contributors in the presented results.

Pulse repetition frequency (PRF) was found to play a pivotal role in the efficiency of droplet conversion when only droplets were present and also when they were

combined with CA. In either case, an optimal PRF was apparent. When droplets were combined with CA, a low PRF was necessary such that a new supply of CA would be replenished within the acoustic beam. When amplitudes increased above the measured threshold, the effective volume above threshold also increased as the portion of the acoustic beam that was at amplitudes above threshold expanded. Since the threshold for inertial collapse of CA was much lower than the ADV threshold, the effective disruption zone for CA was larger than the effective vaporization zone for droplets when amplitudes were at or above ADV threshold.

Absent of any CA, an optimal PRF was also found. When PRFs were too high, bubbles that were visualized through B-mode US in the focus of the vaporizing transducer were absent downstream. Orthogonal imaging planes confirmed that the disappearance of bubbles was not due to radiation force. Previous experiments showed that at a higher frequency, an optimal PRF was not apparent [8], but instead, there existed an exponential rise with PRF with eventual saturation.

A hypothesis was proposed to explain these findings. Several papers in the literature [9][10][11][12] theoretically developed and experimentally tested the pressure threshold for inertial collapse of bubbles for a given insonating frequency, bubble size, ambient pressure, ambient temperature, and attained temperature at collapse. These works assessed the likelihood of cavitation for diagnostic US. When applying this theory to the bubble sizes expected from the droplet size distribution to be used *in vivo*, it was found that most of the bubbles would have been destroyed when pressures exceeded the ADV threshold. Thus, there are competing phenomena when PRF is too high; the bubbles created by ADV can be subsequently destroyed with the next US pulse. For a 1 MHz center frequency, the threshold for inertial collapse for a 60 μm bubble at 3 MPa P_r is lower than the ADV threshold at 3.8 MPa P_r.

Spatial Control of Gas Bubbles and their Effects on Acoustic Fields

Droplets can be vaporized in the vasculature, or for some droplets of smaller size, they can pass through leaky vessel walls and traverse into the tissue. Discussion thus far has concentrated on the vaporization of droplets in feeder arteries, but it does not preclude the possibilities of targeting other areas. In fact, targeting in areas such as capillary beds or in droplet-embedded tissue can be advantageous as it enables the ability to guide bubble placement. In capillaries where the diameter is small and in restricted environments such as the tissue, an ADV event could create a bubble that would more or less lodge in its present location. Manipulation of bubble placement could then be used for further therapeutic purposes.

The behavior of ADV in a constrained environment was explored in a polyacrylamide gel. It was found that the bubble clouds generated in the gel matrix resembled the types of lesions documented previously in other experiments [13][14][15]. Few pulses ($\sim$ 20 cycles) created bubble clouds resembling a cigar shape, while additional pulses would cause the bubble cloud to resemble a tear drop. It was observed that after the formation of a cigar shaped bubble cloud, further ADV would occur proximally and cause the bubble cloud to grow toward the transducer. It appeared that shadowing occured after the creation of the first bubbles, and subsequent acoustic pulses were backscattered.

Thus, the same effect was artificially devised. A bubble wall, which was created in the lateral plane of and prior to insonation by the vaporizing transducer, created an environment of shadowing distal to the wall and of backscatter proximal to the wall. It was found that the bubble wall, with diminished distal fields, could serve as a protective barrier against further distal ADV. The backscattered energy enhanced the proximal acoustic field, enabling proximal ADV to occur at approximately half the applied pressures necessary when no bubble wall was present. When focusing distal to the bubble wall, it was found that some "leakage" could occur through the wall

when insonating at higher amplitudes. However, increasing the thickness of the wall prevented these effects. Thickness, expansiveness, and homogeneity of the bubble wall affected its efficacy as an acoustic shield and enhancer. However, despite the variability found within a thicker (∼2 mm vs. ∼1 mm) bubble wall in backscattered and transmitted signal, it appeared that ample constructive interference occurred to consistently enhance the acoustic field for subsequent vaporization with lower energy input.

Summary of Results

Transcutaneous *in vivo* ADV can be effective. When optimizing the process, careful consideration must be taken when designing pulse parameters and treatment strategy. The results from this dissertation are summarized below:

- ADV threshold decreases with acoustic exposure.
- ADV threshold decreases with the addition of CA. With long pulses, the introduction of CA can decrease the threshold by an order of magnitude, whereas with short microsecond pulses, CA can decrease the threshold by a factor of 2-3.
- ADV threshold is dependent on *in situ* peak rarefactional pressure.
- The relationship between PRF and maximum efficiency for droplet conversion when only droplets are present appears to be frequency dependent. At low frequencies, an optimal PRF exists. At high frequencies and below the threshold for inertial collapse, efficiency increases with PRF until bubble production saturates.
- There is an optimal PRF for maximum efficiency when droplets are combined with CA.

- Lodged bubbles produced by ADV can behave as a shield and reflector for further US therapy. Choice of a target artery or volume is important in order to prevent obstruction of further US treatment. Location of an ADV bubble wall can also create an advantageous acoustic field such that less pressure is required for further proximal US treatment.

5.2 Future Work

5.2.1 Further investigation of the Mechanisms of ADV

The mechanisms for ADV are not fully understood. We have found that inertial cavitation (IC) can occur within and outside of the droplet [5], each of which triggers a vaporization event. As summarized in the previous section, it was shown in Chapters II and III that IC external to a droplet could trigger ADV via the inertial collapse of CA microbubbles. In the absence of CA, evidence from high speed photography (Fig. 5.1) shows that for large droplets on the order of 344 μm in diameter, nucleation sites do occur within the droplet, ultimately forming a gas bubble. However, for these large droplets, these nucleation sites do not trigger the vaporization of the entire droplet. Instead, the droplets become biphasic; it contains both a liquid and gas within it. For smaller droplets (18-45 μm in diameter), dipole motion and gas inception was seen also through high speed photography [3]. However, it was not proven that these nucleation sites emerged from within the droplet, as the bubbles may have been superimposed and may have laid outside of the lateral plane (with respect to the camera) of the droplet. In the case for the larger droplet, the bubbles coalesced within the droplet itself, implying that nucleation occurred within the droplet.

The difference between the two mechanisms may lie in the relationship between droplet size and wavelength. As frequency increases, the acoustic wave has more interaction with the droplet, as exhibited by the dipole oscillation that occurs in

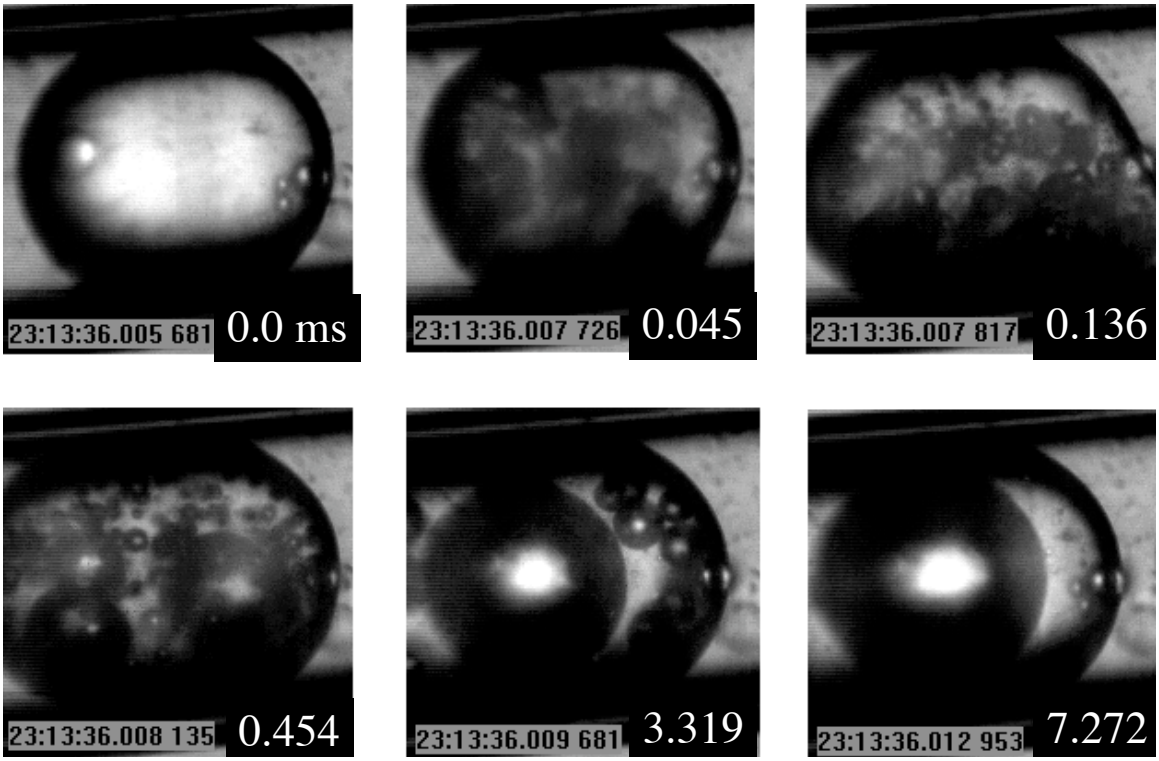

Figure 5.1: ADV of a 344 μm droplet. The duration of insonation is approximately 10 ms and begins with the first frame at 0.0 ms. Images are taken with a high speed camera. Data was presented at [16].

sync with the acoustic pulse [3]. We do not yet have any evidence as to what occurs during ADV at low insonating frequencies when CA are not present.

However, it was shown in Chapter II that aggregates can form at low frequencies for long pulse durations or "on-time." In this case, aggregates may have behaved like a large droplet, and perhaps the collective size allowed for more interaction with the ultrasound. If the albumin proteins were not fully cross-linked on the shell of a single droplet, they could even have cross-linked with proteins from neighboring droplets within the aggregate. The ultrasound wave could interact with the droplets as an aggregate as well as individually, with each droplet imposing mechanical forces on the other. These aggregates could perhaps be compared to work by Matsumoto et al. [17], who have shown that individual bubbles interact with each other in a bubble cloud to generate a collapse with higher energy than individual bubbles collapses.

These clouds have a lower resonant frequency than the bubbles that comprise it. Likewise, for a given low frequency and pressure amplitude, there could in fact exist a "critical" size for aggregation that allows for interaction with the ultrasound wave and subsequent vaporization. The relative size of these aggregates to the insonating wavelength could be compared to the relative size of a single droplet with a wavelength at a higher insonating frequency, such as the droplet imaged in Kripfgans et al. [3], which vaporized in the absence of surrounding droplets. Using Stokes law and given the rate that the aggregates are falling, the size of the aggregates can be calculated. For repetitive pulsing at below ADV threshold amplitudes (Chapter II), calculated aggregate sizes ranged from 118-150 μm in diameter. Further investigation must be conducted to evaluate what aggregate sizes are necessary for vaporization and at what pressures.

Whether this aggregation occurs in a flow environment remains unknown for these acoustic parameters, and thus it is undetermined whether aggregates are a necessary component of ADV. An experiment much like those performed in this dissertation, with the exception of a horizontally oriented flow tube rather than a vertically oriented tube, may allow for differentiation between aggregated droplets that would sink to the bottom of the tube from buoyant bubbles that would rise to the top of the tube. Gradually increasing the flow speed from a standstill while maintaining an amplitude known to produce aggregates may also reveal whether aggregates can form in flow and at what flow rates they're visible through B-mode ultrasound. Using microscopy, it has been shown that CA microbubbles form transient aggregates in flow due to the presence of pulsed ultrasound [18]. It remains to be determined whether this would occur with droplets under flow condition tested here or *in vivo*.

Investigation of the behavior of perfluorocarbons (PFCs) of higher boiling points (BP) may further elucidate the mechanisms at play in this vaporization

process. PFCs of higher boiling point would make more stable droplets as the level of superheat is not as high if not nonexistent. If IC external to the droplet is responsible for triggering a vaporization event, then ADV threshold could be the same for either dodecafluoropentane (DDFP) droplets (BP = 29°C) or droplets of another PFC, such as 1,1,2-trichlorotrifluoroethane (BP = 47-48°C) or perfluorohexane (BP = 58-60°C) if vaporization occurs at all. If vaporization does occur, it should be temporary, and the PFC should return to liquid phase. As PFCs with higher BP than the ambient temperature (either room or body temperature), they may not undergo phase transition at all. In this case, passive acoustic detection of broadband noise would determine if IC occurred. The amplitudes at which IC occurs for these high boiling point PFC droplets can be compared to those found in Chapter II if the same transducer is used and if the droplets are of the same size distribution and concentration. A secondary study may be required to understand the droplet yield from manufacturing different PFC droplets as it has been shown that ADV threshold decreases for larger droplets [3] and IC threshold decreases with increasing concentrations of nuclei [19].

5.2.2 Effects of the Inertial Collapse of CAs on ADV

On the same note, it would be beneficial to understand the direct interaction between CA and droplet. The inertial collapse of CA can trigger a vaporization event, but it is undetermined how they interact. From these initial exploratory experiments, it was found that a small amount of CA in comparison to the amount of droplets that were present was required to achieve the desired effect. It would be beneficial to understand the ratio required for optimal droplet conversion.

A simple solution can be employed to understand the mechanism between droplet and CA. Because the CA concentrations tested in this thesis were above the apparent minimum quantity of CA necessary to facilitate the ADV process, the ratio of the

two agents can be further adjusted to ascertain the threshold concentration. Given a certain droplet concentration, what is the minimum number of CA microbubbles required to trigger a detectable ADV event? In other words, how many droplets can the collapse of one CA microbubble affect?

Since the concentrations of each agent are known, the average distance between each droplet and CA can also be calculated assuming a homogenous distribution. For the concentrations used in Chapter III, the average distance between a CA microbubble and its surrounding droplets was approximately 86 μm. In this manner, minimum proximity of the agents can be measured. The required proximity can be estimated by lowering the concentration of both droplets and CA but at the same time maintaining the ratio of the two agents. The ADV threshold measurements with CA in this dissertation provide a baseline ratio of concentrations. Reducing the concentrations increases the average distance between agents, and the threshold quantity to trigger ADV would indicate the minimum distance necessary between CA and droplet.

This measurement of minimum distance between CA microbubble and droplet can perhaps provide insight into the mechanisms involved. Several events accompany an inertial collapse including high temperatures at the core, jet streams, and secondary shock waves. Jet streams are formed from asymmetrical collapses when bubbles are near a solid surface and cause considerable local damage to the surface [20]. Although droplets cannot be considered a solid surface, they may behave similarly to a bubble, which imposes secondary Bjerknes forces on a neighboring bubble. Thus, this interaction between CA and droplet may promote an asymmetrical collapse and the formation of jet streams, and requires that the two agents be in close proximity. This jet stream may then, due to its proximity, be able to disrupt the albumin shell of the droplet, exposing the previously encapsulated superheated liquid to the medium for subsequent vaporization. However, if secondary shock waves are responsible for

or act as an additional perturbational source for triggering an ADV event, the two agents may not need to be as close. The statistics involved in chance collisions or even movement to the appropriate proximity must also be taken into consideration. It is possible that one chance vaporization event could launch a cascade of events.

High speed shadowgraphy is an ideal option to capture such situations when, for example, (1) microbubble and droplet are situated close together, (2) microbubble and droplet are situated farther apart, and (3) when two droplets surround one microbubble. High speed shadowgraphy would provide direct visual evidence of the interaction between the inertial collapse of a CA microbubble and a surrounding droplet, where both jet streams and shock waves can be perceived (Fig. 5.2). Aside from visualizing the consequences of an inertial collapse, if a jet stream disrupted the CA shell, the resulting events leading to the vaporization of a droplet would look much different than a droplet's response to a sound wave, where nuclei can form within the droplet (Fig. 5.1) or dipole oscillation may occur [3]. Likewise, similar behavior could occur if a secondary shock wave were emitted from the inertial collapse of a microbubble. Shadowgraphy would also reveal if a combination of the two is necessary. Positioning of the CA and droplet in the field of view may be difficult; however, laser induced optical breakdown (LIOB) has been previously used to create bubbles in precise locations [21] and can be used as a tool in this case to create bubbles in desired locations with respect to preexisting droplets.

An additional experiment can be performed to test the hypothesis that the inertial collapse of CAs causes ADV by means of disrupting the albumin shell. Under current conditions where ADV occurs in saline, it is possible that the shell is disrupted and that the consequent vaporization occurs before the shell can repair and cross-link again. If this is the case, then an experiment can be designed to allow optimal conditions for shell repair; a medium saturated with albumin may provide the necessary building blocks for the albumin shell to repair before vaporization. If

saturating the medium with albumin significantly alters the ADV threshold, it would appear that shell disruption is the mechanism for ADV with CAs. However, a minor shift in threshold may only be a result of a change in the medium's viscosity due to high albumin concentration. In order to compensate for this potential difference, acoustic emissions can be monitored and used as a feedback mechanism to adjust the level of cavitation activity such that it is the same in both saline and in a high albumin medium. Once the level of cavitation activity, or amount of "trigger," is matched, any differences in ADV threshold can be attributed to the change in shell properties. Alternatively, modifying the shell composition of the droplet and measuring changes in the ADV threshold would also demonstrate the role of shell disruption in ADV.

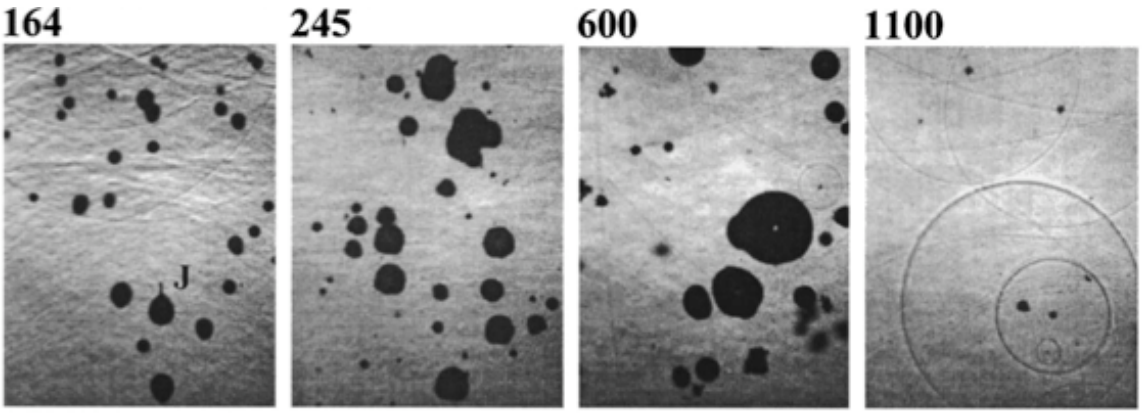

Figure 5.2: Zhong et al. produced high speed shadowgraphs of the inception and collapse of bubbles produced by a shock wave generated by a shock wave lithotripter [22]. The numbers at the top of the images indicate frames captured at 164, 245, 600, and 1100 μs after spark discharge. A microjet is seen at 164 μs and is marked by "J." Bubble growth and/or coalescence are seen at 245 and 600 μs, and secondary shock waves are seen at 1100 μs.

5.2.3 Optimization

The work presented in this dissertation investigates the effects of acoustic parameters that will aid in being able to cause ADV *in vivo* transcutaneously.

However, further experimental work can be done to refine the value for optimal PRF for any given beam width and flow rate. It may be more advantageous to insonate at a higher frequency if it allows more frequent pulsing, in which case a large beam width would also be favorable. However, at these higher frequencies, increasing the pressure amplitude could also enter the regime where ADV bubbles could collapse. An in-depth investigation of efficiency as it relates to carrier frequency, amplitude, beam width, and its optimal PRF would be extremely beneficial to *in vivo* applications where rapid occlusion and maximum droplet conversion are desirable.

5.2.4 Targeted Droplets

Targeted Droplets for Drug Delivery

Targeted agents including CAs have been the subject of recent scientific research for effective cancer therapy [23][24][25]. Likewise, the ability for great specificity would improve the efficacy of ADV in therapy. Development of droplets for targeted drug delivery is ongoing and aims to manufacture targeted drug-bearing droplets that would release the drug only during ADV to a specific site. Concurrent vascular occlusion could further localize the drug therapy. Incorporation of Paclitaxel into a droplet and its subsequent vaporization has already been successful [26][27].

Biphasic agent

As droplets can be targeted with appropriate ligands for drug delivery, CA can also be paired with the droplets in a similar manner. Since it has been shown that the insonation of CA microbubbles can trigger ADV, it may be possible to combine the two agents such that each droplet is bound to a microbubble. The incorporation of a microbubble into the droplet may be another alternative [28], but the microbubbles' response to the acoustic field is stabilized, as the superheated liquid DDFP is, by the albumin shell. Experiments proposed in Section 5.2.2 would contribute to the

design of these droplets.

Some of the complications when droplets were combined with CA included the need for PRF to be reduced in order for the supply of CA to be replenished as they were destroyed in larger volumes than droplets were vaporized. If a microbubble were attached to these droplets, then a vaporization event could occur with every collapse of a microbubble. Seemingly, the effective zone for ADV would expand to the effective zone for inertial collapse of CAs.

If successful ADV is attained with these coupled agents, a new and perhaps more convenient method of ADV is available. Many US systems are currently equipped to employ a technique to monitor local blood flow information by measuring real-time refill curves [29]. In this technique, CAs flow through the vasculature and are allowed to populate the volume of interest. Subsequently, a series of high mechanical index (MI) pulses, employing the maximum acoustic power allowed by the diagnostic machine, are fired transcutaneously and destroy all CAs in the imaging plane. The refill of CA is then monitored. Because CA can be destroyed by an imager when imaging an organ at depth, ADV could be also achieved with high MI pulses. Exact alignment between therapy and imaging feedback, since they are the same transducer, allows for simple targeting. The use of an imaging transducer can additionally allow intercostal penetration to the kidney and electronic scanning for complete occlusion of the target.

5.2.5 *In vivo* Demonstration

Thus far, *in vivo* demonstrations of ADV have been confined to a small animal model without any acoustic attenuation from overlying tissue [4] . With the findings from the *in vitro* work presented in this dissertation relating to attenuation effects and strategies to reduce thresholds, current *in vivo* work applies these techniques to a large animal model, where treatment is transcutaneous. CA are combined with

droplets for injection, and PRF has been noted *in vivo* to have a deleterious effect if it was too high. Like the previous study by Kripfgans et al. [4], droplet injections are being performed intraarterially, but future work will transition to intravenous injections, which will require much higher doses [2].

Phase Aberration Correction

Abdominal access for treatment of the kidney was considered here as the preferred acoustic window. The abdominal wall was shown to cause appreciable attenuation, but furthermore, appreciable aberration was also measured [7]. Microstructures within the abdominal wall due to both muscle and fat tissue cause wavefront and focus distortion. The ability to focus accurately will change from patient to patient as both muscle and fat layers vary.

Thus, it will become important in transcutaneous treatment to be able to refocus the beam for both accurate targeting and to achieve sufficient pressures. Current research uses the bubbles created by ADV as point beacons to perform time reversal [30] in order to penetrate through the skull and focus in the brain. In time reversal, pulses are fired from individual elements on an US transducer. As each wave propagates through a different path, it is aberrated and attenuated. Consequently, the waves arrive asynchronously at the focus. Given a point beacon, the asynchronous echoes can be recorded and time reversed. With the next pulse, time delays are applied to each element such that the echo received last is transmitted first, and the echo received first is transmitted last. Thus, temporal and spatial pulse compression is achieved.

For ADV through the abdominal wall, echoes from the first bubbles created by ADV could be time reversed and employed for subsequent insonation. For patients with a highly aberrating abdominal wall, time reversal would significantly reduce the amount of power output required by the system as well as provide a dependable focal size and location. This consistency would increase repeatability and reliability

of ADV treatments between patients, both of which are important for clinical application.

5.3 Acknowledgments

This work is supported in part by US PHS Grant 5RO1 EB00281-09.

REFERENCES

[1] O. D. Kripfgans, J. B. Fowlkes, D. L. Miller, O. P. Eldevik, and P. L. Carson, "Acoustic droplet vaporization for therapeutic and diagnostic applications," *Ultrasound Med Biol*, vol. 26, no. 7, pp. 1177–1189, 2000.

[2] O. D. Kripfgans, J. B. Fowlkes, M. Woydt, O. P. Eldevik, and P. L. Carson, "*In vivo* droplet vaporization for occlusion therapy and phase aberration correction," *IEEE Trans Ultrason Ferroelect Freq Control*, vol. 49, no. 6, pp. 726–738, 2002.

[3] O. D. Kripfgans, M. L. Fabiilli, P. L. Carson, and J. Fowlkes, "On the acoustic vaporization of micrometer-sized droplets," *J Acoust Soc Am*, vol. 116, no. 1, pp. 272–281, 2004.

[4] O. D. Kripfgans, C. M. Orifici, P. L. Carson, K. A. Ives, O. P. Eldevik, and J. B. Fowlkes, "Acoustic droplet vaporization for temporal and spatial control of tissue occlusion: A kidney study," *IEEE Trans Ultrason Ferroelect Freq Control*, vol. 752, pp. 1101–1110, 2005.

[5] A. H. Lo, O. D. Kripfgans, P. L. Carson, E. D. Rothman, and J. B. Fowlkes, "Acoustic droplet vaporization threshold: Effects of pulse duration and contrast agent," *IEEE Trans Ultrason Ferroelect Freq Control*, vol. 54, no. 5, pp. 933–946, 2007.

[6] T. Giesecke and K. Hynynen, "Ultrasound-mediated cavitation thresholds of liquid perfluorocarbon droplets *in vitro*," *Ultrasound Med Biol*, vol. 29, no. 9, pp. 1359–1365, 2003.

[7] L. M. Hinkelman, T. D. Mast, L. A. Metlay, and R. C. Waag, "The effect of abdominal wall morphology on ultrasonic pulse distortion. part i. measurements," *J Acoust Soc Am*, vol. 104, no. 6, pp. 3635–3649, 1998.

[8] O. D. Kripfgans, *Acoustic droplet vaporization for diagnostic and therapeutic applications*. PhD thesis, University of Michigan, 2002.

[9] R. E. Apfel, "Acoustic cavitation prediction," *J Acoust Soc Am*, vol. 69, no. 6, pp. 1624–1633, 1981.

[10] R. E. Apfel, "Possibility of microcavitation from diagnostic ultrasound," *IEEE Transactions on Ultrasonics Ferroelectrics and Frequency Control*, vol. 33, no. 2, pp. 139–142, 1986.

[11] C. K. Holland and R. E. Apfel, "An improved theory for the prediction of microcavitation thresholds," *IEEE Transactions on Ultrasonics Ferroelectrics and Frequency Control*, vol. 36, no. 2, pp. 204–208, 1989.

[12] R. E. Apfel and C. K. Holland, "Gauging the likelihood of cavitation from short-pulse, low-duty cycle diagnostic ultrasound," *Ultrasound in Medicine and Biology*, vol. 17, no. 2, pp. 179–185, 1991.

[13] M. R. Bailey, L. N. Couret, O. A. Sapozhnikov, V. A. Khokhlova, G. Ter Haar, S. Vaezy, X. G. Shi, R. Martin, and L. A. Crum, "Use of overpressure to assess the role of bubbles in focused ultrasound lesion shape in vitro," *Ultrasound Med Biol*, vol. 27, no. 5, pp. 695–708, 2001.

[14] W. S. Chen, C. Lafon, T. J. Matula, S. Vaezy, and L. A. Crum, "Mechanisms of lesion formation in high intensity focused ultrasound therapy," *Acoust Res Lett Online*, vol. 4, pp. 41–46, 2003.

[15] N. A. Watkin, G. R. terHaar, and I. Rivens, "The intensity dependence of the site of maximal energy deposition in focused ultrasound surgery," *Ultrasound Med Biol*, vol. 22, no. 4, pp. 483–491, 1996.

[16] O. D. Kripfgans, S. Samuel, and J. B. Fowlkes, "Vaporization for perfluorocarbon droplets," (San Diego, California), Ultrasound Contrast Symposium, March 2005.

[17] Y. Matsumoto, S. Yoshizawa, and T. Ikeda, "Dynamics of bubble cloud in focused ultrasound," in *Proc. of 2nd International Symposium on Therapeutic Ultrasound*, pp. 290–299, 2003.

[18] P. A. Dayton, K. E. Morgan, A. L. S. Klibanov, G. Brandenburger, K. R. Nightingale, and K. W. Ferrara, "A preliminary evaluation of the effects of primary and secondary radiation forces on acoustic contrast agents," *IEEE Trans Ultrason Ferroelect Freq Control*, vol. 644, pp. 1264–1277, 1997.

[19] C. X. Deng, Q. Xu, and R. E. Apfel, "Inertial cavitation produced by pulsed ultrasound in controlled host media," *J Acoust Soc Am*, vol. 100, no. 2, pp. 1199–1208, 1996.

[20] C. C. Church, "A theoretical study of cavitation generated by an extracorporeal shock wave lithotripter," *J Acoust Soc Amer*, vol. 86, pp. 215–227, 1989.

[21] S. M. Milas, J. Y. Ye, T. B. Norris, K. W. Hollman, S. Y. Emelianov, and M. O'Donnell, "Acoustic characterization of microbubble dynamics in laser-induced optical breakdown," *IEEE Trans Ultrason Ferroelect Freq Control*, vol. 50, no. 5, pp. 517–522, 2003.

[22] P. Zhong, H. Lin, X. Xi, S. Zhu, and E. Bhogte, "Shock wave inertial microbubble interaction: Methodology, physical characterization, and bioeffect study," *J Acoust Soc Am*, vol. 105, no. 3, pp. 1997–2009, 1999.

[23] S. H. Bloch, R. E. Short, K. W. Ferrara, and E. R. Wisner, "The effect of size on the acoustic reponse of polymer-shelled contrast agents," *Ultrasound Med Biol*, vol. 31, no. 3, pp. 439–444, 2005.

[24] M. A. Borden, M. R. Sarantos, S. M. Stieger, S. I. Simon, K. W. Ferrara, and D. A. Dayton, "Ultrasound radiation force modulates ligand availability on targeted contrast agents," *Molecular Imaging*, vol. 5, no. 3, pp. 139–147, 2006.

[25] P. A. Dayton, S. Zhao, S. H. Bloch, P. Schumann, K. Penrose, T. Matsunaga, R. Zutshi, A. Doinikov, and K. W. Ferrara, "Application of ultrasound to selectively localize nanodroplets for targeted imaging and therapy," *Molecular Imaging*, vol. 5, no. 3, pp. 160–174, 2006.

[26] O. D. Kripfgans, A. H. Lo, and F. d'Errico, "Localized chemo-therapy using acoustic droplet vaporization," (Seoul, South Korea), International Symposium on Therapeutic Ultrasound, June 2007.

[27] N. Rapoport, "Multifunctional nanoparticles for combining ultrasonography with ultrasound-mediated chemotherapy," (Seoul, South Korea), International Symposium on Therapeutic Ultrasound, June 2007.

[28] D. A. B. Smith, T. M. Porter, J. Martinez, S. Huang, R. C. MacDonald, D. D. McPherson, and C. K. Holland, "Destruction thresholds of echogenic liposomes with clinical diagnostic ultrasound," *Ultrasound Med Biol*, vol. 33, no. 5, pp. 797–809, 2007.

[29] T. C. U. Potdevin, J. B. Fowlkes, A. P. Moskalik, and P. L. Carson, "Refill model of rabbit kidney vasculature," *Ultrasound Med. Biol.*, vol. 32, no. 9, p. 13311338, 2006.

[30] K. J. Haworth, J. B. Fowlkes, P. L. Carson, and O. D. Kripfgans, "Towards aberration correction of transcranial ultrasound using acoustic droplet vaporization." In press.